Development of conducting polymer devices for the monitoring of in vitro barrier tissue models

Magali Ferro

N°d'ordre NNT : 2018LYSEM017

THESE de DOCTORAT DE L'UNIVERSITE DE LYON
opérée au sein de
l'Ecole des Mines de Saint-Etienne

Ecole Doctorale N° 488
Sciences, Ingénierie, Santé

Spécialité de doctorat : Microélectronique
Discipline : Bioélectronique

Soutenue publiquement le 03/10/2018, par :
(Magali Patricia Marie Ferro)

Development of conducting polymer devices for the monitoring of 3D barrier tissue models

---

Devant le jury composé de :

Mamessier, Emilie CR1 Aix-Marseille Univeristy	Présidente
Mamessier, Emilie, Chargée de recherche Université Aix-Marseille	Rapporteure
André, Frederic, Maitre de conférences Université Aix-Marseille	Rapporteur
Heilshorn, Sarah, Assistant Professeur Stanford Univeristy	Examinatrice
Van der Meer, Andries, Assistant Professeur Twente University	Examinateur
Owens, Roisin Assistant Professeur Cambridge University	Directrice de thèse
O'Connor, Rodney grade/qualité EMSE	Co-directeur de thèse
Ramuz, Marc Assistant Professeur EMSE	Invité

Spécialités doctorales	Responsables :	Spécialités doctorales	Responsables
SCIENCES ET GENIE DES MATERIAUX	K. Wolski Directeur de recherche	MATHEMATIQUES APPLIQUEES	O. Roustant, Maître-assistant
MECANIQUE ET INGENIERIE	S. Drapier, professeur	INFORMATIQUE	O. Boissier, Professeur
GENIE DES PROCEDES	F. Gruy, Maître de recherche	SCIENCES DES IMAGES ET DES FORMES	JC. Pinoli, Professeur
SCIENCES DE LA TERRE	B. Guy, Directeur de recherche	GENIE INDUSTRIEL	N. Absi, Maitre de recherche
SCIENCES ET GENIE DE L'ENVIRONNEMENT	D. Graillot, Directeur de recherche	MICROELECTRONIQUE	Ph. Lalevée, Professeur

EMSE : Enseignants-chercheurs et chercheurs autorisés à diriger des thèses de doctorat (titulaires d'un doctorat d'Etat ou d'une HDR)

ABSI	Nabil	MR	Génie industriel	CMP
AUGUSTO	Vincent	CR	Image, Vision, Signal	CIS
AVRIL	Stéphane	PR2	Mécanique et ingénierie	CIS
BADEL	Pierre	MA(MDC)	Mécanique et ingénierie	CIS
BALBO	Flavien	PR2	Informatique	FAYOL
BASSEREAU	Jean-François	PR	Sciences et génie des matériaux	SMS
BATTON-HUBERT	Mireille	PR2	Sciences et génie de l'environnement	FAYOL
BEIGBEDER	Michel	MA(MDC)	Informatique	FAYOL
BLAYAC	Sylvain	MA(MDC)	Microélectronique	CMP
BOISSIER	Olivier	PR1	Informatique	FAYOL
BONNEFOY	Olivier	MA(MDC)	Génie des Procédés	SPIN
BORBELY	Andras	MR(DR2)	Sciences et génie des matériaux	SMS
BOUCHER	Xavier	PR2	Génie Industriel	FAYOL
BRODHAG	Christian	DR	Sciences et génie de l'environnement	FAYOL
BRUCHON	Julien	MA(MDC)	Mécanique et ingénierie	SMS
CAMEIRAO	Ana	MA(MDC)	Génie des Procédés	SPIN
CHRISTIEN	Frédéric	PR	Science et génie des matériaux	SMS
DAUZERE-PERES	Stéphane	PR1	Génie Industriel	CMP
DEBAYLE	Johan	MR	Sciences des Images et des Formes	SPIN
DEGEORGE	Jean-Michel	MA(MDC)	Génie industriel	Fayol
DELAFOSSE	David	PR0	Sciences et génie des matériaux	SMS
DELORME	Xavier	MA(MDC)	Génie industriel	FAYOL
DESRAYAUD	Christophe	PR1	Mécanique et ingénierie	SMS
DJENIZIAN	Thierry	PR	Science et génie des matériaux	CMP
DOUCE	Sandrine	PR2	Sciences de gestion	FAYOL
DRAPIER	Sylvain	PR1	Mécanique et ingénierie	SMS
FAUCHEU	Jenny	MA(MDC)	Sciences et génie des matériaux	SMS
FAVERGEON	Loïc	CR	Génie des Procédés	SPIN
FEILLET	Dominique	PR1	Génie Industriel	CMP
FOREST	Valérie	MA(MDC)	Génie des Procédés	CIS
FRACZKIEWICZ	Anna	DR	Sciences et génie des matériaux	SMS
GARCIA	Daniel	MR(DR2)	Sciences de la Terre	SPIN
GAVET	Yann	MA(MDC)	Sciences des Images et des Formes	SPIN
GERINGER	Jean	MA(MDC)	Sciences et génie des matériaux	CIS
GOEURIOT	Dominique	DR	Sciences et génie des matériaux	SMS
GONDRAN	Natacha	MA(MDC)	Sciences et génie de l'environnement	FAYOL
GONZALEZ FELIU	Jesus	MA(MDC)	Sciences économiques	FAYOL
GRAILLOT	Didier	DR	Sciences et génie de l'environnement	SPIN
GROSSEAU	Philippe	DR	Génie des Procédés	SPIN
GRUY	Frédéric	PR1	Génie des Procédés	SPIN
GUY	Bernard	DR	Sciences de la Terre	SPIN
HAN	Woo-Suck	MR	Mécanique et ingénierie	SMS
HERRI	Jean Michel	PR1	Génie des Procédés	SPIN
KERMOUCHE	Guillaume	PR2	Mécanique et Ingénierie	SMS
KLOCKER	Helmut	DR	Sciences et génie des matériaux	SMS
LAFOREST	Valérie	MR(DR2)	Sciences et génie de l'environnement	FAYOL
LERICHE	Rodolphe	CR	Mécanique et ingénierie	FAYOL
MALLIARAS	Georges	PR1	Microélectronique	CMP
MOLIMARD	Jérôme	PR2	Mécanique et ingénierie	CIS
MOUTTE	Jacques	CR	Génie des Procédés	SPIN
NEUBERT	Gilles			FAYOL
NIKOLOVSKI	Jean-Pierre	Ingénieur de recherche	Mécanique et ingénierie	CMP
NORTIER	Patrice	PR1	Génie des Procédés	SPIN
O CONNOR	Rodney Philip	MA(MDC)	Microélectronique	CMP
OWENS	Rosin	MA(MDC)	Microélectronique	CMP
PERES	Véronique	MR	Génie des Procédés	SPIN
PICARD	Gauthier	MA(MDC)	Informatique	FAYOL
PIJOLAT	Christophe	PR0	Génie des Procédés	SPIN
PINOLI	Jean Charles	PR0	Sciences des Images et des Formes	SPIN
POURCHEZ	Jérémy	MR	Génie des Procédés	CIS
ROUSSY	Agnès	MA(MDC)	Microélectronique	CMP
ROUSTANT	Olivier	MA(MDC)	Mathématiques appliquées	FAYOL
SANAUR	Sébastien	MA(MDC)	Microélectronique	CMP
STOLARZ	Jacques	CR	Sciences et génie des matériaux	SMS
TRIA	Assia	Ingénieur de recherche	Microélectronique	CMP
VALDIVIESO	François	PR2	Sciences et génie des matériaux	SMS
VIRICELLE	Jean Paul	DR	Génie des Procédés	SPIN
WOLSKI	Krzystof	DR	Sciences et génie des matériaux	SMS
XIE	Xiaolan	PR0	Génie industriel	CIS
YUGMA	Gallian	CR	Génie industriel	CMP

Mise à jour : 03/02/2017

École Nationale Supérieure des Mines
de Saint-Étienne

NNT : *Communiqué le jour de la soutenance*

Magali FERRO

Development of conducting polymer devices for the monitoring of 3D barrier tissue models

Speciality: Bioelectronics

Keywords: Barrier tissue, ionic selectivity, tight junctions, 3D *in vitro* cell models, organic electrochemical transistor

Abstract

In vitro cell models are widely accepted platforms for toxicological studies and drug screening. However starting from the conventional 2D models, improvements are needed to reproduce the native physiological environment of the targeted tissue. As they usually represent the first line to cross for the adsorption of substances, barrier tissues are extremely interesting for toxicology and drug delivery. Major advances in the field of tissue engineering have given rise to barrier tissue models that accurately recreate cell-cell and cell-matrix 3-dimentional interactions. However, the development of characterization platforms to quantify the permeability of barrier tissue models hasn't followed the rapid pace of complexification of the biological models. In this work I explore the possibilities to design conductive polymer-based devices adapted for the characterization of 3D barrier tissue models.

The regulation of passive ion diffusion across barrier tissues mostly happens through the paracellular route. Electrical measurements are traditionally used to quantify ion flow across barrier tissues and evaluate integrity and tightness of these tissues. Conventional electrical tools are made of metal electrodes placed on each side of the barrier tissue. They measure the current flow that crosses the cell layer. This technology suits most of the conventional 2D cell culture configurations. However, it presents limitations when it comes to

analyzing customized 3D tissue models due to size and stiffness issues in traditional electrical instruments.

As an alternative option to metal electrodes, organic electronic materials have shown great promise to interface with biological tissues. In particular the Organic ElectroChemical Transistor (OECT) using poly(3,4-ethylenedioxythiophene) doped with poly (styrene sulfonate) (PEDOT:PSS) has already shown great efficiency to quantify electrical properties of barrier tissues in 2D. Thanks to microfabrication techniques they can be miniaturized and tuned to form mechanically compliant interface with a range of biological tissues. PEDOT:PSS related volumetric capacitance improves OECT ionic conductance sensitivity.

In this thesis, OECT devices have been adapted to a range of 3D cell culture configurations for *in vitro* modeling of barrier tissues. Compatibility with models such as tracheal cell culture at the air-liquid interface, spheroid models and microvessel-on-a-chip system has been tested. The achievements described in this work present significant progress in the field of *in vitro* platforms of barrier tissue modeling for toxicology and drug discovery testing.

École Nationale Supérieure des Mines
de Saint-Étienne

NNT : *Communiqué le jour de la soutenance*

Magali FERRO

Développement de dispositifs à base de polymères conducteurs pour le suivi de modèles 3D de barrières tissulaires

Spécialité: Bioélectronique

Keywords: Barrière tissulaire, sélectivité ionique, jonctions serrées, modèle cellulaire *in vitro* 3D, transistor organique électrochimique

Abstract

La réglementation européenne des 3Rs (Remplacer, Réduire, Raffiner) impose de diminuer le nombre d'animaux utilisés à des fins de recherches scientifiques. Elle répond à des exigences éthiques en soutenant le développement de méthodes alternatives telles que les modèles cellulaires in vitro. Les récents progrès en micro-fabrication et techniques d'ingénierie tissulaire ont permis une avancée remarquable dans la complexification des plateformes de cultures cellulaires .Ces dernières favorisent l'agencement tridimensionnel (3D) des cellules et les interactions biophysiques et biochimiques avec leur microenvironnement. Elles ont favorisé le développement de modèles de tissus et organes en laboratoire capables de mimer les principales fonctions physiologiques du corps humain. Bien qu'elles soient primordiales, les plateformes de caractérisations cellulaires et tissulaires n'ont pas su suivre l'évolution rapide des modèles in vitro. Au cours de cette thèse nous évaluerons le potentiel des dispositifs électroniques à base de polymères conducteurs pour caractériser la sélectivité ionique des nouveaux modèles de barrières tissulaires.

Les protéines qui forment les jonctions serrées permettent la régulation de la diffusion passive des ions au travers des barrières tissulaires. Ces protéines se comportent comme des canaux sélectifs qui peuvent être dans un état ouvert ou fermé. Les outils conventionnellement utilisés pour quantifier le niveau de

sélectivité des barrières tissulaires sont composés d'électrodes en métal. Elles sont placées de chaque côté de la barrière et mesurent la capacité du tissu à conduire le courant électrique .Ces outils sont particulièrement bien adaptés pour les modèles 2D comme les Transwells®. En revanche, il est difficile d'intégrer ces électrodes au sein des nouveaux modèles 3D à cause de leurs tailles et de leurs rigidités.

Une des alternatives possibles à ces limitations repose sur l'utilisation des transistors organiques électrochimiques (OECTs) à base de PEDOT:PSS (poly(3,4- ethylenedioxythiophene) dopés par des anions de polystyrène sulfonate). Il s'agit d'un matériel organique conducteur qui a déjà montré son efficacité pour la caractérisation de barrières tissulaires de configuration plane. Contrairement aux électrodes en métal, les dispositifs à base de PEDOT:PSS présentent une capacitance volumétrique qui leur permet de détecter les changements de concentrations ioniques avec une sensibilité et une résolution spatiale améliorée Les OECTs offrent également une grande flexibilité de configuration. Ils pourraient ainsi être amenés à concurrencer les outils conventionnels pour la mesure de conductance ionique de barrières tissulaires intégrées au sein de nouvelles plateformes 3D.

Les travaux menés dans cette thèse ont permis de développer des plateformes électriques à base d'OECTs pour caractériser des sphéroïdes, des cultures cellulaires à l'interface air-liquide ou encore les systèmes 'organ-on-a-chip'. Ces plateformes représentent une avancée majeure dans le domaine des modèles in vitro pour les essais toxicologiques.

Acknowledgments

TO BE COMPLETED

Table of Contents

Chapter 1: Introduction **1**

1.1 Thesis overview 1

1.2 Collaborators 3

1.2.1 Collaborators for Chapter 2 3

1.2.2 Collaborators for Chapter 3 4

1.2.3 Collaborators for Chapter 4 4

1.2.4 Collaborators for Chapter 5 5

1.2.5 Collaborators for Chapter 6 5

1.3 References 6

Chapter 2: *In vitro* platforms to assess barrier tissue integrity **8**

2.1 Abstract 8

2.2 Introduction 8

2.2.1 Barrier tissues: structure and role 8

2.2.2 Barrier tissue disruption-related pathology 10

2.2.3 Toward a complexification of *in* vitro barrier tissue models 11

2.3 Barrier tissue *in vitro* characterization assay 12

2.3.1 Tight junctions regulate the paracellular diffusion 12

2.3.2 Assessing size selective pathway 13

2.3.3 Assessing charge selective pathway 15

2.4 Conclusion and Opportunities 18

2.4.1 A need for TEER measurement standardization 18

2.4.2 Using bioelectronic devices to characterize *in vitro* barrier tissues 19

2.5 References 22

Chapter 3: Effect of E cigarette emissions on tracheal cells monitored at the air-liquid interface using an organic electrochemical transistor **28**

3.1 Abstract 28

3.2 Introduction 28

3.3 Results 31

3.4 Discussion and Conclusion 41

3.5 Material & Method 42
3.6 Acknowledgments 46
3.7 References 46
Chapter 4: A planar impedance sensor for 3D spheroids 52
4.1 Abstract 52
4.2 Introduction 52
4.3 Results 54
4.3.1 Microtrap platform design 54
4.3.2 Microtrap platform performance 60
4.4 Discussion 66
4.5 Conclusion 68
4.6 Material & Method 69
4.7 Acknowledgments 72
4.8 References 72
Chapter 5: Dynamic blood brain barrier 3D model with integrated real-time electrical cell barrier monitoring 79
5.1 Abstract 79
5.2 Introduction 79
5.3 Results 81
5.3.1 Engineering 3D fluidic brain microvascular network 81
5.3.2 OECTs integration with organ-on-a-chip device 82
5.3.3 Blood brain barrier formation in 2D model vs 3D model 84
5.4 Discussion and Conclusion 85
5.5 Material & Method 86
5.6 Acknowledgments 88
5.7 References 88
Chapter 6: New materials for in vitro blood brain barrier models 92
6.1 Abstract 92
6.2 Introduction 92
6.3 The demand for in vitro models of the blood brain barrier 93
6.4 Structure and molecular composition of the blood brain barrier matrix 95
6.5 2D blood brain barrier models 98

6.5.1 Porous, non-degradable material for 2D blood brain barrier models 98
6.5.2 Matrix modeling as an important feature for vascular function 102
6.6 Degradable biomaterials as a matrix design element for 2.5D blood brain barrier models 104
6.6.1 Decellularized in vitro-secreted extracellular matrix 104
6.6.2 Electropsun membranes 105
6.6.3 Hydrogels 107
6.7 3D microvascular blood brain barrier models 111
6.7.1 General information about endothelial cell sprouting 112
6.7.2 Biomaterials for blood brain barrier vasculogenesis 113
6.7.3 3D pinting bioinks 115
6.8 Conclusion and future opportunities 116
6.9 References 119
Chapter 7: Conclusions **134**

List of Tables

Number *Page*

Table S3.2 Comparison of vaping parameters used in vitro versus human behavior 35

Table S3.4 E-cigarette aerosols composition. 36

Table 6.1 Overview of the blood brain barrier basal membrane composition 97

Table 6.2 Porous non degradable substrates for 2D BBB cell culture 101

Table 6.3 Biomaterials used to replace porous membrane for 2.5D model 109

Table 6.4 Summary of new materials for BBB modeling and mechanical stimuli associated with investigate/improve cell-matrix interactions. 117

List of Figures

Number *Page*

Figure 2.1 Diversity of barrier tissues in the body 9

Figure 2.2 Cell barrier junctional complexes 10

Figure 2.3 Mechanism of diffusion regulated by tight junctions 13

Figure 2.4 Permeability assays to assess size selective diffusion..... 15

Figure 2.5 Electrical platforms to assess charge selective diffusion 17

Figure 2.6 Typical organic electrochemical transistor structure 20

Figure 2.7 OECT devices integrated with 2D barrier tissues 22

Figure 3.1 Electrical Resistance Monitoring Platform for ALI Airway Epithelium Model 31

Figure 3.2 Fg-OECT device for continuous airway epithelium resistance monitoring 33

Figure S3.1 Fg-OECT-induced ciliary beating frequency variance 35

Figure S3.3 Kinetics of e-cigarette aerosol deposition. 36

Figure 3.3 E-cigarette aerosol-induced cytotoxicity on MucilAir^{TM} epithelium . 40

Figure 4.1 Microtrap platform design. 57

Figure 4.2 Spheroid impedance sensing 60

Figure 4.3 Size-selective microtrap platform performance. 62

Figure 4.4 Barrier-selective microtrap platform performance 64

Figure 4.5 Dynamic performance of the microtrap platform 66

Figure 5.1 Integration of OECTs within microvessel-on-a-chip device 83

Figure 5.2 Electrical characterization of blood brain barrier ionic permeability 84

Figure 6.1 Schematic representation of the neurovascular unit 96

Figure 6.2 Selected History of in vitro BBB Models 98

Figure 6.3 Porous non degradable substrate for 2D BBB models 100

Figure 6.4 Representative image of ZO-1 tight junction proteins 102

Figure 6.5 Decellularized cell secreted-ECM *in vitro* 105

Figure 6.6 Electropsun membrane for BBB 2.5D model 107

Figure 6.7 Strategies to move from 2D to 2.5D cell culture systems in a Transwell configuration 108

Figure 6.8 BBB-on-chips strategies 111

Figure 6.9 Hydrogel composition and casting conditions impact collagen fibrillary structure 115

Chapter 1: Introduction

1.1. Thesis overview

Nowadays, more than $2 billion and about 10 years are required to develop one new drug on average[1]. *In vitro* cell models represent a popular tool for drug testing as well as a convenient alternative to animal models. However, conventional flat cell culture fail to accurately predict what will happen in humans when they are treated with a drug. This may be due in part to a mismatch between how cells work in our body and the 2D *in vitro* models we use. This is mainly due to the interactions with the surrounding microenvironment. For example, the complexity of the blood brain barrier (BBB) is usually reduced to cell culture on a flat, stiff surface and diffusion of soluble growth factors, which doesn't take into account the matrix mechanical cues and cell-cell interactions. To address this global healthcare challenge, microphysiological systems that aim to mimic the native cell microenvironment through the 3D cell culture are on the rise.

In this thesis work, I present new approaches to characterize barrier tissues within a range of 3D cell culture platforms. I reasoned that preserving the integrity of both cell-cell and cell-matrix interactions will allow more predictive data in the field of drug testing and toxicological assays. To do so, I worked to interfaces and integrate bioelectronics with *in vitro* barrier tissues. Organic electrochemical transistor (OECT) represents an innovative device to interface with living tissue by recording ionic signals. OECTs are able to detect micromolar changes in ionic concentration with a millisecond temporal resolution[2]. They have been successfully used to characterize ionic barrier tissue selectivity in 2D configurations. We took advantage of the OECT flexibility to design compact devices that match with 3D barrier tissue models.

To begin with, in chapter 2, I bring a broad overview of barrier tissue structure and physiological functions. It details the molecular organizations of tight junction proteins that not only bridge endothelial or epithelial cells but also regulate ions and solutes passive diffusion across barrier tissue. I review the main features of 2D and 3D barrier tissue *in vitro* models and present available

characterization platforms to assess ionic and solute barrier selectivity. Firstly designed for 2D models, most of these platforms present technical limitations. Because of this, they end up giving contradictory results when integrated within 3D cell culture systems. Thus OECTs are introduced as a promising way to overcome these challenges. Made of organic materials, they benefits from miniaturization thanks to their fabrication *via* photolithography and can easily be integrated within barrier tissues in a seamless and non-invasive way. They have been designed to monitor transepithelial resistance (TER) in a Transwell® model[3] as well as TER and cell coverage in a planar configuration[4].

In chapter 3, I present an electrical platform able to record for the first time ionic selectivity of tracheal cells under physiological conditions. Tracheal cells are part of the airway epithelium which makes a physical separation between the external and the internal environment. As a result, tracheal cells are usually cultured at the air-liquid interface (ALI), which improves tissue functions (ie mucus secretion and clearance). However, there is a mismatch between *in vitro* models and electrical platforms: current electrical monitoring systems are usually made of rigid metal electrodes and require the tissue to be fully-immersed in an electrolyte to operate. I propose to pattern organic material on a flexible electrode so ion exchanges happen through the cell-secreted mucus. I highlight specific cellular response to e-cigarette aerosols by performing for the first time continuous monitoring using an adapted flexible electrode OECT.

In chapter 4, I coupled an OECT with a microfluidic trapping device to assess spheroid impedance sensing. The production of spheroids falls within the rapid expansion of 3D cell models. The method consists in culturing adhesive cells on a non-attachable substrate and forcing them to agglomerate and secrete their own extracellular matrix. In that configuration, cell-cell and cell-matrix interactions are better preserved. However, there are only a few in-line monitoring platforms to study spheroids. In this chapter I show how I modified the conventional OECT fabrication protocol to integrate it with a polydimethylsiloxane (PDMS) microdevice to accurately measure the impedance of spheroids.

In chapter 5, compact planar OECTs are integrated into a BBB-on-a-chip system. The organs-on-chip technology offers the possibility to culture cells in

microfluidic tubes under highly controlled conditions. Mechanical forces can be applied to the PDMS chip to mimic physiological events such as breathing and blood pressure. The integration of rigid metal electrodes within micron-size chambers of organ-on-a-chip device remains challenging. In this section I detail a method to integrate multiple OECTs along microvessel-networks designed into a collagen matrix. I introduce how OECTs enable to accurately compare *in vitro* BBB functions in 2D configuration with 3D configuration.

In chapter 6, I review the new materials used to improve *in vitro* BBB models. The BBB is constituted by microvascular endothelial cells that form a highly selective ionic barrier. They are surrounded by several cell types (including astrocytes and pericytes) and also by a defined matrix called the basal membrane (BM). BBB endothelial cells require several biochemical and physical cues coming from the surrounding environment, which render the tissue difficult to reproduce on the bench. I highlight materials that have been used to mimic native tissue microstructure. I partly focus on matrix mechanical features to improve BBB ionic selectivity. BBB is also surrounded by neurons that generate electrical signals. There is therefore an interest in understanding how BBB react after electric stimulation. The use of organic conducting materials is envisioned as promising because it electrically conducts substrate to culture BBB endothelial cells.

The thesis ends with conclusions and suggested areas of continued scientific investigation (see Chapter 7 Conclusions).

Each chapter starts with a list of Collaborators who contributed to the work presented in that chapter and ends with a comprehensive list of references. Detailed contributions are provided for each chapter in the following section (section 1.2). At the beginning of each chapter, it is specified if the work presented has been published or submitted to a peer-reviewed journal at the time of submission of this thesis. For chapters presenting experimental results, a brief Materials & Methods section is also included within.

1.2. Collaborators

1.2.1. Collaborators for Chapter 2

Information contained within this chapter was compiled and written independently. There are no collaborators for this chapter.

1.2.2. Collaborators for Chapter 3

Collaborators: Dr Lara Leclerc[1], Dr Mohamad Sleiman[2], Bastien Marchiori[3], Dr Jérémie Pourchez[1], Dr Roisin M. Owens[4,5]* and Dr Marc Ramuz[3]*

[1]*Mines Saint-Étienne Department of Biomaterials and Inhaled Particles*

[2] *Sigma Clermont Department of Photochemical*

[3]*Mines Saint-Étienne Department of Flexible Electronics*

[4]*Mines Saint-Étienne Department of Bioelectronics*

[5]*Cambridge University Department of Chemical Engineering and Biotechnology*

Contributions: Various collaborators contribute to this work. The project was first initiated by both Dr Ramuz and Dr Owens. Dr Ramuz set parameters for pulse-time response recording after introduction of tracheal barrier tissue and adapted the Matlab code for the extraction of the time constant. B. Marchiori prepared OECTs using glass substrates and polyurethane materials. Dr Leclerc and Dr Purchez helped to define e-cigarette aerosol treatment conditions and made analysis of vapor deposition cinetic. Dr Sleiman leaded the analysis of e-cigarette vapor composition. M. P. Ferro defined the experimental setup and made cellZscope measurements. Data collection and analysis were made by both Dr Ramuz and M. P. Ferro.

1.2.3. Collaborators for Chapter 4

Collaborators: Dr Vincenzo F. Curto[1], Federica Mariani[2], Dr Erica Scavetta[2], Dr Roisin M. Owens[1,3]

[1]*Mines Saint-Étienne Department of Bioelectronics*

[2]*Universita di Bologna, Departimento di Chimica Industriale*

[3]*Cambridge University Department of Chemical Engineering and Biotechnology*

Contributions: The project was initiated by both Dr Curto and Dr Owens. Dr Curto designed the microfluidic chip and the OECT platform as well as the experimental setup. F. Mariani developed the chemistry formula to improve adhesion of PEDOT:PSS film on top of the gold. M. P. Ferro optimized the

protocol for spheroid mono- and co-culture and made immunostaining and imaging of spheroids. Dr. Curto and M. P. Ferro worked together to make OECT measurements and M. P. Ferro made data analysis. All collaborators were involved in the editing of this chapter.

1.2.4. Collaborators for Chapter 5

Collaborators: Dr Vincenzo F. Curto[1], Dr Rayan Nagao[2], Dr Ying Zheng[2], Dr Roisin M. Owens[1,3]

[1]*Mines Saint-Étienne Department of Bioelectronics*

[2]*University of Washington Department of Bioengineering*

[3]*Cambridge University Department of Chemical Engineering and Biotechnology*

Contributions: Dr Curto first initiated the project and learned the technique of microvessel design into the collagen matrix from Dr Nagao and Dr Zheng (previously published paper). Dr Curto also adapted this technique and the design of OECTs to match both of them in a single sensing platform. M.P.Ferro made microvessel construction, assembly on the OECTs and cell culture into the device for each samples presented in that section. She collected and analyzed the data as well as the immunostaining images. Figure construction and writing were completed by M. P. Ferro.

1.2.5. Collaborators for Chapter 6

Collaborators: Dr Sarah Heilshorn[1], Dr Roisin M. Owens[2]

[1]*Stanford University Department of Material Science & Engineering*

[2]*Cambridge University Department of Chemical Engineering and Biotechnology*

Contributions: Dr Heilshorn proposed the subject of this review. Dr Owens and Dr Heilshorn provided consultation on the selection of relevant topics and specific case studies for inclusion within this chapter. They also provided relevant suggestions on the design of the figures. The review and compilation of chosen topics, final selection of case studies, figure reconstruction, and writing were completed by M. P. Ferro.

1.3. References

1. Schuhmacher, A., Gassmann, O. & Hinder, M. Changing R&D models in research-based pharmaceutical companies. *J*. *Transl*. *Med*. **14,** (2016).

2. Rivnay, J. *et al*. Using white noise to gate organic transistors for dynamic monitoring of cultured cell layers. *Sci*. *Rep*. **5,** 11613 (2015).

3. Jimison, L. H. *et al*. Measurement of Barrier Tissue Integrity with an Organic Electrochemical Transistor. *Adv*. *Mater*. **24,** 5919–5923 (2012).

4. Ramuz, M., Hama, A., Rivnay, J., Leleux, P. & Owens, R. M. Monitoring of cell layer coverage and differentiation with the organic electrochemical transistor. *J Mater Chem B* **3,** 5971–5977 (2015).

Chapter 2: *In vitro* platforms to assess barrier tissue integrity

Publication Status: *This chapter has not been published or submitted for publication at the time of submission of this thesis.*

Collaborators: *Information contained within this chapter was compiled and written independently. There are no collaborators for this chapter.*

2.1 Abstract

Tight junction proteins regulate the diffusion of ions and solutes across a barrier tissue. The selectivity of diffusion mainly happens through the charge and the size of the solute or ion. We review main techniques to assess barrier tissue selectivity, including permeability assays and trans-epithelial -endothelial electrical resistance. These techniques are challenging to integrate within recent 3D cell culture platforms. I highlight organic electrochemical transistors (OECTs) to characterize *in vitro* barrier tissues. The easy processing and chemical tunability of organic material makes OECTs particularly suitable for integration with 3D barrier tissue models.

2.2 Introduction

2.2.1 Barrier tissues: structure and role

Most tissues and organs require a well-defined microenvironment to accomplish their function. Barrier tissues are made of juxtaposed endothelial or epithelial cells. They guarantee tissue homeostasis by regulating exchanges of solutes between two compartments. Epithelium/ endothelium cellular organization depends on physiological function of the tissue in question. Thus, barrier tissues that make the separation between the internal and the external environment are usually thick and stratified to protect the body from physical or chemical damages. However, a simple monolayer of cell line internal organs, can also allow rapid gas and nutrient exchanges between the external environment and the underlined blood vessels (**Figure 2.1**). Vascular and lymphatic systems are made of endothelial cell monolayers. Mural cells, including pericytes and smooth

muscular cells, wrap around the endothelial cells to increase blood pressure mechanical strain resistance. The morphology of endothelial cells that forms blood or lymphatic capillaries is function-dependent. Fenestrated endothelium is found in tissues that are involved in filtration and secretion, while continuous endothelium is associated with highly selective barrier[1].

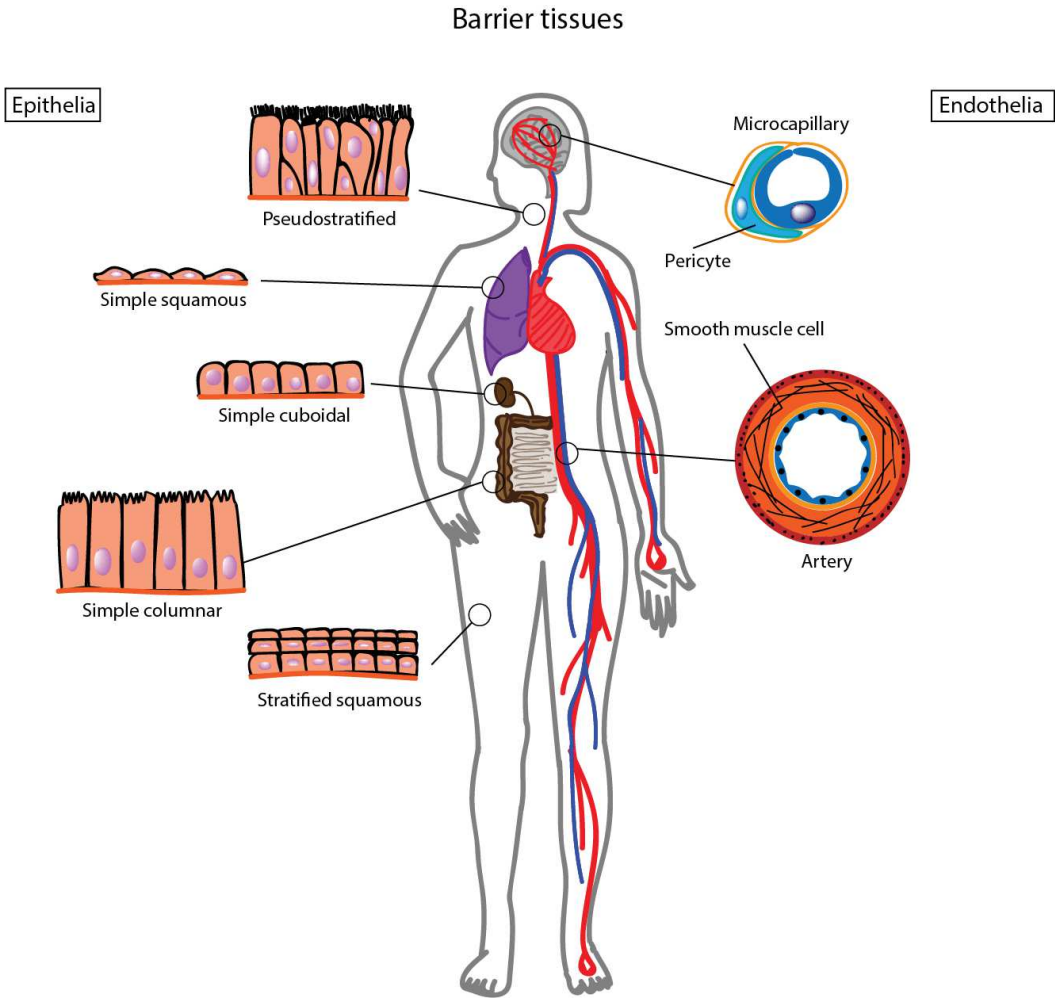

Figure 2.1: Diversity of barrier tissues in the body. ***a)*** *Illustration of barrier tissue diversity along the organism. On the left, epithelia showing cellular organization and shape diversity depending on the tissue function. On the right, endothelial cells that form blood vessels.*

The primary physiological role of barrier tissue is to regulate solute and ion exchanges between two compartments. The regulation of passive ion and solute diffusion mainly happens through lateral junction proteins that bridge the cells. Among these proteins, adherens junctions (AJs), which cadherins are core components, act as cell-cell adhesion complexes[2]. Tight junction (TJ) proteins are mainly composed of claudins and occludins that present an extracellular loop able

to interact with the loop from the neighboring cell to seal the intercellular gap[3]. The intracellular loop links with cell actomyosin cytoskeleton (actin filaments and microtubules) *via* adaptor proteins including zona occludens (ZO) (**Figure 2.2**). TJs and AJs are usually closely associated and reside at the apical end of the lateral membrane and are referred to as the 'apical junctional complex'.

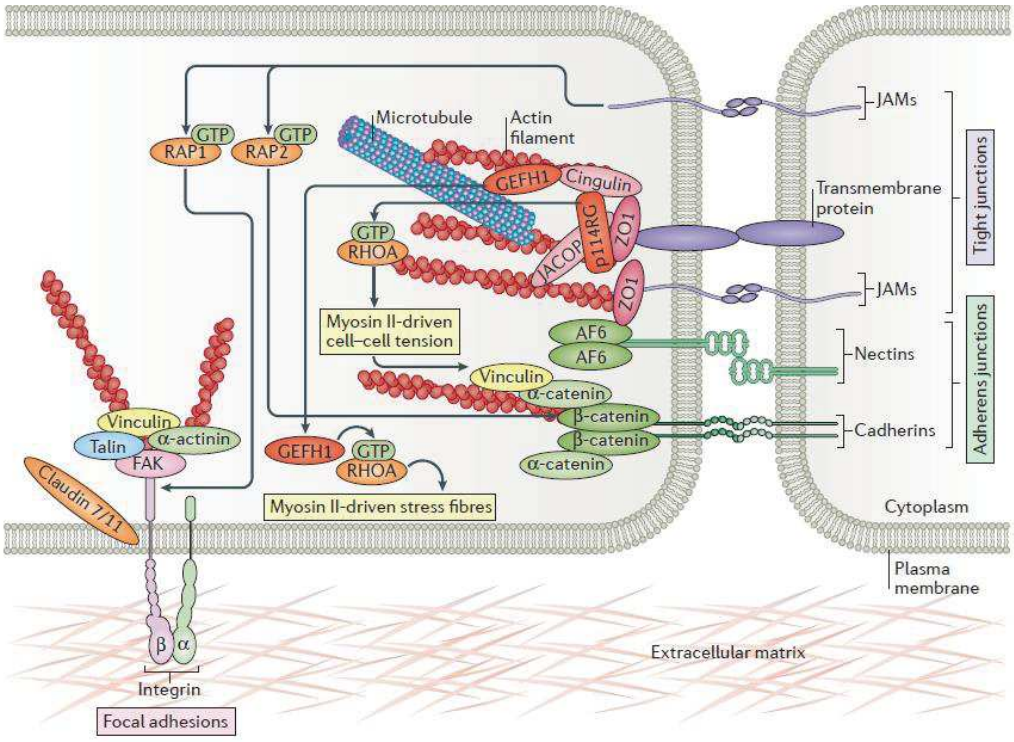

Figure 2.2: Cell barrier junctional complexes. *Representation of junctional complexes that bridge the cell with neighboring cell and surrounding ECM. It includes tight junction proteins that interact with the internal cellular cytoskeleton via cytosolic plaques* [3].

2.2.2 Barrier tissue disruption-related pathology

Barrier tissues guarantee organ and tissue homeostasis. Hence, disruption of barrier tissues might be an integral part of many disease pathophysiologies. Loss of barrier properties might be the consequence of tissue destruction as well as TJ network disruption. The latter may be induced by pathogenic agents able to modify junctional protein synthesis, interaction, distribution and phosphorylation status.

A couple of examples illustrate the relation between barrier tissue disruption and diseases pathology. E-cadherin expression was decreased in bronchial

epithelial cells from subjects with asthma crisis[4]. Abnormal TJ structure causes an increase in intestinal epithelium permeability and has been correlated to celiac disease, an immune-mediated disorder of the small intestine triggered by gluten intolerance[5,6]. This junctional complex was also found of major importance in both inflammatory bowel disease and irritable bowel syndrome[7]. Blood brain barrier disruption has been involved in several neurodegenerative disorders including Alzheimer's disease, Parkinson's disease, and multiple sclerosis.[8]

2.2.3 Toward a complexification of *in vitro* barrier tissue models

The first successful *in vitro* cell culture was led by Katherine Sanford & co-workers in 1948. Cells were cultured in a petri-dish within an arbitrary formulated cell culture media. Since then, the influence of surrounding biochemical and physical signaling cues on cell and tissue functions has been largely demonstrated. Hence, the design of cell culture systems, which provide cell with a defined microenvironment increased drastically[9].

Transwell® inserts (referred to as 'transwells' in the rest of the chapter) are usually made of track etched polycarbonate (PC) or polyethylene terephthalate (PET) suspended membranes. They offer the possibility to culture cells on either side of the membrane while leaving free access to the manipulator in both compartments. Transwells have been thus a widely used system to model *in vitro* barrier tissues, in particular for toxicology assays and drug screening. Although this system offers many technical advantages, cells grow on a flat and stiff surface, which strongly limit cell-cell and cell-matrix interactions. Since 2010, the convergence of microfabrication techniques with tissue engineering paved the way for a new class of microphysiological systems[10]. They offered to synthesize minimal functional units that recapitulate key tissue functions within a device about the size of a computer memory stick. They are referred to as organ-on-a-chip systems and are composed by two polydimethylsiloxane (PDMS) layers that define microfluidic channels. These micron-size chambers are continuously perfused and cells are seeded either on a horizontal porous membrane or along the wall of the tube[11]. From a technical point of view, organ-on-a-chip device offers an advantage to decrease required cell numbers and biological reagent quantity.

2.3 Barrier tissue *in vitro* characterization assay

There are two main ways for a solute or an ion to cross a barrier tissue: across the cell (*via* transcellular route) or in between the cells (*via* paracellular route). The passive diffusion of solute and ions along the paracellular route is mainly regulated by TJ proteins that apply a selective diffusion based on molecule size and charge.

2.3.1 Tight junctions regulate the paracellular diffusion

Freeze fracture electron microscopy of epithelial tissues done in 1973 revealed junction organization in fibril meshwork. At the interface between two or three adjacent cells, tight junction proteins allow the close proximity of neighboring cell membrane by an interlacing of protein extracellular loops. It results in an apparent hemifusion of lipid bilayers shown as 'kissing' points (**Figure 2.3a**). These points prevent the lateral diffusion of transmembrane proteins and participate to the establishment of an apico-basal polarization. Tetraspan proteins of the claudin family and MARVEL domain proteins including occludins represent main components of TJs. TJs provide physical tissue stability and participate to the selective property of barrier tissues.

Nowadays, we describe two junctional paracellular pathway routes depending on selection parameter: (1) *size selective permeation pathway* regulates the diffusion of larger solutes and macromolecules of 30-60 Å. (2) *charge selective permeation pathway* regulates the diffusion of ions and uncharged small molecules through pores of about 4-8 Å (**Figure 2.3b**). Evidence has led to the conclusion that pores are gated, however the underlying mechanism is still unknown. Claudins are an important determinant of the charge selective pathway. Depending on their isotypes, they support cation selectivity (claudin-2), anion selectivity (claudin-17) or sealing property (claudin-1).

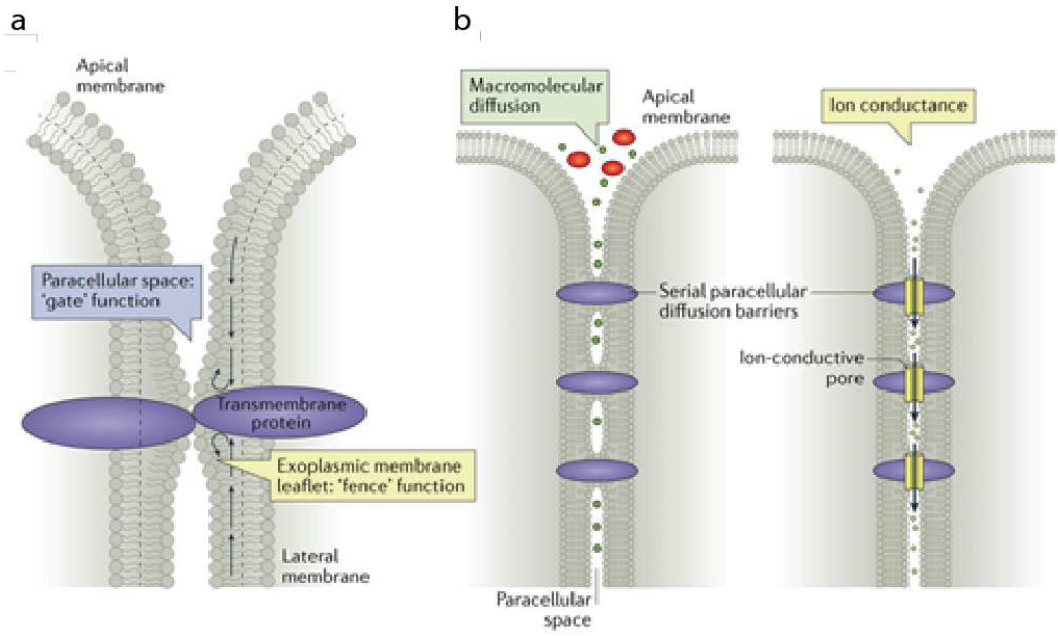

Figure 2.3: Mechanism of diffusion regulated by tight junctions. ***a)*** *Illustration of gate and fence functions of tight junctions. It regulates the lateral diffusion of lipids and proteins along the cell membrane.* ***b)*** *Illustration of macromolecular and ionic passive diffusion regulation by tight junctions. From* [3]

Several assays have been developed in order to visualize TJ proteins and estimate paracellular selectivity. Western blotting and confocal microscopy are two powerful complementary techniques that can allow the visualization and quantification of TJ proteins, in particular claudins and occludin. In the case of confocal microscopy, these proteins are coupled to fluorescent labels, which emission intensity provides a quantitative measure of the junctional network development. However, due to the highly-time consuming of this method, it is not scalable to high throughput

2.3.2 Assessing size selective pathway

The size selective pathways can be visualized by mixing chomophore, fluorophore, or radioisotope labeled tracers on one side of the barrier tissue to create a gradient of concentration. By measuring the time required for the tracer to diffuse through the barrier and reach the other compartment, we can evaluate their passive diffusion rate. Lucifer yellow or Fluorescein isothiocyanate (FITC) coupled dextran or albumin are among the most used macromolecule markers of paracellular permeability and offer a range of molecular size from 3 to 70 kDa.

Permeability assays are quite easy to operate in transwell cell culture configuration as the water-soluble tracer diffuse homogeneously in each compartment. The manipulator, who has easy access to both sides of the cell barrier, collects samples at determined time points and analyse the intensity of fluorescence overtime (**Figure 2.4a, left**). However, it necessities another strategy leading permeability assay on 3D barrier tissues when surrounded by viscoelastic hydrogel. Indeed, gel viscosity slow down the diffusion of the dye. Recently, a method based on confocal microscopy analysis has been developed to evaluate permeability of vascular organ-on-chip system. Then, region of interests (ROIs) have been defined around the tubular structure lined by endothelial cells and a conversion from green fluorescence to color map using image analysis software for determining the variation of intensity of FITC-dextran's fluorescence in the collagen gel surrounding the capillary (**Figure 2.4a, right**). [12] This technique provides a rapid and cost-effective means of assessing size selective diffusion through barrier tissues over a wide range of molecular size without the need of additional equipment. However, this technique gives an integral permeability measurement and do not allow for new molecules to determine if the diffusion happens through the paracellular or the transcellular route. Progress in lithographic techniques on silicon substrates overcomes these limitations by designing micro-cuvette-like structure on the top of a silicon chip on which cells can be cultivated. The density of a micro-cuvette is high enough to underline most of the cellular membrane and intercellular space. After the dye crosses the cell barrier it fills the pores underneath the cell. This technique improves spatial resolution of macromolecular selective diffusion assay (**Figure 2.4b**).[13] As another alternative, FITC-conjugated avidin dispersed in the culture media interact with biotin bound to viscoelastic hydrogels through a high-affinity interaction. The technique allows improvement in assay spatial resolution while offering the possibility to use cell culture substrates with improved mechanical properties such as collagen or gelatin (**Figure 2.4c**).[14]

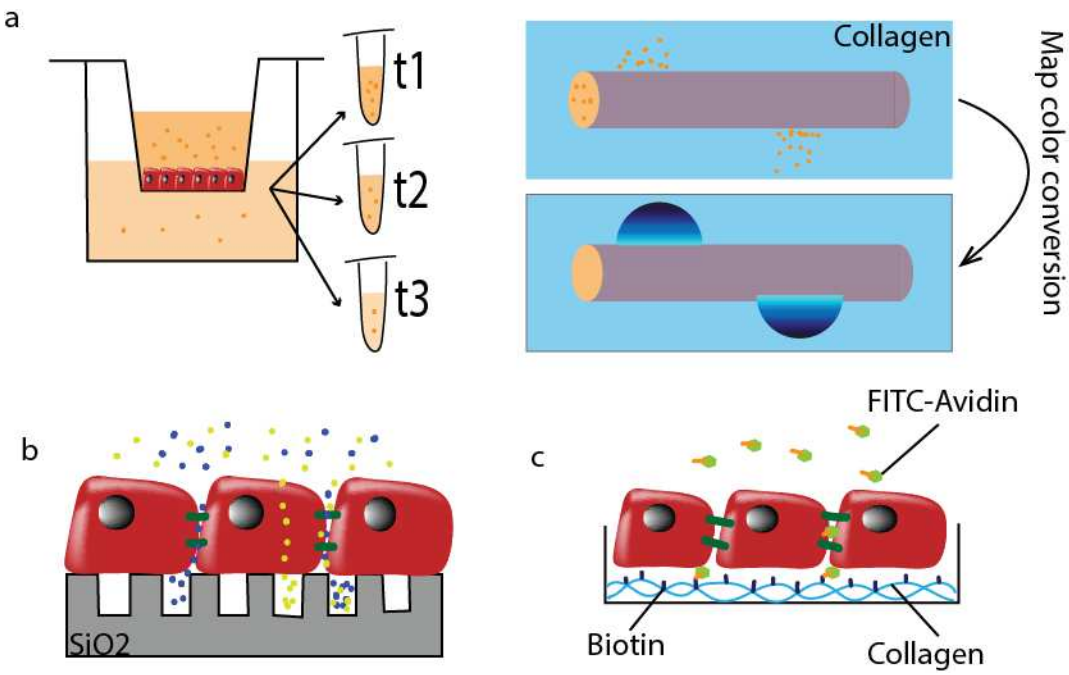

Figure 2.4: Permeability assays to assess size selective diffusion. ***a)*** *Using Transwell inserts, the tracer is added on one side of the cell barrier and samples are collected from the opposite side at defined time points to investigate tracer diffusion rate (on the left). Similarly, for organ-on-chip systems, the tracer is added into the tubular structure and let to diffuse through the barrier into the surrounding material such as collagen gel. Diffusion rate is determined using image analysis and color map transformation (on the right).* ***b)*** *Improvement of the spatial resolution in permeability assay can be reach through the design of micro-cuvette onto silicon substrate or* ***c)*** *biotin-avidin interactions.*

Permeability assays are time-consuming and the lack of automatization makes this technique irrelevant for high-throughput screening. Moreover, the use of tracers can interfere with the transport process under study but also barrier integrity, making tested cells unusable for further experiments.

2.3.3 Assessing charge selective pathway

Contrary to permeability assays, techniques to assess charge selective diffusion are usually rapid, label free, and largely easy to automate. These techniques require two metal electrodes that are placed on either sides of the barrier tissue. A direct current (DC) or an alternative current (AC) voltage signal is applied to the electrodes, which forces the ionic current to flow across the cell barrier. The corresponding inter-electrode resistance value is calculated as the ratio between the voltage and the resulting current. Due to the high resistance of

cell membranes, and the small conductance of ions through the cell membrane, the current predominantly flows through a paracellular route, making the resistance of the tissue approximately equal to the resistance of the TJs. The trans-epithelial/endothelial electrical resistance (TEER) is thus defined by multiplying the inter-electrode resistance by the barrier tissue area.

Electric cell-substrate impedance spectrum (ECIS) has been first used in 1984 to monitor fibroblast shape and behavior. In that system, cells are cultured directly on top of metal electrodes and an AC voltage signal is applied. The presence of cells induces a capacitive effect between the conductive cell media and the electrode. It allows a quantifiable cell spread and number.[15] The AC voltage is usually applied over a range frequency going from 1Hz to 1MHz. [16] It allows the measurement of both cell capacitance and resistance. The design of an electrical equivalent circuit shows the ion flow pathways across a barrier tissue (**Figure 2.5a**). At low frequency range (kHz) most of the ion flows through the paracellular route. The resistance of ion flow along the basal membrane (Rseal) may be very high due to the presence of cell-matrix anchor proteins.[17] ECIS has been rapidly adapted for the quantification of cell barrier paracellular ionic transport exploring the resistive impact of TJ selective permeation pathway.[18] Several commercial systems based on multi-electrode array have been developed including ECIS (Applied BioPhysics, Troy NY) and xCELLigence (RTCA Systems-ACEA Biosciences Inc.) modules. They are widely used during high throughput screening assays.

The possibility to carry out both permeability assays and TEER measurement in parallel might give valuable insights about barrier tissue functions. Recently, the design of cell culture substrate that contains microgrooves have been integrated with a blood-retinal barrier organ-on-a-chip system.[19] The microgroove surface was coated with gold to perform ECIS measurements while permeability assays were performed following the same protocol as previously described (Figure 2.4c).

Spheroids are valuable models for high throughput screening assays. However, spheroid impedance sensing is very challenging as the cells do not adhere to the electrodes anymore. Several platforms have been designed including microfluidic channels [20] and microcavity trap[21] in order to maintain the spheroid

in between gold electrodes (**Figure 2.5b**). In the latter microelectrodes are designed on the four sides of the cavity and monitor two independent bipolar EIS measurements using a frequency range of 133 kHz. However, spheroid placement between the electrodes may induce resistance variation that are difficult to extract.[21] To overcome this issue, a new platform composed by a central channel confined by retaining pillars has been designed. Coplanar EIS electrodes are placed in the center of the channel and the full device is placed on a tilting stage. The spheroid is placed within the channel and is allowed to roll by gravity back and forth on top of the electrode. Impedance measurements are thus recorded in a dynamic way.[22]

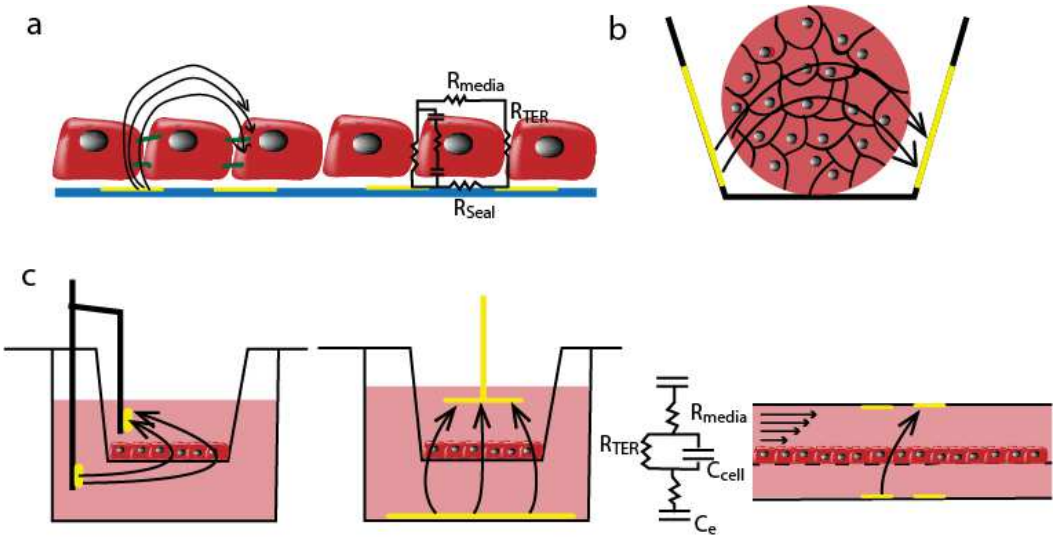

Figure 2.5: Electrical platforms to assess charge selective diffusion. *ECIS platform for barrier tissue impedance sensing. Cells are cultured on top of planar metal electrodes (**a**) or in a spheroid configuration (**b**). **c**) TEER platforms developed for transwell insert (left and middle) and organ-on-a-chip system (right). Illustrations show the ion flow (black arrow) and the related equivalent circuit.*

Cell impedance sensing is also widely performed on transwells. In this configuration, metal electrodes are placed in the upper and lower compartments (**Figure 2.5c**). Commercial modules to perform TEER measurements in transwells include the Epithelial Voltohmmeter (EVOM2, World Precision Instruments, Sarasota, FL) and the cellZscope (nanoAnalytics GmbH, Germany). The EVOM2, also referred as 'chopstick', applies a low AC voltage squared signal (~10 μA) with a signal frequency of 12.5 Hz. The TEER is calculated following the Ohm's law. The assumption of non-conducting cells is valid, because at low frequency

AC, capacitive impedance offered by the lipid bilayer is significantly higher than the junctional resistance, channeling the electric current through the 'path of least resistance'[23]. The cellZscope module provides an impedance spectroscopy measurement to give a more accurate representation of TEER. Amplitude and phase of the resulting current is analyzed over a range of frequency from 1Hz to 1MHz and the cell layer impedance is calculated as $Z = V(t)/I(t)$. The impedance spectrum shows three distinct frequency regions that are dominated by specific equivalent circuit elements.[24]

The micrometer-size of organ-on-a-chip chambers rends difficult barrier tissues access. Thus integrating rigid metal electrodes into the system turns out to be challenging. Electrode wires are slipped into the tubular chamber, however there are risks of cell damage and device contamination. To overcome this limitation, micropatterned electrodes may be embedded into PDMS layers (Figure 5c, right).

2.4 Conclusion and opportunities

2.4.1 A need for TEER measurement standardization

Brain microcapillary ionic resistance was measured *in vivo* for the first time in 1982 and serves today as a strong reference in the field of blood brain barrier. Two set of electrodes were placed within the capillary. The ion permeability was supposed to be constant along the structure and the loss of potential was expressed as a function of capillary length, thus TEER was reported in $\Omega.cm^2$. To compare *in vitro* TEER value with *in vivo* recordings, commercial systems were used to divide the calculated resistance by the cell layer surface, although this method is only valid if the current flow is uniform across the barrier. Non-uniform current density is one of the main reasons for erratic TEER values in customized microfluidic systems. The tissue segment closes to the electrodes may participate more to the ion flow than the rest of the structure, which results in an overestimation of the effective area and thus of the TEER value.

Additional factors including media conductivity, electrode size and distance from the cell layer induce artifactual differences in measured barrier tissue resistance. If the cell barrier can easily be moved in and out from the electrodes

the contribution of these variables is reduced by subtracting a blank resistance. However, this method is prone to error for organ-on-a-chip systems as electrode placement and media conductivity may vary between the blank system and the tissue-containing system.[25] Four electrodes were used (two electrodes placed on each side of the cell barrier) in a microfluidic device to generate six resistance measurements and calculate a TEER value independent of channel properties. [26,27] Mathematical models are able to describe customized systems using the finite element analysis method and separate raw resistance coming from the system itself and from a biological event.[28,29]

Nowadays, there is still a missing practical and standardized approach to integrate electronic devices into the newly developed microphysiological systems.[19,30,31] One way to overcome this issue has been to match the shape of the *in vitro* system with conventional transwell membrane and use commercial systems to measure TEER value.[32] Although this method makes easier the comparison with published data, it obviously limits the design of the microsystem.

2.4.2 Using bioelectronic devices to characterize *in vitro* barrier tissues

Bioelectronic materials couple signals from electronic devices and biological systems. They might transduce biological event into electronic recordings and generate biological response through electronic stimulation. The field of bioelectronics date from the work of Luigi Galvani (18th century) who made a detached frog legs twitch by applying a small voltage to the muscle. Today, bioelectronic devices principally extend to the medical field. Biosensors have been developed to improve healthcare, including glucose sensor for diabetics and pacemaker to support heart failure. Ultrathin implantable electrodes have been developed for brain electrical recording in accordance with the EU Flagship Initiative “Human Brain Project” and the US equivalent “Brain Activity Map”. Both projects started in 2013 with the aim to increase comprehension in brain activity and neurological diseases.[33]

The organic electrochemical transistor (OECT) is widely used to record ionic-based biological events. Developed by Wrighton and co-workers in the mid-

1980s, the OECT is composed by an organic semiconductor film that makes a channel between two metal electrodes called the source and the drain. A third electrode, the gate, is connected to the channel through an electrolyte (**Figure 2.6**). The working principle of an OECT relies on an oriented flow of holes or electrons through the channel and the injection of ions into the channel to change the conductivity of the organic film. A typical material for the OECT is the conducting polymer poly(3,4‑ethylenedioxythiophene) doped with poly(styrene sulfonate) (PEDOT:PSS). PEDOT is a p-type doped polymer, which lead to the creation of mobile holes able to hop from one PEDOT chain to another. When a negative drain voltage is applied, these holes are compensated by sulfonate anions of PSS and a drain current flow through the channel. It defines the ON state of the transistor. The OECT works in depletion mode, which means the application of a positive gate voltage lead to the injection of positive ions from the electrolyte into the conductive polymer bulk. These cations compensate PSS anions, which decreases the number of holes available in the channel and induces a drop in the drain current. It leads to the OFF state of the transistor. Contrary to metal electrodes, change in channel conductivity happens through the all volume of the film and not only at the interface with the electrolyte. Thanks to this volumetric response, the OECT transduces small gate voltage signals into large drain current variations. OECT transduction efficiency is illustrated by the transconductance ($g_m=\partial I_D/\partial V_G$), which is very high for the OECTs and an important figure of merit for transistors.[34]

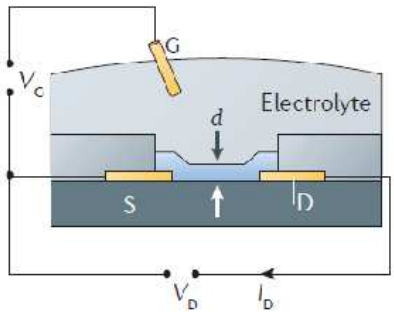

Figure 2.6: Typical organic electrochemical transistor structure. *The illustration shows the typical structure of the organic electrochemical transistor (OECT). It shows the source (S), drain (D) and gate (G) electrodes immersed into an electrolyte. d corresponds to the channel thickness. A drain voltage (V_D) and*

gate voltage (V_G) are applied to the system and the resulting drain current (I_D) is measured. From [34].

Bernards and Malliaras first investigated the use of OECT technology to characterize lipid bilayer. The bilayer lipid membrane (BLM) was placed in between the gate and the transistor channel. As lipid membrane act as ionic capacitors, the presence of an intact BLM fully suppress the gating of the OECT while the presence of ion channels partially restore it.[35] This experiment paved the way for the use of OECTs to characterize *in vitro* barrier tissues.

OECT has thus been integrated into transwell models for cell impedance sensing. In that configuration, the transistor channel is patterned at the bottom of the lower compartment, while the gate electrode is immersed into the upper compartment (**Figure 2.7a**). [36–38] Thus barrier tissue ionic selectivity impact OECT gating efficiency as fewer ions are allowed to penetrate the channel. Toxicology assay were successfully performed as barrier disruption restore the progressively the gating. In contrast to the transwell model, a planar model may also be envisaged. Cell culture on top of the channel transistor allows to differentiate simple cell coverage from cell barrier formation.[39,40] OECTs are easily represented by an RC circuit, which describe the electrolyte resistance and capacitance of both gate/electrolyte interface and PEDOT:PSS channel. The integration of an OECT with a barrier tissue, leads to an additional parallel RC circuit in series with the previous one, which corresponds to the resistance and capacitance of the cell layer (**Figure 2.7b**). Contrary to metal electrodes, PEDOT:PSS films are optically transparent, which allow cell layer visualization during impedance sensing. This optical property allowed to correlate electrical signals with visual information during a wound healing assay[41].

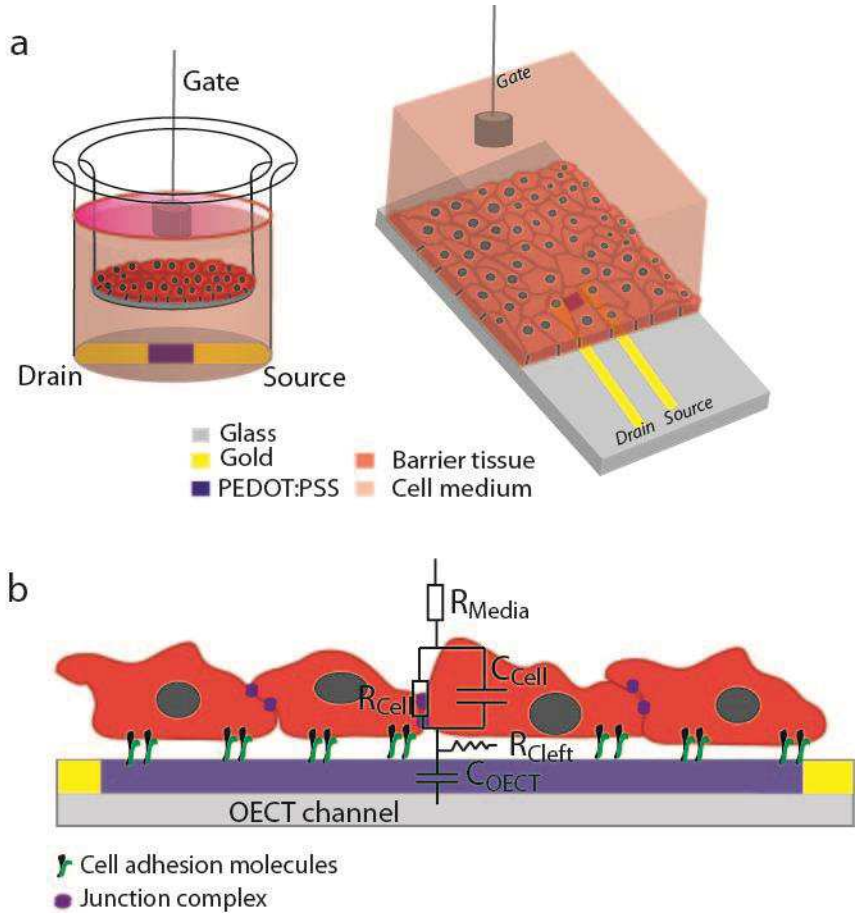

Figure 2.7: OECT devices integrated with 2D barrier tissues. ***a)*** *Illustration of an OECT integrated with transwell model (left) or within cell culture substrate (right).* ***b)*** *Electrical equivalent circuit showing resistance and capacitance of the cell layer (R_{Cell} and C_{Cell}) grown on top of the transistor channel. R_{Media} corresponds to the resistance of the media and C_{OECT} to the OECT capacitance. Cleft resistance (R_{Cleft}) describes the presence of cell adhesion molecules that regulate ion flow in parallel of the channel.*

2.5 References

1. Potente, M. & Mäkinen, T. Vascular heterogeneity and specialization in development and disease. *Nat. Rev. Mol. Cell Biol.* **18,** 477–494 (2017).

2. Harris, T. J. C. & Tepass, U. Adherens junctions: from molecules to morphogenesis. *Nat. Rev. Mol. Cell Biol.* **11,** 502–514 (2010).

3. Zihni, C., Mills, C., Matter, K. & Balda, M. S. Tight junctions: from simple barriers to multifunctional molecular gates. *Nat. Rev. Mol. Cell Biol.* **17,** 564–580 (2016).

4. Lambrecht, B. N. & Hammad, H. The airway epithelium in asthma. *Nat*. *Med*. **18,** 684–692 (2012).

5. König, J. *et al*. Human Intestinal Barrier Function in Health and Disease. *Clin*. *Transl*. *Gastroenterol*. **7,** e196–e196 (2016).

6. Schumann, M., Siegmund, B., Schulzke, J. D. & Fromm, M. Celiac Disease: Role of the Epithelial Barrier. *Cell*. *Mol*. *Gastroenterol*. *Hepatol*. **3,** 150–162 (2017).

7. Landy, J. *et al*. Tight junctions in inflammatory bowel diseases and inflammatory bowel disease associated colorectal cancer. *World J*. *Gastroenterol*. **22,** 3117 (2016).

8. Sweeney, M. D., Sagare, A. P. & Zlokovic, B. V. Blood–brain barrier breakdown in Alzheimer disease and other neurodegenerative disorders. *Nat*. *Rev*. *Neurol*. **14,** 133–150 (2018).

9. Sakolish, C. M., Esch, M. B., Hickman, J. J., Shuler, M. L. & Mahler, G. J. Modeling Barrier Tissues In Vitro: Methods, Achievements, and Challenges. *EBioMedicine* **5,** 30–39 (2016).

10. Zhang, B., Korolj, A., Lai, B. F. L. & Radisic, M. Advances in organ-on-a-chip engineering. *Nat*. *Rev*. *Mater*. **3,** 257–278 (2018).

11. Bhatia, S. N. & Ingber, D. E. Microfluidic organs-on-chips. *Nat*. *Biotechnol*. **32,** 760–772 (2014).

12. Pauty, J. *et al*. A Vascular Permeability Assay Using an *In Vitro* Human Microvessel Model Mimicking the Inflammatory Condition. *Nanotheranostics* **1,** 103–113 (2017).

13. Michaelis, S. *et al*. Macroporous silicon chips for laterally resolved, multi-parametric analysis of epithelial barrier function. *Lab*. *Chip* **12,** 2329 (2012).

14. Dubrovskyi, O., Birukova, A. A. & Birukov, K. G. Measurement of local permeability at subcellular level in cell models of agonist- and ventilator-induced lung injury. *Lab*. *Invest*. **93,** 254–263 (2013).

15. Giaever, I. & Keese, C. R. Monitoring fibroblast behavior in tissue culture with an applied electric field. *Proc*. *Natl*. *Acad*. *Sci*. **81,** 3761–3764 (1984).

16. Xu, Y. *et al*. A review of impedance measurements of whole cells. *Biosens*. *Bioelectron*. **77,** 824–836 (2016).

17. Buitenweg, J. R., Rutten, W. L. C., Willems, W. P. A. & van Nieuwkasteele, J. W. Measurement of sealing resistance of cell-electrode interfaces in neuronal cultures using impedance spectroscopy. *Med*. *Biol*. *Eng*. *Comput*. **36,** 630–637 (1998).

18. Tiruppathi, C., Malik, A. B., Del Vecchio, P. J., Keese, C. R. & Giaever, I. Electrical method for detection of endothelial cell shape change in real time: assessment of endothelial barrier function. *Proc*. *Natl*. *Acad*. *Sci*. **89,** 7919–7923 (1992).

19. Yeste, J. *et al*. A compartmentalized microfluidic chip with crisscross microgrooves and electrophysiological electrodes for modeling the blood–retinal barrier. *Lab*. *Chip* **18,** 95–105 (2018).

20. Hildebrandt, C., Büth, H., Cho, S., Impidjati & Thielecke, H. Detection of the osteogenic differentiation of mesenchymal stem cells in 2D and 3D cultures by electrochemical impedance spectroscopy. *J*. *Biotechnol*. **148,** 83–90 (2010).

21. Kloß, D., Fischer, M., Rothermel, A., Simon, J. C. & Robitzki, A. A. Drug testing on 3D in vitro tissues trapped on a microcavity chip. *Lab*. *Chip* **8,** 879 (2008).

22. Bürgel, S. C., Diener, L., Frey, O., Kim, J.-Y. & Hierlemann, A. Automated, Multiplexed Electrical Impedance Spectroscopy Platform for Continuous Monitoring of Microtissue Spheroids. *Anal*. *Chem*. **88,** 10876–10883 (2016).

23. Sun, T. *et al*. On-chip epithelial barrier function assays using electrical impedance spectroscopy. *Lab*. *Chip* **10,** 1611 (2010).

24. Srinivasan, B. *et al*. TEER measurement techniques for in vitro barrier model systems. *J*. *Lab*. *Autom*. **20,** 107–126 (2015).

25. Elbrecht, D. H., Long, C. J. & Hickman, J. J. Transepithelial/endothelial Electrical Resistance (TEER) theory and ap-plications for microfluidic body-on-a-chip devices. *tc* **1,** 1 (2016).

26. van der Helm, M. W. *et al*. Direct quantification of transendothelial electrical resistance in organs-on-chips. *Biosens*. *Bioelectron*. **85,** 924–929 (2016).

27. van der Helm, M. W. *et al*. Fabrication and Validation of an Organ-on-chip System with Integrated Electrodes to Directly Quantify Transendothelial Electrical Resistance. *J*. *Vis*. *Exp*. (2017). doi:10.3791/56334

28. Khire, T. S. *et al*. Finite element modeling to analyze TEER values across silicon nanomembranes. *Biomed*. *Microdevices* **20,** (2018).

29. Odijk, M. *et al*. Measuring direct current trans-epithelial electrical resistance in organ-on-a-chip microsystems. *Lab Chip* **15,** 745–752 (2015).

30. Henry, O. Y. F. *et al*. Organs-on-chips with integrated electrodes for trans-epithelial electrical resistance (TEER) measurements of human epithelial barrier function. *Lab Chip* **17,** 2264–2271 (2017).

31. Arık, Y. B. *et al*. Barriers-on-chips: Measurement of barrier function of tissues in organs-on-chips. *Biomicrofluidics* **12,** 042218 (2018).

32. Wang, Y. I., Abaci, H. E. & Shuler, M. L. Microfluidic blood-brain barrier model provides in vivo-like barrier properties for drug permeability screening: Microfluidic BBB Model Mimics In Vivo Properties. *Biotechnol*. *Bioeng*. **114,** 184–194 (2017).

33. Ferro, M. D. & Melosh, N. A. Electronic and Ionic Materials for Neurointerfaces. *Adv*. *Funct*. *Mater*. **28,** 1704335 (2018).

34. Rivnay, J. *et al*. Organic electrochemical transistors. *Nat*. *Rev*. *Mater*. **3,** 17086 (2018).

35. Bernards, D. A. & Malliaras, G. G. Steady-State and Transient Behavior of Organic Electrochemical Transistors. *Adv*. *Funct*. *Mater*. **17,** 3538–3544 (2007).

36. Jimison, L. H. *et al*. Measurement of Barrier Tissue Integrity with an Organic Electrochemical Transistor. *Adv*. *Mater*. **24,** 5919–5923 (2012).

37. Tria, S. A. *et al*. Dynamic Monitoring of *Salmonella typhimurium* Infection of Polarized Epithelia Using Organic Transistors. *Adv*. *Healthc*. *Mater*. **3,** 1053–1060 (2014).

38. Tria, S. A., Jimison, L. H., Hama, A., Bongo, M. & Owens, R. M. Validation of the organic electrochemical transistor for in vitro toxicology. *Biochim*. *Biophys*. *Acta BBA - Gen*. *Subj*. **1830,** 4381–4390 (2013).

39. Ramuz, M., Hama, A., Rivnay, J., Leleux, P. & Owens, R. M. Monitoring of cell layer coverage and differentiation with the organic electrochemical transistor. *J Mater Chem B* **3,** 5971–5977 (2015).

40. Ramuz, M. *et al*. Optimization of a Planar All-Polymer Transistor for Characterization of Barrier Tissue. *ChemPhysChem* **16,** 1210–1216 (2015).

41. Curto, V. F. *et al*. Organic transistor platform with integrated microfluidics for in-line multi-parametric in vitro cell monitoring. *Microsyst*. *Nanoeng*. **3,** 17028 (2017).

Chapter 3: Effect of E cigarette emissions on tracheal cells monitored at the air-liquid interface using an organic electrochemical transistor

Publication Status: *This chapter has been submitted for publication in the peer-reviewed journal Advanced Biosystems in 2018* (M. P. Ferro*, L. Leclerc, M. Sleiman, B. Marchiori, J. Pourchez, R. M. Owens & M. Ramuz).

Collaborators: *Dr Lara Leclerc[1], Dr Mohamad Sleiman[2], Bastien Marchiori[3], Dr Jérémie Pourchez[1], Dr Roisin M. Owens[4,5]* and Dr Marc Ramuz[3]**
1Mines Saint-Étienne Department of Biomaterials and Inhaled Particles
2 Sigma Clermont Department of Photochemical
3Mines Saint-Étienne Department of Flexible Electronics
4Mines Saint-Étienne Department of Bioelectronics
5Cambridge University Department of Chemical Engineering and Biotechnology

3.1 Abstract

E-cigarette has been suggested as a potentially healthier alternative to cigarettes based on studies using cell viability, DNA damage and transcriptional response assays. However, little is known about the effect of e-cigarette aerosols on the integrity of tracheal epithelium, specifically with respect to barrier resistance. This is partly due to the lack of methods for monitoring epithelia at the air-liquid interface (ALI), i.e. under physiological conditions. Here, we show that an organic electrochemical transistor (OECT) can be adapted for the measurement of barrier resistance at the ALI. This technology enables accurate, continuous quantification of tracheal barrier integrity through the use of a conformable gate electrode placed on top of the cell-secreted mucus, obviating the need for addition of culture medium or buffer as a conductance medium for rigid electrodes. This platform allowed the detection of a dose-dependent, rapid decrease in barrier resistance of an *in vitro* model of human bronchial epithelium (MucilAirTM) after E-cigarette aerosols exposure. The system represents a powerful tool to study tissue responses of the human airway epithelium to inhaled smoke. The same technology will have broad applications for toxicology studies on other tissues with ALI, including other airway tissues and skin.

3.2 Introduction

Increases in tracheal epithelial barrier permeability constitute a well-known consequence of mucosal inflammation, and can be caused by several environmental exposures including air pollution components, respiratory viruses or bacteria, some chemicals, and cigarette smoke.[1] The introduction of REACH (Registration, Evaluation, Authorization and restriction of CHemicals) regulation, requiring toxicological profiling of all chemical substances imported into Europe, has further stimulated the development of physiologically representative *in vitro* cell models suitable for aerosol toxicity analysis.[2] The respiratory tract is lined by the airway epithelium, forming the interface between the internal milieu and the external environment. It represents the first physical barrier to prevent the entrance of harmful inhaled compounds or particles into the body and is thus an integral part of *in vitro* models used to study aerosol toxicity. This pseudostratified epithelium is formed by three categories of epithelial cells (shown in **Figure 3.1a**, left): goblet cells, that secrete an apical sticky viscoelastic mucus able to retain most of the potentially harmful inhaled particles, ciliated cells lined with hundreds of apical cilia, which orient the mucus clearance from the lung to the throat, and basal cells strongly anchored to the basal membrane by hemidesmosomes and tightly attached to the other two cell types by desmosomes. The latter provides mechanical stability to the tissue.[3] Apical junctional complexes localized between neighboring cells are essential for the barrier properties of the airway epithelia. They are composed of apically-located tight junctions (TJs), responsible for regulating paracellular transport of ions and molecules, along with underlying adherens junctions, important for initiation and maintenance of cell-cell adhesion.[4] A common feature of airway epithelium models is the development of an air-liquid interface (ALI) cell culture system to reproduce the physiological cells microenvironment.[5] Resulting physical and biochemical cues stimulate the secretion by goblet cells of a uniform mucus layer, which protects the underlining mucosa. ALI models usually exhibit highly polarized and pseudostratified epithelium with higher transepithelial electrical resistance (TEER) values and lower permeability compared to submerged cell culture systems.[6] Transwell inserts are commonly used as a support for ALI cell culture systems as they are cheap, easy to handle and allow access to both the basal and apical sides of the cell layer (**Figure 3.1a**, right).[7–9] A variety of available characterization techniques such as imaging, permeability and

Live/Dead assays are usually used to characterize ALI models *in vitro*. TEER measurement is a powerful and non-invasive technique to rapidly quantify barrier tissue integrity, traditionally performed using commercially available systems like Epithelial Voltohmmeter (EVOM; World Precision Instruments, Sarasota, FL) and cellZscope (nanoAnalytics GmbH, Germany).[10] In these instruments, Transwell inserts are placed in between two electrodes submerged into a conducting electrolyte (usually cell culture media) (**Figure 3.1b**, right). Electrodes are connected by an alternative current (AC) forcing the electrical flow to go through the epithelium. By recording the resulting current, the impedance spectrum is analyzed through an equivalent electrical circuit in which the barrier tissue is represented as a resistor (Rcell) and a capacitor (Ccell) in parallel (**Figure 3.1b**, left). These platforms are suitable for most submerged barrier tissue models but their use is severely limited in the case of ALI configurations, as they require the addition of cell culture media in the apical compartment for each measurement. Such "washing steps" may result in mucus dilution and artefactual experimental conditions. Previous studies pointed out the key role of mucus in protecting the underlying mucosa from harmful components and its absence may cause short-term damages.[6] In the case of aerosol toxicity assays, the interaction of the added liquid with deposited particles may change particle properties and/or concentration, compromising reproducibility.[5] As a consequence, performing TEER measurements of airway epithelium in ALI model using current technologies is problematic. To tackle this, we show here the development of an innovative platform to monitor barrier tissue resistance under physiological conditions, at the ALI. We combine the use of the Organic Electrochemical Transistor (OECT) with a novel conformal flexible gate (fg) electrode in a new fg-OECT system capable of conduction through the mucus layer, and thus avoiding addition of media to perform the measurements. Previous work by our group has demonstrated high temporal and spatial resolution monitoring of submerged barrier tissue resistance using OECT technology.[11,12] We show here the unique ability of the fg-OECT to monitor tracheal epithelium resistance at the ALI, specifically for assessing aerosol toxicity analysis (*i.e.* the toxicity of airborne particles in solid or liquid form suspended in a gaseous phase). We demonstrate the working principle of this new platform and illustrate how this approach can yield pertinent continuous electrical monitoring of the negative effects of e-

cigarette aerosols on an ALI model of human bronchial epithelium. These measurements are the first of their kind, thanks to the technology integration described herein.

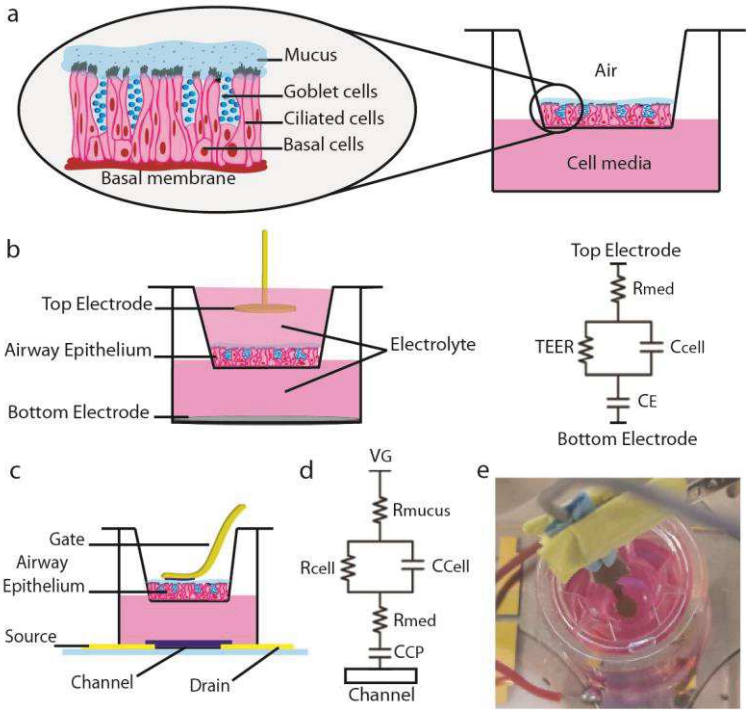

Figure 3.1: Electrical Resistance Monitoring Platform for ALI Airway Epithelium Model. ***a)*** *Air-liquid interface (ALI) cell culture configuration using Transwell inserts (right) allows tracheal cells to differentiate into a pseudostratified epithelium and to secrete a uniform mucus layer (left).* ***b)*** *Integration of an ALI airway epithelium model with the cellZscope module for electrical resistance measurement (left) and the corresponding equivalent electrical circuit (right) describing current flow between the top and the bottom electrodes. TEER and Ccell refer respectively to the transepithelial electrical resistance and the capacitance of the epithelium, Rmed refers to the resistance of the media and CE refers to the capacitance of the measurement electrodes.* ***c)*** *Integration of an ALI airway epithelium model into the fg-OECT platform for ALI resistance sensing. The flexible gate (fg) electrode is made of a polyurethane membrane coated with gold and PEDOT:PSS, which conforms to the cell-secreted mucus.* ***d)*** *fg-OECT equivalent circuit describing ionic transport between the gate electrode and the transistor channel. V_G refers to the voltage at the gate, Rcell and Ccell refer respectively to the airway epithelium resistance and capacitance, Rmed and Rmucus refer respectively to the resistance of the media and the mucus, Ccp refers to the capacitance between the conducting polymer and the electrolyte layer.*

3.3 Results

The integration of an ALI model of human bronchial epithelium into the fg-OECT platform (**Figure 3.1c)** consists of the following components: a channel made of the conducting polymer PEDOT:PSS spincoated in between two gold electrodes, source and drain, on a glass substrate, and a soft conformable gate electrode made of a polyurethane sheet coated with gold. Polyurethane membranes exhibit stretchable properties and biocompatibility making them good candidates to interact with biological tissue.[13] In our platform, the gate is placed directly in contact with the cell-secreted mucus. This new configuration explores the use of mucus as an electrolyte, obviating the need for addition of culture medium required by rigid electrodes. For polarizable electrodes, like gold, a double-layer capacitance is formed at the gate-electrolyte interface. To maintain efficient gating, the surface area of the gate needs to be at least ten times higher than the channel surface to allow efficient de-doping of the channel.[14] To avoid having a very large gate, we increased the capacitance of the gate by drop casting PEDOT:PSS on top of the gold, inducing a volumetric capacitance while maintaining its biocompatibility and mechanical properties.[15] For the fg-OECT platform the airway epithelium is represented by a resistor (Rcell) and capacitor (Ccell) in parallel (**Figure 3.1d)**, with an ALI airway epithelium on a Transwell integrated with a flexible gate **(Figure 3.1e**). The OECT is a well characterized volumetric ion to electron convertor.[16] and has already proven its value for monitoring barrier tissue integrity of a number of different epithelial types including intestinal epithelium[11] and lung tissue.[17,18] In this OECT, the channel and the gate electrode are connected through the presence of an electrolyte. Upon application of a positive gate voltage (V_G), ions from the electrolyte are pushed into the channel, decreasing the number of charge carriers in the polymer, resulting in a drop in the drain current (I_D). By placing a cell barrier between the gate and the channel, the tissue regulates ion diffusion through the tissue, decreasing the number of ions able to reach the channel, slowing down the drop in $I_{D.}$ The ability of the channel to reach a steady state following a gate bias pulse is directly dependent on the resistance of the tissue placed between. The higher the resistance of the epithelium, the slower the drain current reaches steady state. To illustrate the working principle of our platform with an *in vitro* model of human tracheal tissue we used commercially available, well characterized MucilAir^{TM} epithelium from several donors (MD051002, MD068501, MD072001). Measuring

the temporal response of the drain current of the fg-OECT to a 2s 0.2V pulse applied at the gate with and without MucilAir^{TM} epithelium (**Figure 3.2a)** we observed that the time constant of the OECT (extracted from a fit to an exponential growth of the temporal response)[19] changes from 0.0338± 0.0005s (in the absence of epithelium) to 0.228± 0.017s (in the presence of epithelium). By comparing the variation of the time constant in parallel with the TEER value obtained using a cellZscope module (after addition of media), for four healthy MucilAir^{TM} epithelia (MD051002), we noted good correlation between the two techniques **(Figure 3.2b)**. This also illustrates the variability in barrier tissue integrity from insert to insert, and the importance of dynamic, continuous monitoring to establish baseline and subsequent toxicological profiles.

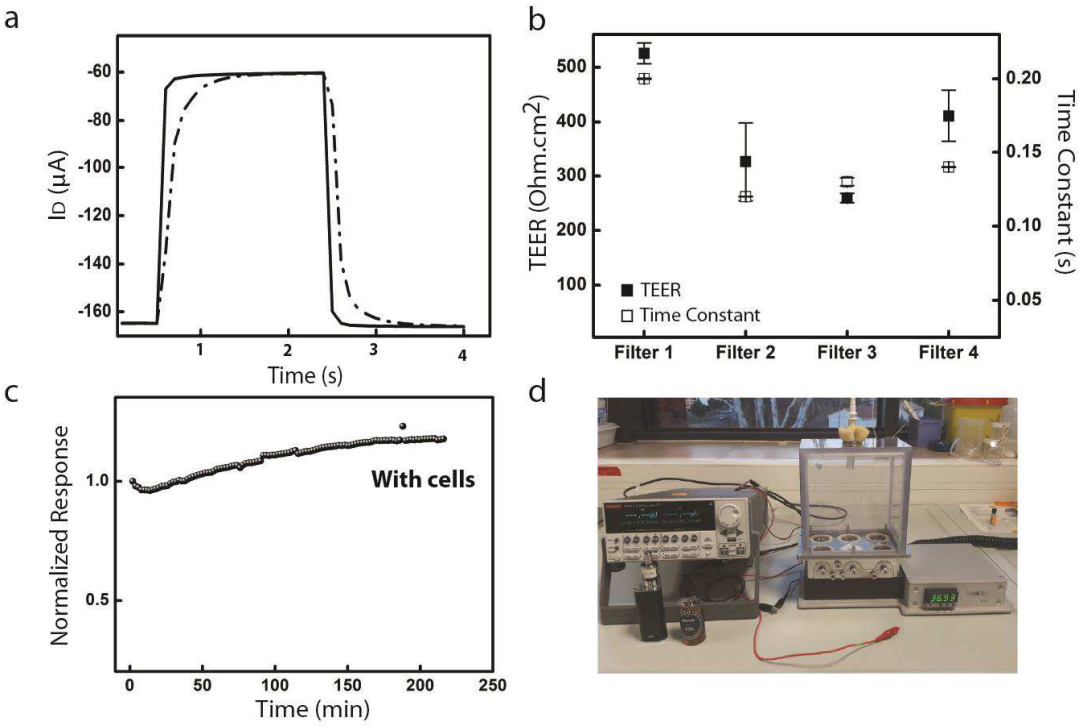

Figure 3.2: Fg-OECT device for continuous airway epithelium resistance monitoring. ***a)*** *Temporal response of the drain current of the fg-OECT to a 0.2V pulse applied at the gate during 2s after integration of a Transwell filter with (dashed line) or without (solid line) MucilAir^{TM} epithelium.* ***b)*** *TEER (solid black squares-left axis) obtained using a cellZscope module and time constant (empty squares-right axis) obtained using the fg-OECT device, of 4 different MucilAir^{TM} epithelium coming from the same donor (n=3 measurements). The time constant is extracted from a fit to an exponential growth of the fg-OECT temporal response. Error bars represent the standard deviation from the mean.* ***c)*** *Normalized time response of the fg-OECT with a MucilAir^{TM} epithelium without any aerosol*

deposition. The response is recorded every 2 min using a gate pulse of 0.2V for 2 sec. The present curve is used as a reference showing NR=1 corresponds to intact physical barrier properties. ***d)*** *Photograph of the fg-OECT platform and VITROCELL® Cloud6 module for aerosol exposure.*

The use of e-cigarettes is rapidly increasing but the effects on lung health are still largely unknown. Recent studies have shown pro-inflammatory responses in airway epithelium promoted by e-cigarette aerosols through a similar pathway known for cigarette smoke.[20,21] Cigarette smoke exposure has been proven to disrupt ALI epithelial barrier model integrity through a biphasic dose-dependent response over a couple of hours.[22,23] To demonstrate the application of the fg-OECT device as a sensor for ALI barrier tissue integrity, we evaluated the impact of short-term exposure of e-cigarette aerosols on airway epithelium barrier integrity using MucilAir^{TM} epithelial tissues. Taking advantage of the compatibility of our fg-OECT with measurements at the ALI, we performed continuous monitoring of the barrier resistance following aerosol exposure. To enable the fg-OECT to continuously monitor without damaging the barrier integrity over time, we integrated a MucilAir^{TM} epithelium into the platform and recorded the fg-OECT response time. The response time increases slightly over a period of 3.5 hours but then stabilized (**Figure 3.2c**).

Although it is clear that the fg-OECT brings clear benefits in avoiding dilution of the apical surface of cells through addition of media, standard evaluations of tissues at the ALI include analysis of ciliary beat frequency (CBF) as a further functional analysis of barrier tissue integrity. It has been reported that the submersion of airway epithelium in medium increases the variance of CBF compared to cells maintained at the ALI.[24] To evaluate the mechanical impact of the gate deposition on top of the bronchial epithelium, we conducted an analysis of (CBF) in MucilAir^{TM} epithelium with and without the fg-OECT. We measured CBF by extracting pixel intensities and applying Fourier transformation to bright field video recordings of the ciliated surface before and after being in contact with the gate for 10 and 200 min (ciliaFA software).[25] This analysis revealed that the fg-OECT induced a 3 fold increase in the variance of CBF compared to the cells maintained at the ALI (**Figure S3.1**). This variance is comparable to that induced by the addition of liquid on the apical side of the tissue[24].

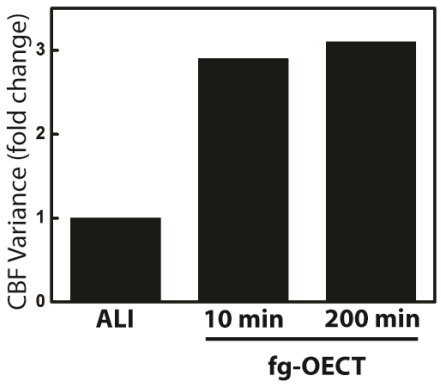

Figure S3.1: Fg-OECT-induced ciliary beating frequency variance. *Fold change in variance of ciliary beating frequency (CBF) of a MucilAirTM epithelium before (ALI) and after (fg-OECT) integration into the fg-OECT device during 10 min or 200 min. MucilAirTM epithelium came from a single donor (MD072001).*

To mimic exposure of the human airway epithelium to e-cigarette aerosols, we used a VITROCELL® Cloud6 module (VITROCELL Systems GmbH, Germany) composed of a heated base to maintain the environment at 37°C and a plastic bell allowing dose-controlled and spatially uniform deposition of e-aerosols on the Transwell (**Figure 3.2d**) Aerosols were collected directly from the e-cigarette mouthpiece using a plastic syringe and dispersed into the module through an apical aperture on the bell. We exposed MucilAir^{TM} epithelium to e-cigarette aerosols using a ROYKIN brand e-liquid containing 11 mg/mL nicotine and an intense but clinically relevant vaping regimen (**Table S3.2**). The introduction of aerosols to the tissue was confirmed using a quartz crystal microbalance (QCM) and revealed that each series of 5 puffs deposits 66.83±2.07 µg/cm^2 (**Figure S3.3**).

Table S3.2: Comparison of vaping parameters used in vitro versus human behavior.

Parameter	Human Behaviour	*In Vitro*
Number of puffs per minute	2-4	2.5
Puff volume	50 mL	50 mL
Puff duration	2-8 s	4 s
Interpuff interval	18-30 s	26 s

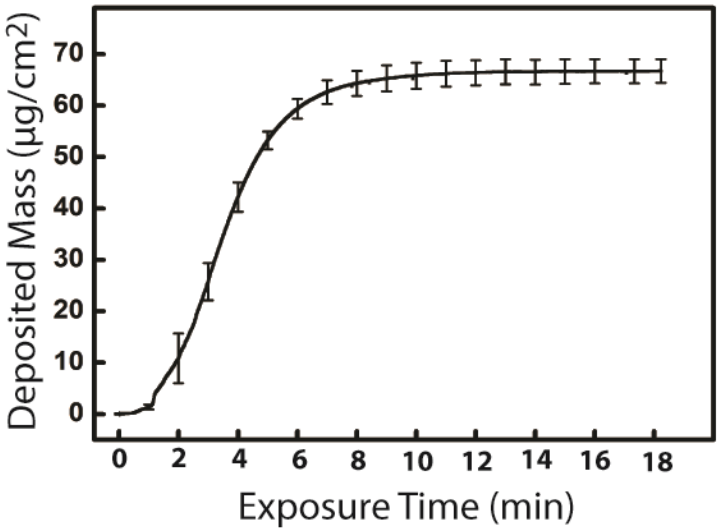

Figure S3.3: Kinetics of e-cigarette aerosol deposition. *Evaluation of aerosol deposition on MucilAirTM epithelium placed into a VITROCELL® Cloud 6 module using a quartz crystal microbalance system (n=4). 5 puffs of e-cigarette were generated and dispersed into the module during the first 2 min. Data shows mean values and error bars, which represent the standard deviation from the mean.*

The composition of volatile organic compounds (VOCs) in the e-cigarette aerosol was also characterized. This analysis showed the presence of high levels of propylene glycol (876 µg), vegetable glycerin (135 µg) and lower level of nicotine (6.7 µg) inside the VITROCELL® (**Table S3.4a**). Several carbonyls, including known cytotoxic aldehydes such as formaldehyde (8.9±3.4 µg) and acrolein (45±18 µg), were detected.[26] These aldehydes are likely generated by thermal decomposition of e-liquid solvents (e.g. propylene glycol and vegetable glycerin). Additional analyses of e-cigarette aerosol directly collected from the iStick allowed quantification of each compound per puff, revealing the presence of additional carbonyls (propanal and 2-butanone) as well as suggesting a potential loss of some lower volatile compounds (nicotine, propylene glycol and vegetable glycerin) likely by deposition and adsorption into the VITROCELL® surfaces (**Table S3.4b**).

Table S3.4: E-cigarette aerosols composition. ***a)*** *Levels of volatile carbonyls collected inside the VITROCELL® after the generation of 120 µg/cm2 aerosols using an iStick e-cigarette (ROYKIN liquid with nicotine at 11mg/mL) under the vaping regimen.* ***b)*** *Emission levels of carbonyls collected by directly introducing e-cigarette aerosol emitted by the iStick (ROYKIN brand e-liquid*

containing 11 mg/mL nicotine) into VOC sorbent tubes and DNPH cartridges, followed by chromatographic analysis. a For nicotine, propylene glycol and vegetable glycerin, levels were calculated based on only one measurement due to a technical problem (detector saturation) whereas duplicate measurements were made for the other compounds.

a

Compound	Amount (µg)
Propylene glycol	876 ± 325
Vegetable glycerin	135 ± 78
Nicotine	6.7 ± 3.0
Formaldehyde	8.86 ± 3.37
Acetaldehyde	105.57 ± 46.13
Acetone	18.06 ± 4.57
Acrolein	45.04 ± 17.62

b

Compound	Concentration (µg/puff)
Propylene glycol	1938a
Vegetable glycerin	410a
Nicotine	60.5a
Formaldehyde	5.7 ± 0.00
Acetaldehyde	3.4 ± 0.03
Acetone	2.0 ± 0.00
Acrolein	1.2 ± 0.01
Propanal	8.7 ± 0.02
2-butanone	5.3 ± 0.03

To evaluate the impact of e-cigarette aerosols on MucilAir™ epithelium barrier integrity, we first measured the TEER using the cellZscope. As described above, this platform necessitates the addition of media on the apical side of the

filter for each measurement point to submerge the upper electrode. To avoid dilution of the aerosols by adding and removing the media several times, TEER was measured only twice during the experiment: before and after aerosol exposition (**Figure 3.3a**). The TEER value of the filter alone without cells (Reference) was 7.85±0.51 Ω.cm^2 while the MucilAir^{TM} epithelium exhibited a resistance of 427.66±19.55 Ω.cm^2 in line with previous reports (**Figure 3.3b**).[27] We exposed the epithelia to a range of concentrations of aerosol: 133.66 µg/cm^2 (10 puffs), 267.32 µg/cm^2 (20 puffs) and 400.98 µg/cm^2 (30 puffs) of aerosols, revealing a dose-dependent impact of e-cigarette aerosols on MucilAir^{TM} epithelium (MD068501) (Figure 3b). The exposure to 267.32 µg/cm^2 did not induce a significant change in TEER while 133.66 µg/cm^2 resulted in a slight increase in the TEER value to 525.33±23.02 Ω.cm^2. Significant cytotoxicity was observed with 400.98 µg/cm^2, which induced a large drop in TEER value (85.3±1.1 %) with a final TEER value of 62.66±4.72 Ω.cm^2. Short-term cytotoxicity effect of e-cigarette aerosols on human airway epithelium model have already been shown, however, we are still missing continuous recording of barrier integrity overtime as up until now it has implied submerging the tissue and thus loss of the ALI.[21] This issue could be overcome by using the fg-OECT enabling continuous electrical measurement at the ALI. To more comprehensively validate our technology against commercially available systems, we decided to focus the experiment on two aerosol concentrations 334.15 µg/cm^2 (25 puffs) and 400.98 µg/cm^2 (30 puffs), expected based on cellZscope data, to disrupt barrier integrity within the first hours following exposure. An evaluation of the aerosol deposition kinetics has shown that 90% of the maximum mass of aerosols is deposited after only 6 min of incubation time (Figure S4). To ensure that we reached 99% of the deposited mass of aerosols before covering the epithelium with the gate, we designed our experiment by incubating the MucilAir^{TM} epithelium inside the VITROCELL® module, depositing the aerosol and then incubating for 15 min after the last puff was delivered before commencing measurement using the fg-OECT. We then performed continuous monitoring for a total of ~4 hours **(Figure 3.3c).** The normalized response of the fg-OECT in both conditions reveals a non-monotonic tissue response, ultimately leading to the complete loss of epithelial barrier properties (**Figure 3.3d**). The barrier disruption occurs within the first 3.5 hours following aerosol exposure and the cellular response is comparable for both

conditions, however the duration of each phase is dose-dependent. After exposure to 334.15 μg/cm^2 of aerosol the response time decreases rapidly, but a recovery phase occurs at ~ 50 minutes, followed by a second decrease phase occurring just before 150 minutes. Interestingly, after exposure to 400.98 μg/cm^2 of aerosol, we observed an increase in the device response of 121.5 ±9 % of the initial value, followed by a short recovery peaking ~100 minutes, followed by a sharp decrease. The reason for the recovery phase is unclear, however given the variety of compounds present in the aerosol (Table S5.1, Table S5.2) it is highly probable that a compound is present that exerts a stimulatory effect on the barrier properties, which is subsequently overcome by other compounds that are present in higher concentrations exerting toxic effects. An increase was also observed with the cellZscope for 133.66 μg/cm^2 aerosol addition (after 4 hours) suggesting that lower doses, or short exposure may stimulate initial increases in barrier tightness. The non-monotonic behavior was confirmed for two additional donors in response to 334.15 μg/cm^2 and 400.98 μg/cm^2 aerosol deposition on MucilAir^{TM} epithelium (MD068501;MD072001).

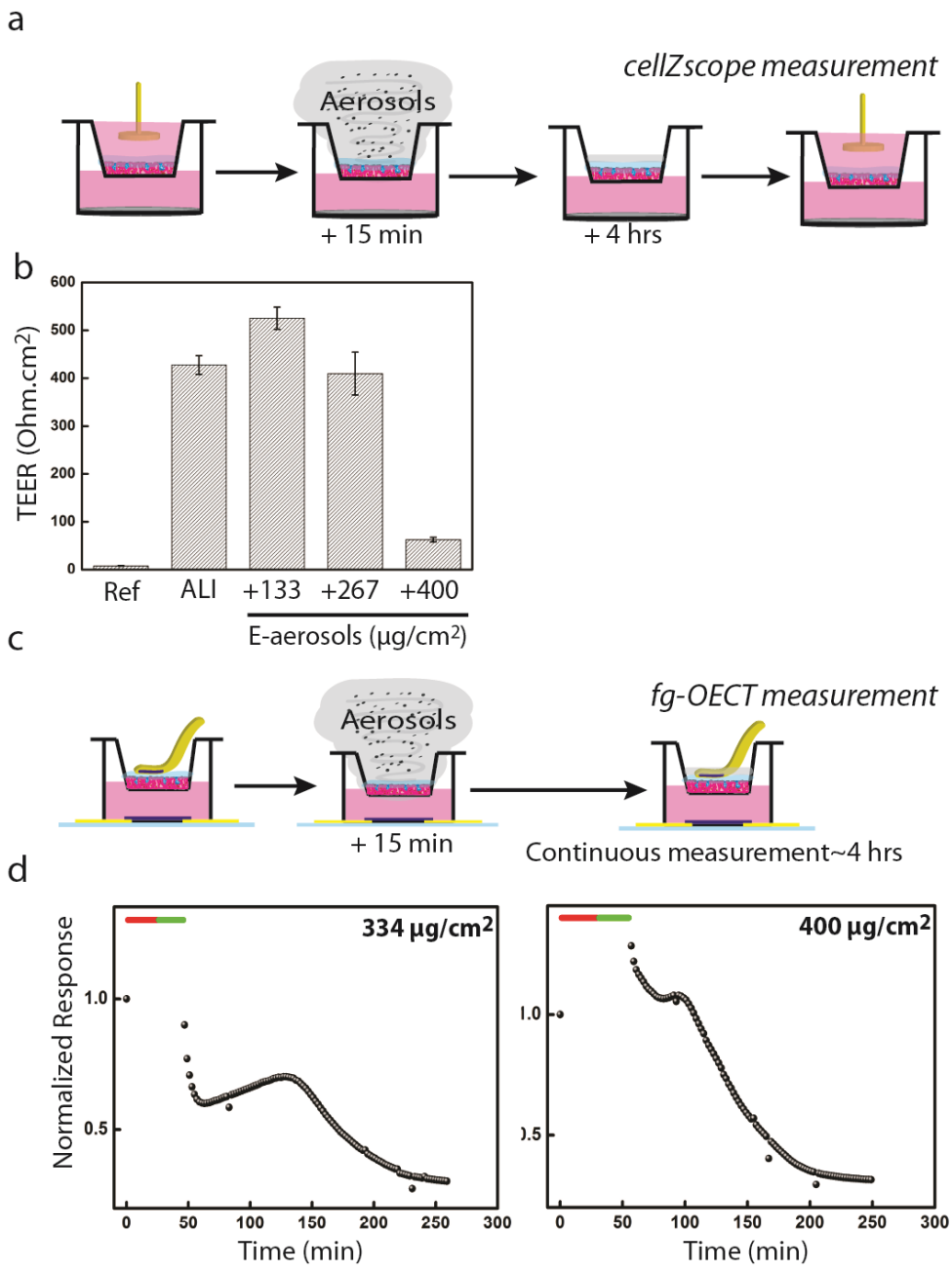

Figure 3.3: E-cigarette aerosol-induced cytotoxicity on MucilAir™ epithelium. ***a)*** *Schematic of the experimental setup to evaluate e-cigarette aerosol impact on MucilAir™ epithelium integrity using the cellZscope module. An initial data point was collected before aerosol deposition. Aerosols were then deposited on top of the cells for 15 minutes with a subsequent incubation time of 4 hours. Following the incubation time, a second data point was collected.* ***b)*** *Mean TEER value (n=2) obtained using a cellZscope module of the filter without cells (Ref), of MucilAir™ epithelium in the absence of aerosol exposure (ALI) or after being exposed for 4 hours to 133 µg/cm², 267 µg/cm² or 400 µg/cm² of e-cigarette aerosol. Error bars represent the standard deviation from the mean.* ***c)*** *Schematics of the experimental setup to evaluate e-cigarette aerosols impact on MucilAir™ epithelium integrity using the fg-OECT. Contrary to the setup*

described below, the epithelium was integrated into the fg-OECT device directly after deposition of aerosols to perform a continuous measurement during 4 hours. ***d****) Normalized time response of the fg-OECT device following integration of MucilAir™ epithelium exposed to 334 µg/cm² and 120 µg/cm² of aerosols. Aerosols were deposited on the cells at t=1 min for 25 to 30 min depending on the mass of deposited aerosols (red line) then cells were incubated for 15 min (green line) before the recording start. Here, NR=1 corresponds to initial intact barrier properties and NR=0.3 corresponds to a cell layer with no barrier properties.*

3.4 Discussion and Conclusion

In this work, we have developed a sensing platform to perform airway barrier tissue monitoring at the ALI. The fg-OECT system consists of a planar channel and a flexible gate electrode made of a polyurethane membrane that conforms to the apical side of the epithelial tissue. This technology takes advantage of the adhesive properties and ionic composition of mucus and uses it as an electrolyte for ionic diffusion. It provides a unique way to perform continuous monitoring of ALI barrier tissue resistance for hours while maintaining cells in a physiological environment. Using this system with a VITROCELL® Cloud6 module for airway epithelium aerosol exposure, we gained insight into how e-cigarette aerosols disrupt human bronchial epithelium barrier function over time. The use of e-cigarettes has rapidly become widespread, even if our understanding of e-cigarette impact on health is still very limited. Compared to conventional cigarettes, nicotine electronic delivery systems allow control of nicotine concentration used, and several studies promote its healthier impact on the lung tissue.[28–30] However, some papers have already addressed toxicity of e-liquids or e-cigarette aerosols on *in vitro* models of airway epithelium.[21,31,32] Due to the lack of adapted technology, these studies are mainly based on cellular inflammation response studies and viability testing but very few investigate aerosol impact on cell barrier integrity. We carried out a systematic analysis of the composition of e-cigarette aerosols generated from a ROYKIN brand e-liquid and performed continuous analysis of the effect of these aerosols on airway epithelium. We showed that the loss in barrier integrity is not monotonic, but rather first increases before finally decreasing, with the effect accelerated at higher doses. Recent studies have demonstrated cytotoxicity of short-term e-cigarette aerosols exposure, however, they have not shown such short

exposure time cytotoxicity (on the scale of hours).[21] There is currently no standardized method for e-cigarette aerosols application, and the time-deposited mass can vary a lot according to the aerosol module and associated parameters for vaporization, thus complicating the comparison of results with the literature. We took care to carry out a careful dosimetry assessment for e-cigarette studies to evaluate the real deposited mass of aerosols reaching the cell surface.[30] Our study suggests that e-cigarette should be viewed as far from risk free or harmless and non-neutral compared to air although possibly less toxic than cigarette smoke.[28,33–35] To more thoroughly investigate the cytotoxic effects of e-cigarette, a long term exposure model lasting several days to a few weeks, including recreation of physiological breathing movements during exposure would be more appropriate. One limitation of our system is the impact on variance in ciliary beating frequencies (CBFs) when the gate is continuously in contact with cells. However, this problem could be overcome by the inclusion of micro-holes through the gate in order to decrease the total surface of the gate in contact with cells while maintaining efficient gating. Additional studies should also include repeated exposure over multiple days to better evaluate the long-term effect of e-cigarette aerosols on airway epithelial function. In conclusion, the fg-OECT platform provides a unique, reliable and versatile approach to perform airway sensing into physiological conditions. Our strategy may be adapted to a variety of *in vitro* model configurations, including lung and skin models.[5,24,36]

3.5 Material & Method

Human airway epithelium cell culture

24-well plate MucilAir™ inserts from individual donors were purchased from Epithelix Sarl (Plan-Les-Ouates, Switzerland). MucilAir™ cultures were originated from primary human cells isolated from the human bronchial tissue. Three donors were used in the study. According to the supplier's certificate of analysis, donors for the cultures were 48-53 year old Caucasian, with no pathology reported (batch numbers: MD051002, MD068501, MD072001). Cells were maintained in culture using MucilAir™ culture media at 37°C and 5% CO_2 in a 95% humidified incubator for 24h before experiments. Every other day, media was changed using MucilAir™ culture media.

Device fabrication

Thermally evaporated gold source and drain contacts were defined by photolithography on top of a glass substrate. The planar channel of the Organic electrochemical transistor (OECT) was fabricated using the conducting polymer PEDOT: PSS (Heraeus, Clevios PH 1000) as the active layer. The PEDOT:PSS was mixed with ethylene glycol (Sigma Aldrich) in a volume ratio of 1:4 (ethylene glycol to PEDOT:PSS) to increase conductivity, the surfactant 4-dodecylbenzenesulfonic acid (DBSA, 0.5 µL.mL-1) to improve film formation, and the cross-linker 3-glycidoxypropyltrimethoxysilane (GOPS) (10 mg.mL-1) to improve film stability. Channel dimensions were patterned using a parylene peel-off technique described previously[19], resulting in a PEDOT:PSS channel length of 3 mm and width of 6 mm. A thermally evaporated gold gate electrode was defined on top of 50-µm-thick stretchable polyurethane (PU) film (DelStar technologies INC, ref EU50) by laser ablation, using LPKF Protolaser S equipment. A drop of 10 µl of PEDOT:PSS was added on top of the gold to reduce its impedance. Following PEDOT deposition, devices were baked for 1 h at 110°C under atmospheric conditions.

Aerosol exposure

A recent high-power electronic nicotine delivery system was used made up of a variable lithium-ion battery (iStick TC40W, Eleaf) and an atomizer (GS Tank, Eleaf). Equipped with an internal 2600 mAh battery, the variable wattage can be adjusted up to 40 W of vaping power. The variable wattage/voltage resistance range is 0.15–3.55 Ω, corresponding to the working range of the battery device. The GS-Tank is a recently engineered atomizer. It presents a resistance of 0.15 Ω, a liquid capacity of 3 mL and requires maximum push power ranging up to 40 W. The amount of airflow can easily be adjusted by the control ring on the atomizer base. Prior to performing particle size assessments, batteries were fully charged, the maximum air inflow position was fixed, and the value of the electrical resistance was checked. Atomizers were changed regularly to avoid biases due to the use of degraded and/or dirty coil. In our study, for all experiments the power level of the battery was fixed at 30 W. The E-liquid used was from ROYKIN brand (Tabac intense) corresponding to 80% of propylene glycol, 20% of vegetal glycerin and 11 mg/mL of nicotine. The aerosol generated by the high-power

ENDS was administered to the cell culture using a VITROCELL® Cloud 6 exposure system with 24-well insert adaptors. The system consists of a heating surface (37°C) where inserts can be placed under a hermetic exposure enclosure for the aerosol. Aerosol sampling was carried out considering 4-s puff of 55 mL every 30 seconds with 2 min pauses after each administration of 5 consecutive puffs to avoid ENDS overheating. Puffs were collected in a 60 mL syringe acting as a reservoir during the transfer to the Cloud 6 module. Experiments were performed with different numbers of puffs (10, 20, 25 and 30). A delay of 15 min at the end of the exposure allow ENDS aerosol to totally deposit on the cells before opening the enclosure.

Smoke deposition and composition analysis

To characterize the chemical composition of generated e-cigarette aerosols, gas phase samples were collected as follows: Direct sampling: e-cigarette aerosols were collected using a syringe with volumes varying between 5 mL and 55 mL, followed by direct injection of collected aerosol into Tenax sorbent tubes (Sigma Aldrich) to capture volatile organic compounds (VOC) or 2,4-dinitrophenylhydrazine (DNPH) Cartridges (Sigma Aldrich, LpDNPH S10L) to capture volatile aldehydes and ketones. Passive sampling in the VITROCELL® Cloud: to mimic exposure conditions, experiments in the VITROCELL® were carried out under identical conditions described above but by replacing the cells with the Tenax tubes and DNPH cartridges, for a duration of 80 minutes. Experiments were carried out in triplicate and blanks of the VITROCELL® (without e-cigarette aerosols) were also collected. After sampling, DNPH cartridges were extracted with 2 mL of acetonitrile followed by analysis using a Shimadzu liquid chromatography Nexera X2 equipped with a diode array detector SPD-M20A. A 10 µL aliquot was injected in a Nucleodur Sphinx RP, of 15 cm length and of 5 µm of particle size, at a flow rate of 1 mL min^{-1}. The detection wavelength was set at 360 nm and the mobile phase consisted of 60% ACN (acetonitrile) and 40% water. The identification of carbonyls was based on comparing retention times and UV spectra of peaks with those obtained with an analytical standard mix of 13 carbonyl-DNPH derivatives (Sigma Aldrich, ERA-028). A calibration curve was generated for quantification, by preparing in acetonitrile diluted solutions of the analytical mix, with concentrations in the

range (1-15 µg/mL). Three analyses were run per sample. On the other hand, trapped VOC inside the Tenax tubes were thermally desorbed at 270 °C at 50 mL min^{-1} for 5 minutes using an automated thermal desorption system (Turbomatrix ATD 150, Perkin Elmer), followed by analysis using gas chromatography (Agilent 6890) coupled to mass spectrometry (Agilent 5973). Separation of desorbed volatiles was carried out using a HP-5 MS column (30 m × 0.25 mm × 0.25µm) operated initially at 50°C for 1 min, followed by a 10 °C min^{-1} ramp to reach 300 °C. Mass spectra were scanned between m/z 35 and m/z 300 with the source temperature set at 230 °C. Identification was based on comparing retention times and mass spectra with those obtained by injecting authentic standards of nicotine, polypropylene glycol and glycerin (Sigma Aldrich) as well as by comparing mass spectra with the NIST 14 database. Quantification of nicotine was obtained by calibration in the range 10 – 100 µg.

Transepithelial electrical resistance measurements

Transepithelial electrical resistance (TEER) measurements were performed using the cellZscope module (nanoAnalytics GmbH, Germany). MucilAir™ insert (Corning Costar Transwell™ Permeable Supports with PET membrane inserts of 0.4 µm pore size) was integrated into the module and pre-heated cell culture media was added to the apical compartment of the insert prior to perform measurement at 37°C. After measurement performed, the liquid was gently removed from the luminal side of the insert paying attention to avoid removal of mucus and replaced into the incubator.

Electrical measurement and data analysis

For OECT measurements, the gate was gently placed at the center of the luminal side of the filter, in direct contact with cell-secreted mucus. OECT operations were performed using a Keithley 2612 Source Measure Unit. Pulse time response measurements were performed at 37°C before and after e-cigarette aerosols deposition outside the VITROCELL® Cloud module. Throughout these experiments, measurement parameters were chosen to avoid exposing the cell layers to a voltage drop above 0.4V, which could damage bilayer membranes[37]. Then, OECT data were collected using the following parameters: V_G = 0.2V, V_D = -0.2V on time 2s, off time= 118s. Measurement parameters were controlled using a customized LabVIEW program. When OECT data are shown in the form of a

normalized response (NR), NR is obtained by dividing time constant value (τ_t) by the time constant value before aerosol deposition (τ_0) and subsequently normalizing the dataset Fitting of the time constant (Tau) was performed using a Matlab script as already described.[38]

3.6 Acknowledgments

R. M. O would like to acknowledge Agence Nationale de la Recherche 3Bs project (M. P. F.) and Ecole des Mines Saint-Etienne/Institut Mines Télécom for Bourse Ecole (M. P. F.).

3.7 References

1. Rezaee, F. & Georas, S. N. Breaking Barriers. New Insights into Airway Epithelial Barrier Function in Health and Disease. Am. J. Respir. Cell Mol. Biol. 50, 857–869 (2014).

2. E. Commission, "REACH regulation," can be found under: http://ec.europa.eu/enterprise/sectors/chemicals/reach/index_en.htm, 2013.

3. Knight, D. A. & Holgate, S. T. The airway epithelium: Structural and functional properties in health and disease. Respirology 8, 432–446 (2003).

4. Buckley, A. G. et al. Visualisation of Multiple Tight Junctional Complexes in Human Airway Epithelial Cells. Biol. Proced. Online 20, (2018).

5. Upadhyay, S. & Palmberg, L. Air-Liquid Interface: Relevant In Vitro Models for Investigating Air Pollutant-Induced Pulmonary Toxicity. Toxicol. Sci. (2018). doi:10.1093/toxsci/kfy053

6. Lechanteur, A., das Neves, J. & Sarmento, B. The role of mucus in cell-based models used to screen mucosal drug delivery. Adv. Drug Deliv. Rev. 124, 50–63 (2018).

7. Huang, S. et al. Establishment and characterization of an in vitro human small airway model (SmallAirTM). Eur. J. Pharm. Biopharm. 118, 68–72 (2017).

8. Willoughby, J. A. Predicting Respiratory Toxicity Using a Human 3D Airway (EpiAirwayTM) Model Combined with Multiple Parametric Analysis. Appl. Vitro Toxicol. 1, 55–65 (2015).

9. Behrsing, H. P., Huang, S. & Constant, S. The Use of Human 3D Reconstructed Airway Cultures for Tobacco Product Evaluation: Precision Low-Volume Exposures at the Apical Site. Appl. Vitro Toxicol. 3, 56–67 (2017).

10. Srinivasan, B. et al. TEER measurement techniques for in vitro barrier model systems. J. Lab. Autom. 20, 107–126 (2015).

11. Jimison, L. H. et al. Measurement of Barrier Tissue Integrity with an Organic Electrochemical Transistor. Adv. Mater. 24, 5919–5923 (2012).

12. Ramuz, M., Hama, A., Rivnay, J., Leleux, P. & Owens, R. M. Monitoring of cell layer coverage and differentiation with the organic electrochemical transistor. J Mater Chem B 3, 5971–5977 (2015).

13. Pavlova, M. & Draganova, M. Biocompatible and biodegradable polyurethane polymers. 14, 6 (1993).

14. Cicoira, F. et al. Influence of Device Geometry on Sensor Characteristics of Planar Organic Electrochemical Transistors. Adv. Mater. 22, 1012–1016 (2010).

15. Proctor, C. M., Rivnay, J. & Malliaras, G. G. Understanding volumetric capacitance in conducting polymers. J. Polym. Sci. Part B Polym. Phys. 54, 1433–1436 (2016).

16. Rivnay, J. et al. High-performance transistors for bioelectronics through tuning of channel thickness. Sci. Adv. 1, e1400251–e1400251 (2015).

17. Yao, C. et al. Organic Electrochemical Transistor Array for Recording Transepithelial Ion Transport of Human Airway Epithelial Cells. Adv. Mater. 25, 6575–6580 (2013).

18. Romeo, A. et al. Drug-induced cellular death dynamics monitored by a highly sensitive organic electrochemical system. Biosens. Bioelectron. 68, 791–797 (2015).

19. Khodagholy, D. et al. Highly Conformable Conducting Polymer Electrodes for In Vivo Recordings. Adv. Mater. 23, H268–H272 (2011).

20. Wu, Q., Jiang, D., Minor, M. & Chu, H. W. Electronic Cigarette Liquid Increases Inflammation and Virus Infection in Primary Human Airway Epithelial Cells. PLoS ONE 9, e108342 (2014).

21. Yu, V. et al. Electronic cigarettes induce DNA strand breaks and cell death independently of nicotine in cell lines. Oral Oncol. 52, 58–65 (2016).

22. Neilson, L. et al. Development of an in vitro cytotoxicity model for aerosol exposure using 3D reconstructed human airway tissue; application for assessment of e-cigarette aerosol. Toxicol. In Vitro 29, 1952–1962 (2015).

23. Balharry, D., Sexton, K. & BéruBé, K. A. An in vitro approach to assess the toxicity of inhaled tobacco smoke components: Nicotine, cadmium, formaldehyde and urethane. Toxicology 244, 66–76 (2008).

24. Benam, K. H. et al. Matched-Comparative Modeling of Normal and Diseased Human Airway Responses Using a Microengineered Breathing Lung Chip. Cell Syst. 3, 456-466.e4 (2016).

25. Smith, C. M. et al. ciliaFA: a research tool for automated, high-throughput measurement of ciliary beat frequency using freely available software. Cilia 1, 14 (2012).

26. Dwivedi, A. M., Upadhyay, S., Johanson, G., Ernstgård, L. & Palmberg, L. Inflammatory effects of acrolein, crotonaldehyde and hexanal vapors on human primary bronchial epithelial cells cultured at air-liquid interface. Toxicol. In Vitro 46, 219–228 (2018).

27. Balogh Sivars, K. et al. A 3D Human Airway Model Enables Prediction of Respiratory Toxicity of Inhaled Drugs In Vitro. Toxicol. Sci. 162, 301–308 (2018).

28. Azzopardi, D. et al. Electronic cigarette aerosol induces significantly less cytotoxicity than tobacco smoke. Toxicol. Mech. Methods 26, 477–491 (2016).

29. Anthérieu, S. et al. Comparison of cellular and transcriptomic effects between electronic cigarette vapor and cigarette smoke in human bronchial epithelial cells. Toxicol. In Vitro (2017). doi:10.1016/j.tiv.2016.12.015

30. Haswell, L. E. et al. Reduced biological effect of e-cigarette aerosol compared to cigarette smoke evaluated in vitro using normalized nicotine dose and RNA-seq-based toxicogenomics. Sci. Rep. 7, (2017).

31. Sleiman, M. et al. Emissions from Electronic Cigarettes: Key Parameters Affecting the Release of Harmful Chemicals. Environ. Sci. Technol. 50, 9644–9651 (2016).

32. Sherwood, C. L. & Boitano, S. Airway epithelial cell exposure to distinct e-cigarette liquid flavorings reveals toxicity thresholds and activation of CFTR by the chocolate flavoring 2,5-dimethypyrazine. Respir. Res. 17, (2016).

33. Misra, M., Leverette, R., Cooper, B., Bennett, M. & Brown, S. Comparative In Vitro Toxicity Profile of Electronic and Tobacco Cigarettes, Smokeless Tobacco and Nicotine Replacement Therapy Products: E-Liquids, Extracts and Collected Aerosols. Int. J. Environ. Res. Public. Health 11, 11325–11347 (2014).

34. Cervellati, F. et al. Comparative effects between electronic and cigarette smoke in human keratinocytes and epithelial lung cells. Toxicol. In Vitro 28, 999–1005 (2014).

35. Dinakar, C. & O'Connor, G. T. The Health Effects of Electronic Cigarettes. N. Engl. J. Med. 375, 1372–1381 (2016).

36. Alexander, F., Eggert, S. & Wiest, J. Skin-on-a-Chip: Transepithelial Electrical Resistance and Extracellular Acidification Measurements through an Automated Air-Liquid Interface. Genes 9, 114 (2018).

37. DeFranco, J. A., Schmidt, B. S., Lipson, M. & Malliaras, G. G. Photolithographic patterning of organic electronic materials. Org. Electron. 7, 22–28 (2006).

38. Tria, S. A. et al. Dynamic Monitoring of Salmonella typhimurium Infection of Polarized Epithelia Using Organic Transistors. Adv. Healthc. Mater. 3, 1053–1060 (2014).

Chapter 4: A planar impedance sensor for 3D spheroids

Publication Status: *This chapter has been published in a peer-reviewed journal Lab on a Chip* (V. F. Curto*, M. P. Ferro*, F. Mariani, E. Scavetta &, R. M. Owens, Lab Chip, 2018, **18**, 933-943*)*. *These two authors contributed equally to this work.

Collaborators: *Dr Vincenzo F. Curto[1], Federica Mariani[2], Dr Erica Scavetta[2], Dr Roisin M. Owens[1,3]*
1Mines Saint-Étienne Department of Bioelectronics
2Universita di Bologna, Departimento di Chimica Industriale
3Cambridge University Department of Chemical Engineering and Biotechnology

4.1 Abstract

Three dimensional cell culture systems have witnessed rapid expansion in the fields of tissue engineering and drug testing owing to their inherent ability to mimic native tissue microenvironments. High throughput technologies have also facilitated rapid and reproducible generation of spheroids and subsequently their use as *in vitro* tissue models in drug screening platforms. However, drug screening technologies are in need of on-line monitoring platforms to study these 3D culture models. In this work we present a novel platform to measure the electrical impedance of 3D spheroids, through the use of a planar organic electrochemical transistor (OECT) and a circular-shaped microtrap. A new strategy was generated to overcome incompatibility of the integration of polydimethylsiloxane (PDMS) microdevices with OECTs fabrication. The impedance platform for 3D spheroids was tested by using spheroids formed from mono-cultures of fibroblast and epithelial cells, as well as co-culture of the two cell types. We validated the platform by showing its ability to measure the spheroid resistance (R_{sph}) of the 3D cell models and differences in R_{sph} were found to be related to the ion permeability of the spheroid. Additionally, we showed the potential use of the platform for the on-line R_{sph} monitoring when a co-culture spheroid was exposed to a porogenic agent affecting the integrity of the cell membrane.

4.2 Introduction

Recent advances in microfabrication, cell biology and tissue engineering have greatly supported the development of physiologically relevant 3D cell culture models. Through the use of these models it is now possible to create in vitro systems that can better mimic in vivo tissue dynamics with enhanced cell-cell and cell-extracellular matrix (ECM) interactions.[1,2] Generation of 3D cell models has been done using both natural and/or synthetic polymers for the fabrication of 3D porous scaffolds in which monoculture or co-cultures of cells can grow in 3D.[3] In parallel, the use of scaffold-free techniques for the formation of 3D cell constructs has also greatly advanced in recent years.[4] By taking advantage of the ability of cells to secrete their own ECM and to self-organize into stable 3D structures, cells cultured on non-adherent substrates form 3D microstructures commonly known as spheroids or organoids. Several reports have shown the development of different organoids types, such as cardiac[5,6], liver[7,8] and epithelial[9,10] tissues, both in mono and co-culture systems.

The rapid expansion of scaffold-free technologies to create 3D spheroids, such as the hanging drop technique[11], has opened up new opportunities in the field of drug discovery and toxicology screening. Recent efforts in this research area have made it feasible to use spheroids for high-throughput drug screening by employing well-established biology tools, such as imaging12 and other end-point assays.[13] Microfluidics have also been explored extensively for manipulation and testing of spheroids in lab-on-a-chip devices, both for long-term culture and drug screening.[14–17] Manipulation of spheroids in microfluidics can be performed by either loading the spheroid in the microfluidic after off-chip formation, or by direct formation of the spheroid in the microchannel. For the former, semi-oval shaped nozzle microfluidic devices are typically used to trap the spheroids in microfluidics. In these systems, bypass channels of higher hydraulic resistance are used to precisely position the spheroids in the microfluidics[14,15,18]. Silva et al. demonstrated a reduction in the shear-fluid damage of trapped pancreatic islets when using this device geometry.[15] For spheroids formed in situ, different strategies have been employed such as hemispherical microwells16 and pneumatic microstructure arrays[17] for tumor spheroid cultures, as well as the integration of microfluidic networks in hanging drop systems with a microfluidic gradient generator and capillary valves for on line toxicology studies of human colorectal

carcinoma spheroids.[19] Despite the push towards the use of spheroids for high-throughput drug discovery and toxicology, there is a definite gap in terms of available technologies capable of performing on-line monitoring of these 3D culture models. Label-free electrochemical impedance sensors (EIS) have proven to be a very powerful technique to assess the integrity of cell barriers in a minimally invasive manner[20]. To date, EIS has been used extensively with 2D cell culture for the determination of electrical resistance of cell layers (to assess cell properties such as adhesion, proliferation or differentiation[20]) in cells grown directly on electrodes, or on porous membranes, to determine a quantity known as trans(epi/endo)-thelial resistance (TEER).[21] However, there are few examples of impedance based methods for monitoring 3D cultures.[22–24]

Our laboratory has explored the use of a novel class of organic electronic devices, the organic electrochemical transistors (OECTs), as an alternative electronic transducer to perform cell-impedance sensing.[25] The OECT is a three terminal device that make use of the electrochemical doping/de-doping of a conducting polymer, such as poly(3,4-ethylene-dioxythiophene):poly(styrene sulfonic acid) (PEDOT:PSS), to modulate the drain current of the transistor channel.[26] OECTs have been employed in a wide range of applications, ranging from chemo/bio-sensing,[27,28] to in vivo brain activity recording[29] and in vitro measurements of electrogenic cells[30] as well as non-electrogenic cells[31,32]. Recently, we reported on the monitoring of 3D cysts using the OECT, however the sensitivity and the ease of use of the technique left room for improvement.[33]

In this work, we show the coupling of an OECT transducer with a microfluidic trapping device to realize an easy-to-use testing platform capable of assessing the resistance of spheroids. We propose a new fabrication strategy for both the OECT and the PDMS microtrap to achieve the optimal performance of our organic impedance sensor. Through the use of a PDMS circular-shaped microtrap we validated our platform using both mono- and co-culture spheroids, to demonstrate the ability of the platform to measure the spheroid resistance.

4.3 Results

4.3.1 Microtrap platform design

The OECT is a three terminal device that can be easily integrated and operated in microfluidics, as we showed previously.[32] **Figure 4.1a** shows a schematic representation of the proposed platform. The PDMS microtrapping device comprises a single straight channel (500 μm wide) that terminates with a nozzle in order to facilitate the positioning of the spheroid at its end. The spheroid is driven to the desired location by the liquid flow, as shown in the zoom-in schematic of Figure 1a (red arrow). A gravity-driven flow was achieved by altering the liquid level in the two liquid reservoirs connected to the two extreme of the monolithic PDMS microdevice, as shown in the fully assembled device in **Figure 4.1b**. During the spheroid trapping step the height of the liquid in the reservoir on the straight section (left) of the microchannel was kept to a higher level. The recovery of the spheroid was then performed by simply inverting the liquid levels of the two liquid reservoirs (green arrow of Figure 1a). In our platform, the OECT channel was positioned on the side of the straight microfluidic channel, while the gate electrode was placed on the right, after the nozzle microtrap.

Figure 4.1c shows a scheme of the OECT fabrication steps, including its integration with the PDMS microtrapping device, shown in step 6. Patterning of organic material, e.g. PEDOT:PSS, using the PaC peel-off techniques was first reported by DeFranco et al.34 and successively adapted by Sessolo et al. for the fabrication of low impedance multi-electrode arrays for in vitro neural recording.[35] In our laboratory, we have successfully used the PaC peel-off technique for the fabrication of several OECT channel geometries, from millimetre scale[36] down to tens of micrometre OECT channel length.[37] For standard OECT fabrication, we make use of two separate layers of PaC (~2μm each) to insulate the gold contacts and define the active area of the transistor by peel-off technique, respectively. PaC is one of the many derivatives of poly(p-xylylene) characterised by high mechanical and chemical stability. However, one of the main drawbacks in using PaC as the insulator layer for planar OECT is its chemical incompatibility with PDMS. In practice, PDMS and PaC cannot be bonded permanently together by simple O2 plasma activation, a common technique used to seal PDMS microfluidics onto glass substrates. To overcome this limitation, we modified the OECT fabrication protocol using only a single

layer of PaC. By doing so, we are able to pattern the PEDOT:PSS film to form an OECT and, at the same time, to use the glass substrate for bonding via O2 activation of the PDMS microtrapping device with our planar electronics.

In the new fabrication protocol, following lift-off to define gold tracks (step 1 Figure 1c), a single 2 μm thick layer of PaC was deposited via chemical vapour deposition (CVD) on top of an anti-adhesion layer (step 2). Patterning of the transistor active areas, both OECT channel and gate electrode, was achieved by O2 reactive-ion etching (RIE), step 3. To promote a stable covalent bonding between the gold and the conducting polymer film, a self-assembled monolayer (SAM) of the (3-mercaptopropyltrimethoxy)-silane was formed on the gold contacts. Covalent crosslinking between the mercapto-SAM and the spin-coated PEDOT:PSS film is possible due to the presence of a second silane agent (GOPS) dispersed in the PEDOT:PSS liquid suspension. A schematic of the chemical structures of the mercapto-SAM and its crosslinking network within the PEDOT:PSS film is shown in **Figure 4.1d**. The impact of the mercapto-SAM on the electrochemical behaviour of the OECT active layer was assessed by cyclic voltammetry and impedance spectroscopy, both confirming negligible effects (more details shown in ESI). Finally, the PaC layer was peeled-off to reveal the final pattern of the conducting polymer film, as shown in Figure 1c step 5.

It is important to note that initial attempts to fabricate fully operative and stable OECT devices without the use of the mercapto-SAM were unsuccessful. The mechanical stress generated at the PEDOT:PSS film/gold interface during mechanical removal of the single PaC layer resulted in delamination of the conducting polymer film and, in turn, failure in the transistor operation. Improvements in the OECT fabrication due the presence of the mercapto-SAM are presented in **Figure 4.1e**. **Figure 4.1f** shows the transfer characteristics of an OECT as a function of the gate bias, following mercapto-SAM functionalization. The drain current (ID)/voltage drain (VD) characteristic demonstrates a typical low voltage operation (below 1V) in depletion mode.[26]

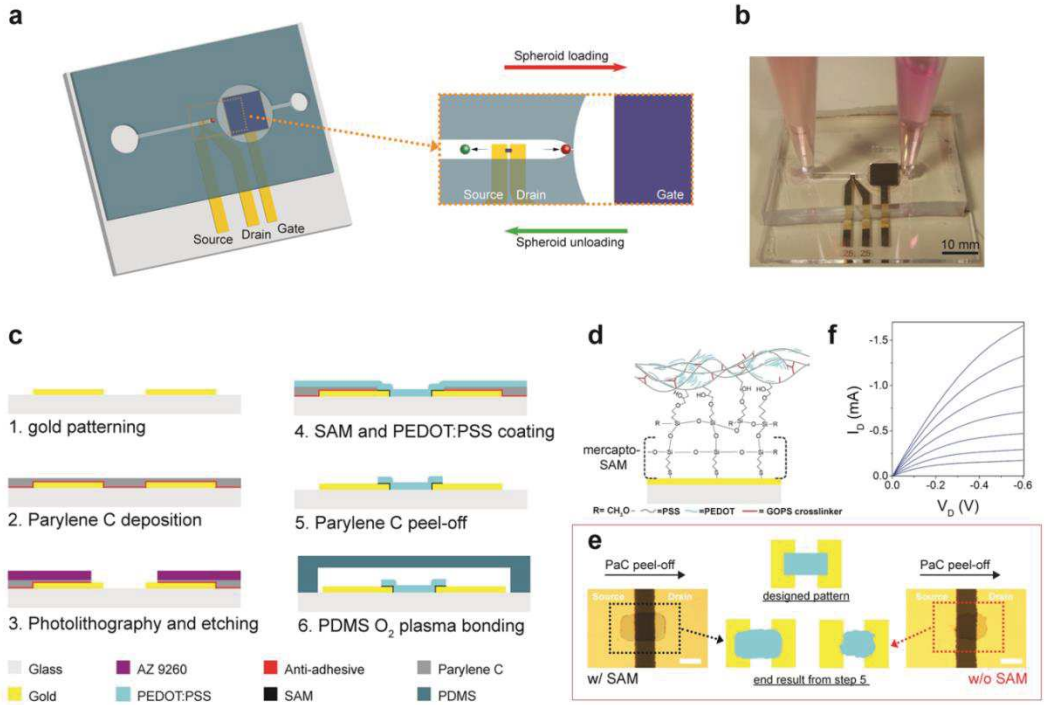

Figure 4.1. Microtrap platform design. ***a)*** *Schematic representation of the microtrap impedance sensing platform. An Organic Electrochemical Transistor (OECT) is fabricated on glass and the PDMS microtrapping device is positioned on top of the planar electronics. The transistor channel (25x25 µm²) is located to the left of the nozzle trap while the gate is positioned right after the microtrap. Zoom in illustration shows the loading (red) and unloading (green) flow direction to place the spheroid within the microtrap.* ***b)*** *Optical image of the fully assembled platform in which 1 mL micropipette tips are used as permanent reservoirs for the cell culture media and to control the gravity-driven flow.* ***c)*** *Modified version of standard OECT fabrication in order to achieve permanent bonding of the planar electronics and the PDMS microtrapping device. For fabrication of the platform, (1) patterning of gold tracks, (2) deposition of anti-adhesive layer and parylene C (PaC) layer, (3) reactive ion etching for PaC patterning and gold exposition, (4) mercapto-silane self-assembled monolayer (SAM) and spincoating of PEDOT:PSS conducting polymer dispersion, (5) PaC peel-off and (6) O_2 activation for bonding.* ***d)*** *Schematic illustration of the SAM-mediated covalent bonding between gold and PEDOT:PSS. The nucleophilic thiol groups selectively bond to gold, leaving the silanol moieties available to react with PEDOT:PSS crosslinker.* ***e)*** *Enhanced adhesion between gold and PEDOT:PSS film. In the presence of the mercapto-SAM, the PEDOT:PSS film stably adheres to the gold interface after peeling off the sacrificial PaC layer. In the absence of the mercapto-SAM, we observed PEDOT:PSS tearing away from the gold layer after Pac peel off. The middle schematics show the end results of the PEDOT:PSS patterning with and without SAM after PaC peel-off.* ***f)*** *Output characteristics (ID vs VD) of the OECT in the presence of the SAM on gold. VG varying from 0 (top curve) to +0.6V (bottom curve) with a step of +0.1V.*

Figure 4.2a shows time-lapse images of the spheroid trapping steps. As the spheroid can be easily trapped using our microtrap architecture, the next step was to achieve optimal performance of the impedance sensor when embedded in the microfluidics. One the main challenges to face when measuring the impedance of 3D spheroids is to drive the ion flux through the spheroid and to avoid any other low resistive ionic pathways, as they can lead to misinterpretation of the device readout. Standard photolithographic fabrication of master moulds for PDMS replica moulding makes use of a single layer of the negative SU-8 photoresist. However, when using SU-8 master moulds the resulting PDMS microfluidic chips can only be made with a squared cross-section profile due to the impossibility to reflow the photoresist after development. **Figure 4.2b-*i*** and ii show optical images of the PDMS microdevice and a schematic view of the cross section of the nozzle microtrap, respectively. Although this trap geometry has been shown by others to be effective for spheroid trapping,[14,15,18] the use of the squared profile microtrap leads to the presence of gaps in between the PDMS and the spheroid, highlighted by the black arrows in the scheme of Figure 4.2b-iii. This in turn can cause loss in sensitivity of the impedance sensor as the ionic current can flow through those gaps as they hold a lower ionic resistance compared to the paracellular ones. In support of this, Huerta et al. showed already the impossibility to measure impedance of cysts with a diameter smaller than the inner diameter (ID) of the glass micro capillary (Ø= 164 μm) used for the trapping.[33] As the envisioned platform should be able to reliably measure the impedance for spheroids of different radii, we modified the squared microtrap profile to achieve a circular-shaped nozzle profile that can be easily used with spheroids of different dimensions. An optical image of the PDMS modified microtrap and a close up picture of the circular-shaped profile (inset) is shown in **Figure 4.2c-*i***. Details on the post-modification of the microtrap using the glass capillary templating technique can be found in **Figure S1**. Schematics of the cross-sectional view of the circular-shaped profile of the trap and envisioned trapping of the spheroid are shown in **Figure 4.2c**. The use of this microtrap geometry can provide a better seal of the spheroid around the microtrap perimeter and greatly favour the operation of the impedance sensor by minimising the ionic flow around the spheroid. Moreover, another advantage of using the circular-shaped trap is the possibility to trap and measure impedance of any spheroid as long as their

diameter is larger than 80 μm, i.e. circular trap diameter. **Figure 4.2d** shows a TIF-pLifeAct spheroid of a diameter equal to ~149 μm trapped in the circular-shaped nozzle where a tight contact between the spheroid and the PDMS is clearly visible, as indicated by the white arrow.

Alongside the improvements of the trapping microstructure, it was also important to assess the impact of the microtrap on the performance of the OECT in its operational frequency range (1 Hz ≤ f ≤ 20 kHz). In fact, by placing the nozzle in between the gate and the channel of the transistor a change in the transistor response is expected due to an increased electrolyte ionic resistance (Rel). **Figure 4.2e** shows a direct comparison of the bandwidth spectra (transconductance gm vs frequency) for the OECT in the absence and presence of the microtrap. The transconductance gm represents the gain (amplification) of the transistor (ΔID/ΔVG). Figure 2e shows the frequency dependent characteristic of the OECT when both the transistor gate and channel were placed in the straight microfluidic channel, right before the nozzle microtrap. A characteristic plateau of gm is observed up to ~700 Hz, followed by an abrupt decrease in the transconductance at higher frequencies and a resulting cut-off frequency (-3dB) at ~1.47 kHz. The inset image of Figure 2e shows an equivalent circuit for which the capacitor is the OECT capacitance (COECT) and Rs is the series resistance, including the electrolyte resistance Rel. In the presence of the squared and circular-shaped microtrap, a slightly different gm vs frequency characteristic was measured, with a shift of the cut-off frequency towards lower frequencies due to the increase in the Rel contribution in both cases. We measured a cut-off frequency of ~190 Hz (red) for the squared and unmodified microtrap, and ~63 Hz (blue) when using the circular-shaped microtrap. For the latter, the lower cut-off frequency is consistent with the fact that the circular-shaped microtrap has a smaller cross-sectional area (higher Rel) compared to the squared one, as shown in the inset equivalent circuit of Figure 2e.

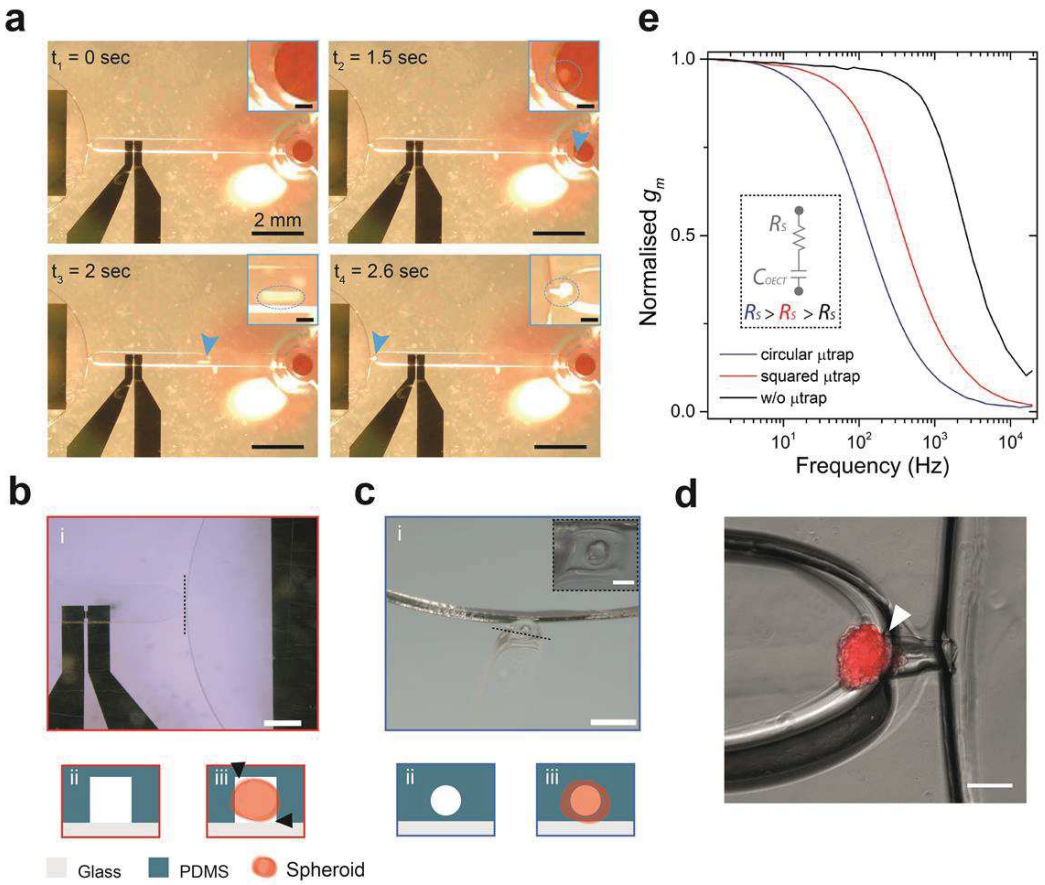

Figure 4.2. Spheroid impedance sensing ***a)*** *Time lapse images of the spheroid trapping. From top left to bottom right, (t_1) placing the spheroid in the inlet reservoir, (t_2) spheroid reaching the PDMS inlet, (t_3) spheroid travelling through the microchannel and (t_4) spheroid trapped in the microfluidic nozzle.* ***b)*** *top - Optical image of the microtrap for the fully assembled platform (scale bar 500 µm). bottom -Schematics of the cross-sectional view of the squared microtrap and spheroid trapping. The squared profile can lead to the presence of gaps between the spheroid and the PDMS (black arrows).* ***c)*** *top – Optical image of the modified version of the microtrap using the glass capillary templating technique. Inset image showing a close up view of the circular-shaped microtrap (scale bar 500 µm, inset 100 µm). bottom - Schematics of the cross-sectional view of the circular-shaped microtrap and spheroid trapping.* ***d)*** *Optical image of a TIF pLifeAct spheroid trapped in the circular-shaped trap. The white arrow shows the conformal contact between the spheroid and the PDMS (scale bar 100 µm).* ***e)*** *Frequency dependent response of the OECT in microfluidics in the absence of the microtrap (black), when using the squared microtrap (red) and the circular-shaped microtrap (blue). The decrease in the cut-off frequency (-3dB) is due to the increase of the series resistance in the electrolyte.*

4.3.2 Microtrap platform performance

The main objective of this work was to realise a platform capable of measuring the electrical resistance of spheroids (R_{sph}) in a simple and reliable manner. To validate our platform, we first made use of fluorescently labelled TIF (pLifeAct expressing RFP actin) spheroids. Spheroids were cultured using two different conditions in order to achieve spheroids of different dimensions. Using a static hanging drop plate, we were able to grow these spheroids with an average diameter of 152±4 μm and 187±11 μm by seeding 1000 and 2000 cells per drop, respectively. **Figure 4.3a** shows the typical bandwidth spectra for the transistor when a single TIF pLifeAct spheroid was placed inside the microtrap. When using the OECT to measure the spheroid impedance, a further decrease in the initial cut-off frequency of the transistor was monitored due to changes in the ion flux caused by the presence of the spheroid in the microtrap, from the blue curve to the orange and green curves. **Figure 4.3b** shows optical images for the two spheroids with a diameter of ~140 μm for the 1000 cells and a diameter of ~184 μm for the 2000 cells when trapped in the circular-shaped nozzle. The two insets of Figure 4.3b show the fluorescence images of the spheroids prior to trapping, showing almost unaltered shape of the spheroids once inside the microtrap. We can also observe how the two spheroids present a good contact to the circular-shaped trap despite their different diameters.

With regards to the transistor cut-off frequency change given by the two TIF spheroids, we observed in this case only a slight difference in the final cut-off frequencies, i.e. ~2Hz. **Figure 4.3c** shows the extracted impedance spectra measured in the absence of spheroids (blue curve), and when the two spheroids were placed in the microtrap (1000 cells, green curve; 2000 cells, orange curve). The inset equivalent circuit of Fig.3c was used to fit the impedance spectra in order to extract the spheroid resistance values R_{sph} for the two TIF spheroids. It should be noted here that R_{sph} takes into account the ionic resistive pathways both through and around the spheroid. Although the circular-shaped trap is able to significantly improve the seal between the PDMS microtrap and the spheroid, the presence of gaps contributing to the final impedance cannot be excluded. The estimated R_{sph} for the ~140 μm spheroid is 3.6 Ω·cm2 and for the ~184 μm spheroid the R_{sph} is equal to 4.1 Ω·cm2. The slightly larger R_{sph} of the latter spheroid might be attributed to its larger dimension as this spheroid can impede

more the ion flow when compared to the smaller one. However, when comparing the mean R_{sph} values for several spheroids **in Figure 4.3d** (1000 cells R_{sph}=3.9 Ω·cm2 (n=4), 2000 cells R_{sph}=4.4 Ω·cm2 (n=4)), there is not a statistically significant difference ($p < 0.05$, t-test). TIF cells' primary role is structural, being largely present in connective tissue rather than epithelial or endothelial (barrier-tissue). Therefore, this result showed us the R_{sph} is largely dependent on the ion permeability of the spheroid, i.e. cell type and function, rather than its dimensions.

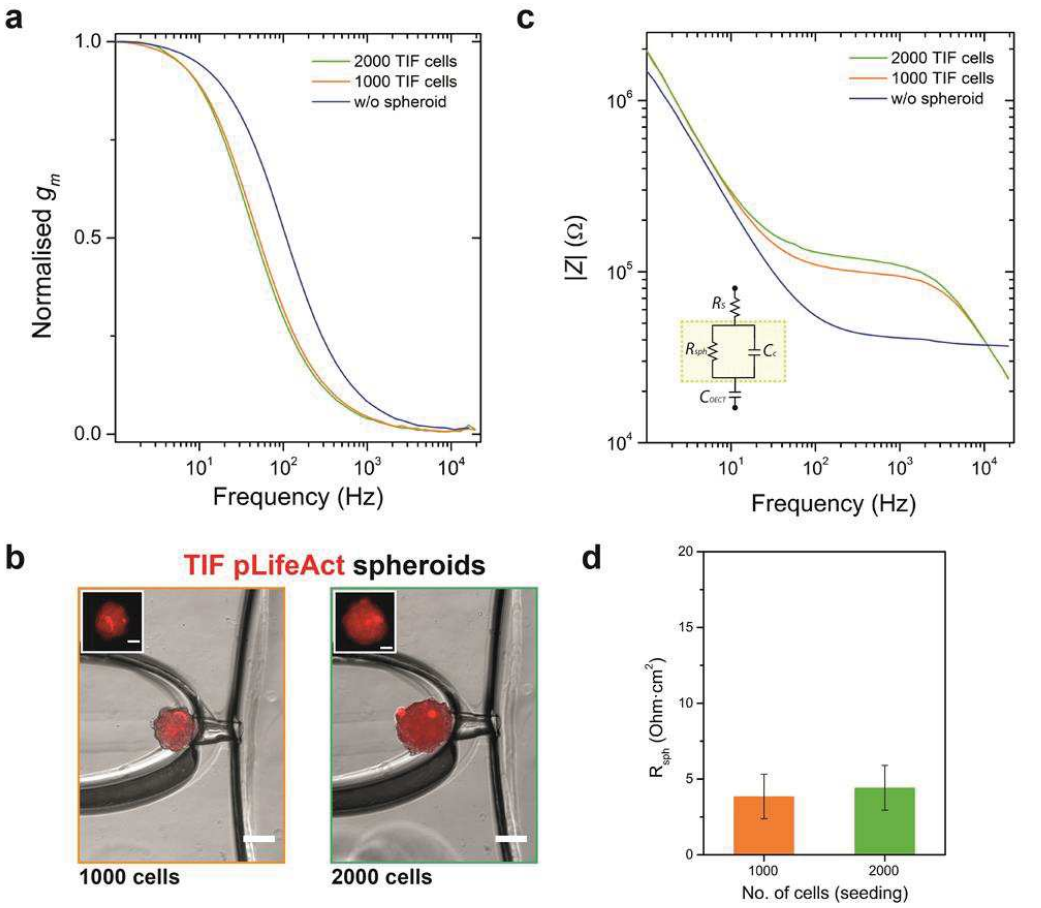

Figure 4.3. Size-selective microtrap platform performance. ***a)*** *Typical frequency dependent response of the OECT in the absence (blue) and in the presence of TIF pLifeACT spheroids of different dimensions. Seeding conditions for the spheroid: 1000 cells per drop (orange) and 2000 cells per drop (green).* ***b)*** *left – 1000 cells spheroid (Ø=ca. 140 µm) trapped inside the circular-shaped nozzle. Inset image shows the spheroid prior trapping (scale bar 100 µm, inset 50 µm). right - 2000 cells spheroid (Ø=ca. 184 µm) trapped inside the circular-shaped nozzle. Inset image shows the spheroid prior to trapping (scale bar 100 µm, inset 50 µm).* ***c)*** *Typical impedance spectra in the absence (blue) and presence of TIF pLifeAct spheroids (1000 cells, orange; 2000 cells, green). Inset equivalent circuit used for the fitting of the spheroid resistance (R_{sph}).* ***d)*** *R_{sph}*

obtained for different TIF pLifeAct spheroids cultured using the two conditions. (1000 cells n=4, 2000 cells n=4).

Following this result, we then wanted to investigate the ability of the platform to measure the R_{sph} when different cell types are used for the formation of the spheroids. MDCK II cells are epithelial cells from the distal part of the kidney tubule that express TJs in their apical cellular membrane and are highly resistive when cultured in 2D.[32] Initial attempts to grow MDCK II spheroids using the hanging drop technique were not successful as we could only form cellular clusters with dimensions well below the circular-shaped trap diameter, i.e. 80 μm. Yonemura et al.[9] observed a similar behavior when growing MDCK II cells in U-bottomed culture plates. As a means to improve spheroid formation, we made use of dextran (see materials and methods) added to the cell culture media in order to increase the media viscosity and favour spheroid formation. By doing so, we were able to form much larger MDCKII organoids, although we could not achieve high yield. An optical image of the trapped MDCK II eGFP organoid is presented in **Figure 4.4b**. The inset of Figure 4b shows the organoid prior to trapping in the circular-shaped nozzle. In this case, we noticed that the MDCK II eGFP organoids had a much softer nature compared to the TIF spheroids as the trapping always resulted in the spheroid being drawn into the length of the circular trap. Changes in the relative height of the liquid in the inlet/outlet reservoirs to achieve lower flow rates were not sufficient to avoid the confinement of the organoid throughout the trap. The softer nature of the MDCK II eGFP cluster may be due to the formation of lumen, resulting in formation of a cyst rather than a spheroid, previously described under the culturing conditions used here.[9] When measuring the impedance of the R_{sph} for the MDCK II-eGFP cyst, we observed a drastic decrease in the transistor cut-off frequency (below 5 Hz) as shown by the light grey curve in **Figure 4.4a**. Resulting impedance spectra and mean R_{sph} values of 145±11 Ω·cm2 (n=2) for the MDCK II-eGFP cyst are shown in **Figure 4.4d and e**, respectively. With regards to the much higher R_{sph}, we believe this may be caused by the typical lower ion permeability of this type of cells as well as the much tighter contact among the cells due to the cyst deformation/compression inside the circular-shaped nozzle. This result demonstrates that the platform can easily detect difference in the spheroid ion permeability; however, we needed

further evidence of this due to the unexpected insertion of MDCK II eGFP cyst inside the microtrap.

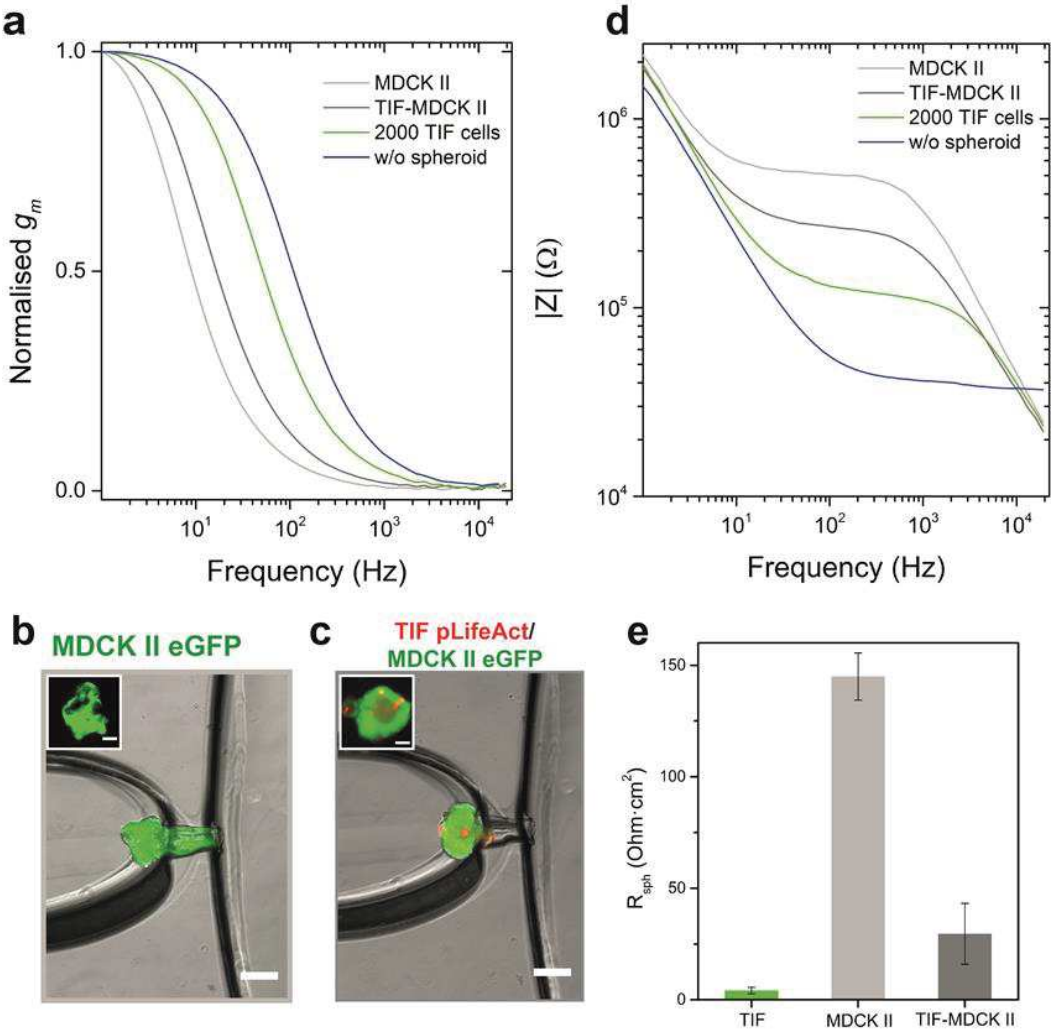

Figure 4.4. Barrier-selective microtrap performance. ***a)*** *Typical frequency dependent response of the OECT in the absence (blue) and in the presence of TIF pLifeACT spheroid (green), TIF pLifeAct/MDCK II eGFP co-cultured spheroid (grey) and MDCK II eGFP spheroid (light grey).* ***b)*** *MDCK II eGFP spheroid (Ø=ca. 145 µm) trapped inside the circular-shaped nozzle. Due to the presence of a cyst lumen, the cyst presents a soft nature that results in the insertion of the spheroid inside the circular-shaped trap. Inset image shows the spheroid prior trapping (scale bar 100 µm, inset 50 µm).* ***c)*** *TIF pLifeAct/MDCK II eGFP co-cultured spheroid (Ø=ca. 183 µm) trapped inside the circular-shaped nozzle. Inset image shows the spheroid prior trapping (scale bar 100 µm, insert 50 µm).* ***d)*** *Typical impedance spectra in the absence (blue) and in the presence of TIF pLifeACT spheroid (green), TIF pLifeAct/MDCK II eGFP co-cultured spheroid (grey) and MDCK II eGFP spheroid (light grey). (e) Mean R_{sph} obtained for different spheroid types: TIF pLifeAct (2000 cells n=4), MDCK II eGFP (n=2) and TIF pLifeAct/MDCK II eGFP (n=5).*

We had shown before that TIF pLifeAct spheroids were not deformed (Figure 3) when trapped in the platform. Given their supporting tissue function, we wanted to use them in combination with MDCK II cells for the formation of a more mechanically stable spheroid. In this case, the TIF cells should provide a suitable matrix on which the MDCK II can grow and form a continuous cell barrier. Interestingly, the co-culture of the two cell types resulted in the formation of spheroids with a core-shell structure in which the core is made of TIF cells while the MDCK II cells form a confluent layer around the core. The insert image of Figure 4b shows a typical TIF/MDCK II spheroid where it is possible to observe a more dense core of TIF cells (red) surrounded by the MDCK II (green) epithelial cells. Figure 4b shows a trapped TIF/MDCK II spheroid that did not deform after trapping, similar to what we observed previously when only using TIF cells for the spheroid. When measuring the R_{sph} for the TIF/MDCK II spheroid, we obtained typical resistance values higher than the TIF spheroid but lower than the MDCK II ones. Co-cultured spheroids were characterised by a cut-off frequency of ~10 Hz, as shown in Figure 4a. Figure 4e reports values of R_{sph} equal to 29.3±13.7 Ω·cm2 (n=5) for an average spheroid dimension of 206±66 μm. In the same graph resistance value of TIF spheroids (2000 cells) are also reported, for a more straightforward graphical comparison of the differences in R_{sph} of the three spheroid types. Overall, these results provide clear evidence of how the measured R_{sp}h is influenced by the differences in the spheroid ion permeability given by the cells and, that the combination of the OECT with the circular-shaped microtrap is a suitable platform to assess such differences.

To further validate the platform, we also tested the dynamic performance of the device. **Figure 4.5** shows dynamic measurements over a period of 45 minutes during which the TIF/MDCK II spheroid is exposed to a porogenic molecule, Triton X-100, a well-known non-ionic surfactant. The positive control experiment shows that the transistor performance was not affected by the presence of the Triton X-100 in the electrolyte. The variation of the R_{sph} (circle black) for a co-culture of TIF/MDCK II spheroid exposed to a concentration equal to 170 μM of Triton X-100 shows that it takes *ca*. 10 minutes to observe an initial decrease in the R_{sph}. Following this time, a more marked variation of the R_{sph} was then recorded with a total loss of ~90% of the initial resistance after *ca*. 35 minutes of

exposure to Triton X-100. The control experiment in the absence of Triton X-100 in Figure 5 (circle grey) does not show a similar trend and the R_{sph} is stable over the same period of time. However, some variations in the R_{sph} were measured probably due to movements of the spheroid within the trap during the testing period.

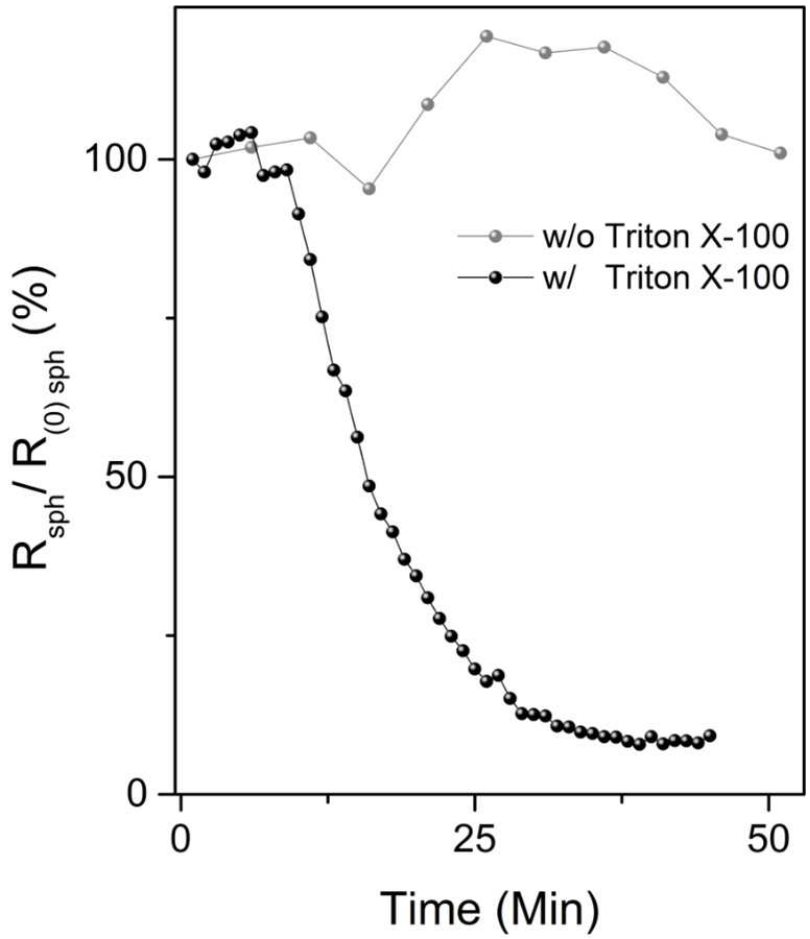

Figure 4.5. Dynamic performance of the microtrap platform. *On line measurements of the R_{sph} in the presence (black/white dots) and absence (grey/white dots) of a porogenic agent, Triton X-100, 170 µM. Due to the presence of Triton X-100 in cell culture media, a continuous decrease in R_{sph} was measured resulting from the gradual disruption of the spheroid cells membrane integrity.*

4.4 Discussion

In this work we have developed a novel platform to perform impedance sensing of 3D spheroids. The platform comprises a circular-shaped PDMS microfluidic trapping device and an OECT impedance sensor to measure the R_{sph}.

The proposed platform is capable of measuring the impedance of different kinds of spheroids. When using TIF spheroids we obtained R_{sph} values of just a few $\Omega \cdot cm^2$. The low resistance seems to be in agreement with the fact that fibroblast cells have a supporting tissue function and do not present significant paracellular resistance. When varying the spheroid diameter we observed negligible differences in the R_{sph} of TIF spheroids, understood as a change in the ionic pathways when flowing through a larger or smaller spheroid. We showed the suitability of this platform for measuring R_{sph} for spheroids that present different ionic permeability as they were grown using different cell types. For TIF/MDCK II spheroids we obtained average R_{sph} values ~6.7 times larger than for TIF pLifeAct. Although these two spheroids types present comparable dimensions (TIF/MDCK II spheroid diameter equal to 206±66 μm and TIF pLifeAct spheroids (2000 cells) average diameter equal to 187±11 μm) a marked difference in the R_{sph} was measured due to the presence of highly resistive MDCK II epithelial cells on the spheroid outer shell.

When looking at other 3D spheroid impedance platforms, e.g. making use of microcavities[22], hanging drop systems[23,24], capillary traps[38] and others[39], one of their current limitations is the absence of a common physical quantity to describe the spheroid impedance. Different parameters/units had been used when studying the spheroid impedance, for example by comparing changes of the impedance magnitude at multiple frequencies[24], normalised current[23] and relative increase of the full impedance frequency spectrum[22,38,39]. Although these methods are suitable to describe the 3D *in vitro* models under investigation, it is difficult to have a straightforward comparison between the outcomes of these studies. For impedance sensors in 2D cell cultures, TEER is the gold-standard parameter employed by most of the commercially available impedance systems, such as cellZscope, chopstick electrodes and ECIS from Applied BioPhysics. However, the TEER describes the trans(endo/epi)thelial resistance of a single cell monolayer while in spheroids the cells are clustered together in a 3D configuration. Thus, TEER is not a suitable parameter to be used when studying the impedance of 3D spheroids. As an alternative, in this work we made use of the R_{sph} as the physical quantity of interest to describe the impedance of spheroids expressed in $\Omega \cdot cm^2$ units. Indeed, we were able to show a correlation between spheroid resistance R_{sph}

and differences in the spheroid ionic permeability arising from the use of different cell, as well as online assessment of the R_{sph} in the presence of a porogenic agent. To conclude, it should be stressed here once more that R_{sph} should solely describe the ionic paracellular resistance in 3D, however, we cannot exclude the presence of ionic pathways around the spheroids. Our strategy here was to use the circular-shaped nozzle to improve the seal contact between spheroid and PDMS trap and minimise/avoid the presence of gaps that can lead to potential low resistive ion fluxes around the spheroid. Further studies on this aspect are currently underway.

4.5 Conclusion

In this work, we have proposed a novel platform combining a circular-shaped microtrap and OECTs to accurately measure the impedance of 3D spheroids. A new photolithographic fabrication protocol was developed for the fabrication of the OECTs through the use of a mercapto-silane agent to improve the adhesion between PEDOT:PSS/gold and we showed standard OECT performance. Moreover, the new fabrication protocol favoured the integration of PDMS based microfluidics, otherwise impossible when using the 2-layers PaC fabrication due to the chemical incompatibility for bonding between PaC and PDMS.[35] The spheroid microfluidic trap consisted of a single channel terminating with a nozzle trap geometry. To improve the spheroid ionic blockage between the channel and the gate of the OECT, the nozzle trap was modified to achieve a circular-shaped profile that minimises/avoids the presence of gaps between spheroid and PDMS trap contours. The modified trap was used to measure the impedance of spheroids in a non-destructive way. When using the platform to measure the impedance of 3D spheroids, we showed marked differences in the R_{sph} for spheroids grown using fibroblast and epithelial cells alone, and when combining the two cell types. Finally, we assessed the platform performance while measuring in real-time changes in the R_{sph} caused by the presence of a triton X-100 in the cell media, known to disrupt cell membrane integrity. Future work will focus on making improvements to the spheroid trapping mechanism to avoid unwanted insertion of the spheroid inside the circular-shaped trap when using softer spheroids and/or cysts, such as the MDCK II organoids here. This can possibly be achieved by microfabrication of a smaller circular-shaped microtrap

using laser ablation.[40] Further improvements on the estimation of R_{sph} will be also addressed in the future by correlating the spheroid impedance with its volume instead of the contact surface area between spheroid and microtrap.

4.6 Material & Method

OECT fabrication

Planar OECTs were fabricated on conventional microscope glass slides (75x25 mm^2). Thermally evaporated gold defined source, drain, and gate tracks, patterned *via* lift-off lithography. PEDOT:PSS (Heraeus, Clevios PH 1000) transistor channels of 25x25 μm^2 and gate electrodes (4x4 mm^2) were created using an adapted version of the parylene C (PaC) peel-off technique.[35] Briefly, following gold lift-off an anti-adhesive layer (2% v/v industrial cleaner, Micro-90) was spin-coated (1000 rpm, 30 seconds) on the glass slide followed by deposition of a single 2 μm thick layer of parylene C (PaC). AZ9260 photoresist was then spin-coated, exposed, and developed in AZ developer (AZ Electronic Materials) followed by reactive ion etching (Oxford 80 Plasmalab plus) of the unprotected layer of PaC in order to define openings for PEDOT:PSS deposition. The conducting polymer formulation consisted of PEDOT:PSS, ethylene glycol (Sigma Aldrich, 0.25 mL for 1 mL PEDOT:PSS solution), 4-dodecylbenzenesulfonic acid (DBSA, 0.5 μL mL^{-1}) and 3-glycidoxypropyltrimethoxysilane (GOPS) (10 mg mL^{-1}). To enhance the adhesion of the PEDOT:PSS layer to the gold contacts during PaC peel-off, a monolayer of 3-mercaptopropyltrimethoxysilane (MPTMS) was formed on the gold by exposing the substrate to a 10 mM solution (3:1 volume iso-propyl alcohol (IPA)/de-ionised water (DI)) for 1 min, then rinsed with IPA and DI and blown dry with nitrogen. Prior to spin-coating of the PEDOT:PSS solution, the glass slides were O_2 plasma activated (25 Watt, 120 seconds) to promote hydrolysis and activation of the MPTMS.[41] The resulting devices were subsequently baked at 130 °C for 1 h followed by 2 rinsing/soaking cycles in deionized water to wash away any unbound low density molecular-weight material from the OECT channel and gate.

Microtrap fabrication

The PDMS microfluidic trapping device was fabricated by standard soft lithography *via* SU-8 replica moulding. A silicon wafer was rinsed with acetone, IPA and DI water and then blown dry with nitrogen. The wafer was then placed in an oven at 150°C under vacuum for at least 3 hours to de-hydrate the silicon wafer and improve SU-8 adhesion. A single 250 μm thick layer of SU-8 2075 (MicroChem Corp) was spin-coated on the wafer, followed by pre-exposure baking, i-line (λ=365 nm) exposure, post-exposure baking and development. The final master mould was then treated with an anti-adhesive layer of perfluorodecyltrichloro-silane (Nanonex nanoimprintor) to facilitate demoulding of the cured PDMS. PDMS elastomer and curing agent were mixed truly in a 10:1 weight ratio, poured on the master mould and cured at 60°C overnight.

To create a circular-shaped microtrap, the un-sealed PDMS microtrap was modified as follows: (1) a glass capillary (outer diameter 80 μm) was carefully placed inside the PDMS squared microtrap (width 100 μm, height 250 μm). (2) A 125 μm thin foil of polyimide was placed on top in order to provide a reversible seal of the microtrap device. The polyimide foil was fixed in position using polyimide tape. (3) A small drop of uncured PDMS was allowed to flow by capillarity inside the microchannel in order to fill the gaps in between the cured PDMS microtrap and the glass capillary. The device was then placed in a pre-heated oven at 120°C for 2 minutes in order to achieve a fast curing rate of the PDMS around the glass capillary. (4) The glass capillary was gently pulled out from the trap and the polyimide foil was then removed. The modified PDMS microtrap device was then fully cured for 2 hours at 80°C. Detailed schematics of the fabrication steps are reported in Figure S1. Finally, inlet and outlet ports were punched in the PDMS and both microtrap and OECT device were plasma activated to obtain irreversible sealing of the microtrap device with the planar OECT.

3D Spheroid cell culture

Human telomerase immortalized fibroblasts (TIF) (a gift from Ellen Van Obberghen-Schilling (Institut de Biologie de Valrose)) and green fluorescent canine epithelial kidney cells (MDCK II eGFP) cells (a gift from Frederic Luton (IPMC, Valbonne)) were used to prepare spheroids for both mono and co-culture.

TIF pLifeAct were transfected with p^{CMV}LifeAct–TagRFP (ibidi GmbH) to achieve stable expression of red fluorescent labelling of F-actin protein. The cells were cultivated in DMEM (Advanced DMEM Reduced Serum Medium 1X, Invitrogen) with 2 mM glutamine (Glutamaxt-1, Invitrogen), 10% FBS (Fetal Bovine Serum, Invitrogen), 0.5% PenStrep (PenStrep100X, Invitrogen) and 0.1% Gentamicin (Gentamicin 100X, Invitrogen). Briefly, spheroids growth was performed using a 96 well hanging drop plate (InSphero, Switzerland). 40 μL cell suspensions of TIF pLifeAct and/or MDCK II eGFP were used to fill each hanging drop well. 1000 and 2000 cells per drop were used for the formation of two different sizes of TIF pLifeACT spheroids. MDCK II eGFP spheroids were cultured starting from 500 cells per drop, while TIF pLifeAct/MDCK II eGFP co-culture spheroids were prepared using a cell ratio of 2:1 (1000-500 cells), respectively. This ratio was found to be optimal for enhancing self-organization of the spheroid with a characteristic core-shell structure (core: TIF pLifeAct; shell: MDCK II eGFP). Spheroid circularity was promoted using cell culture media containing 3.83 mg/mL dextran complement (Sigma-Aldrich, Switzerland), Figure S2.[42] Spheroids were cultured for 3 days in an incubator at 37°C, 95% Humidity, 5% CO_2.

OECTs operation and data analysis

For the operation of the OECTs, a National Instruments PXIe-1062Q system was employed. A source-measurement unit (SMU) NI PXIe-4145 was used to bias the channel of the OECT (V_{DS}), while gate potential was applied and controlled using a NI PXI-6289, a multifunction data acquisition (DAQ) module. For frequency-dependent measurements, output currents of the drain (I_D) and the gate (I_G) were recorded using two NI-PXI-4071 digital multimeters (DMM). The bandwidth measurements were performed by applying a sinusoidal modulation at the gate electrode (ΔV_{GS} = 50 mV peak-to-peak, 1 Hz < f <20 kHz) while keeping a constant bias at the drain (V_{DS} = −0.5 V). Measurements parameters were controlled using a customized LabVIEW program. Fitting of the frequency-dependent measurements to extract spheroid resistance (R_{sph}) was performed using a Matlab script, as reported previously.[25] Spheroid resistance values expressed in $\Omega \cdot cm^2$ were obtained using a cell area equal to the contact surface area between the spheroid and the microtrap. When using TIF and TIF/MDCK II

spheroids, we estimated a cell area equal to the cross-section surface of the circular-shaped trap (diameter of 80 μm). For MDCK II spheroids, the total cell area was calculated by also considering the lateral contact surface between spheroid and microtrap in addition to the cross-section surface of the circular-shaped trap.

4.7 Acknowledgments

VFC. acknowledges support from a Marie Curie post-doctoral fellowship FP7-PEOPLE-2013-IEF, Project No. 624673. RMO would like to acknowledge the ANR 3Bs project, and an Ecole des Mines de St. Etienne doctoral fellowship for MPF. FM. acknowledges funding provided by the European Erasmus+ Program.

4.8 References

1. Shamir, E. R. & Ewald, A. J. Three-dimensional organotypic culture: experimental models of mammalian biology and disease. Nat. Rev. Mol. Cell Biol. 15, 647–664 (2014).

2. Elliott, N. T. & Yuan, F. A Review of Three-Dimensional In Vitro Tissue Models for Drug Discovery and Transport Studies. J. Pharm. Sci. 100, 59–74 (2011).

3. Carletti, E., Motta, A. & Migliaresi, C. Scaffolds for Tissue Engineering and 3D Cell Culture. in 3D Cell Culture: Methods and Protocols (ed. Haycock, J. W.) 17–39 (Humana Press, 2011). doi:10.1007/978-1-60761-984-0_2

4. Achilli, T.-M., Meyer, J. & Morgan, J. R. Advances in the formation, use and understanding of multi-cellular spheroids. Expert Opin. Biol. Ther. 12, 1347–1360 (2012).

5. Oltolina, F. et al. Human Cardiac Progenitor Spheroids Exhibit Enhanced Engraftment Potential. PLoS ONE 10, (2015).

6. Polonchuk, L. et al. Cardiac spheroids as promising in vitro models to study the human heart microenvironment. Sci. Rep. 7, 7005 (2017).

7. Lee, S.-A. et al. Spheroid-based three-dimensional liver-on-a-chip to investigate hepatocyte–hepatic stellate cell interactions and flow effects. Lab. Chip 13, 3529–3537 (2013).

8. Bell, C. C. et al. Characterization of primary human hepatocyte spheroids as a model system for drug-induced liver injury, liver function and disease. Sci. Rep. 6, srep25187 (2016).

9. Yonemura, S. Differential Sensitivity of Epithelial Cells to Extracellular Matrix in Polarity Establishment. PLOS ONE 9, e112922 (2014).

10. Ray, K. Intestinal tract: Patient-derived intestinal spheroids—culturing the gut. Nat. Rev. Gastroenterol. Hepatol. 11, 516–516 (2014).

11. Tung, Y.-C. et al. High-throughput 3D spheroid culture and drug testing using a 384 hanging drop array. Analyst 136, 473–478 (2011).

12. Li, L., Zhou, Q., Voss, T. C., Quick, K. L. & LaBarbera, D. V. High-throughput imaging: Focusing in on drug discovery in 3D. Methods 96, 97–102 (2016).

13. Friedrich, J., Seidel, C., Ebner, R. & Kunz-Schughart, L. A. Spheroid-based drug screen: considerations and practical approach. Nat. Protoc. 4, 309–324 (2009).

14. McMillan, K. S., Boyd, M. & Zagnoni, M. Transitioning from multi-phase to single-phase microfluidics for long-term culture and treatment of multicellular spheroids. Lab. Chip 16, 3548–3557 (2016).

15. Silva, P. N., Green, B. J., Altamentova, S. M. & Rocheleau, J. V. A microfluidic device designed to induce media flow throughout pancreatic islets while limiting shear-induced damage. Lab. Chip 13, 4374 (2013).

16. Kwapiszewska, K., Michalczuk, A., Rybka, M., Kwapiszewski, R. & Brzózka, Z. A microfluidic-based platform for tumour spheroid culture, monitoring and drug screening. Lab Chip 14, 2096–2104 (2014).

17. Liu, W., Wang, J.-C. & Wang, J. Controllable organization and high throughput production of recoverable 3D tumors using pneumatic microfluidics. Lab. Chip 15, 1195–1204 (2015).

18. Ruppen, J. et al. A microfluidic platform for chemoresistive testing of multicellular pleural cancer spheroids. Lab Chip 14, 1198–1205 (2014).

19. Frey, O., Misun, P. M., Fluri, D. A., Hengstler, J. G. & Hierlemann, A. Reconfigurable microfluidic hanging drop network for multi-tissue interaction and analysis. Nat. Commun. 5, (2014).

20. Lo, C. M., Keese, C. R. & Giaever, I. Impedance analysis of MDCK cells measured by electric cell-substrate impedance sensing. Biophys. J. 69, 2800–2807 (1995).

21. Srinivasan, B. et al. TEER measurement techniques for in vitro barrier model systems. J. Lab. Autom. 20, 107–126 (2015).

22. Kloß, D., Fischer, M., Rothermel, A., Simon, J. C. & Robitzki, A. A. Drug testing on 3D in vitro tissues trapped on a microcavity chip. Lab. Chip 8, 879–884 (2008).

23. Rismani Yazdi, S. et al. Adding the ‘heart’ to hanging drop networks for microphysiological multi-tissue experiments. Lab Chip 15, 4138–4147 (2015).

24. Schmid, Y. R. F., Bürgel, S. C., Misun, P. M., Hierlemann, A. & Frey, O. Electrical Impedance Spectroscopy for Microtissue Spheroid Analysis in Hanging-Drop Networks. ACS Sens. 1, 1028–1035 (2016).

25. Rivnay, J. et al. Organic electrochemical transistors for cell-based impedance sensing. Appl. Phys. Lett. 106, 043301 (2015).

26. Khodagholy, D. et al. High transconductance organic electrochemical transistors. Nat. Commun. 4, 2133 (2013).

27. Pappa, A.-M. et al. Organic Transistor Arrays Integrated with Finger-Powered Microfluidics for Multianalyte Saliva Testing. Adv. Healthc. Mater. n/a-n/a (2016). doi:10.1002/adhm.201600494

28. Gualandi, I. et al. Selective detection of dopamine with an all PEDOT:PSS Organic Electrochemical Transistor. Sci. Rep. 6, (2016).

29. Khodagholy, D. et al. In vivo recordings of brain activity using organic transistors. Nat. Commun. 4, 1575 (2013).

30. Yao, C., Li, Q., Guo, J., Yan, F. & Hsing, I.-M. Rigid and Flexible Organic Electrochemical Transistor Arrays for Monitoring Action Potentials from Electrogenic Cells. Adv. Healthc. Mater. 4, 528–533 (2015).

31. Jimison, L. H. et al. Measurement of Barrier Tissue Integrity with an Organic Electrochemical Transistor. Adv. Mater. 24, 5919–5923 (2012).

32. Curto, V. F. et al. Organic transistor platform with integrated microfluidics for in-line multi-parametric in vitro cell monitoring. Microsyst. Nanoeng. 3, micronano201728 (2017).

33. Huerta, M., Rivnay, J., Ramuz, M., Hama, A. & Owens, R. M. Research Update: Electrical monitoring of cysts using organic electrochemical transistors. APL Mater. 3, 030701 (2015).

34. DeFranco, J. A., Schmidt, B. S., Lipson, M. & Malliaras, G. G. Photolithographic patterning of organic electronic materials. Org. Electron. 7, 22–28 (2006).

35. Sessolo, M. et al. Easy-to-Fabricate Conducting Polymer Microelectrode Arrays. Adv. Mater. 25, 2135–2139 (2013).

36. Ramuz, M. et al. Combined Optical and Electronic Sensing of Epithelial Cells Using Planar Organic Transistors. Adv. Mater. 26, 7083–7090 (2014).

37. Pappa, A.-M. et al. Organic Transistor Arrays Integrated with Finger-Powered Microfluidics for Multianalyte Saliva Testing. Adv. Healthc. Mater. 5, 2295–2302 (2016).

38. Hildebrandt, C., Büth, H., Cho, S., Impidjati, null & Thielecke, H. Detection of the osteogenic differentiation of mesenchymal stem cells in 2D and 3D cultures by electrochemical impedance spectroscopy. J. Biotechnol. 148, 83–90 (2010).

39. Luongo, K. et al. Microfluidic device for trapping and monitoring three dimensional multicell spheroids using electrical impedance spectroscopy. Biomicrofluidics 7, (2013).

40. Hsieh, Y.-K. et al. Direct Micromachining of Microfluidic Channels on Biodegradable Materials Using Laser Ablation. Polymers 9, (2017).

41. Wu, W., Wu, J., Kim, J.-H. & Lee, N. Y. Instantaneous room temperature bonding of a wide range of non-silicon substrates with poly(dimethylsiloxane) (PDMS) elastomer mediated by a mercaptosilane. Lab. Chip 15, 2819–2825 (2015).

42. Leung, B. M., Lesher-Perez, S. C., Matsuoka, T., Moraes, C. & Takayama, S. Media additives to promote spheroid circularity and compactness in hanging drop platform. Biomater. Sci. 3, 336–344 (2015).

Chapter 5: Dynamic blood brain barrier 3D model with integrated real-time electrical cell barrier monitoring

Publication Status: *This chapter has not been published or submitted for publication at the time of submission of this thesis*. This chapter is a manuscript in preparation.

Collaborators: *Dr Vincenzo F. Curto[1], Dr Rayan Nagao[2], Dr Ying Zheng[2], Dr Roisin M. Owens[1,3]*
[1]Mines Saint-Étienne Department of Bioelectronics
[2]University of Washington Department of Bioengineering
[3]Cambridge University Department of Chemical Engineering and Biotechnology

5.1 Abstract

Organ-on-a-chip systems constitute an emerging class of 3D models that aim to provide the right environment to mimic how cells work in human bodies. These chips are made of microfluidic chambers that are lined by cells. Media flow is continuously pumped through the chambers and mechanical stress can be applied to the tissues to simulate physiological process such as breathing. Impedance spectroscopy is a powerful technique to assess *in vitro* barrier tissue ionic selectivity. It is mainly performed using rigid metal electrodes placed in either side of the tissue. However, integration of these electrodes within a micron-size chamber is challenging and brings the risk of cell damage and tissue contamination. Here we show the integration of organic electrochemical transistors (OECTs) within a blood brain barrier (BBB)-on-a-chip system to perform on-line impedance sensing of the BBB.

5.2 Introduction

Preclinical animal testing becomes more and more controversial and is expected to be substituted by predictive *in vitro* cell culture models to a large extent. One of the most commonly used *in vitro* models relies on the 2D culture of cells on static configurations. These models are cheap and easy to handle and have made significant advancements in biological research. However, they exhibit intrinsic limitations due to a lack of mechanical tunability and an inaccurate mimicking of cell microenvironment.[1] As such, mechanical and biochemical cues coming from the native environment are mostly absent. To overcome these issues

and promote cell-cell and cell-matrix interactions, alternative 3D models are proposed such as microfluidic organ-on-a-chip systems.[2]

Progress made in tissue engineering and microfabrication allowed the emergence of organ-on-a-chip devices that mimic functional units of a specific organ or tissue.[3] These devices are composed by continuously perfused micron-sized chambers that are lined by cells. Several organs-on-chips have been developed in the past few years, such as lung-on-a-chip array and vessel-on-a-chip system.[4,5] Organ-on-a-chip devices have been bridged together to form a body-on-a-chip system, which is able to mimic the complex multi-organ interactions. The field of organs-on-chips is fast developing toward a higher-level systemic function.[6] However, few tools is available for the on-line characterization of these models. As a result, the integration of in-line monitoring systems with organs-on-chips devices is in high demand.

The transendothelial resistance (TER) is a powerful label-free technique to quantify ionic selective barrier properties in vessel-on-a-chip devices. The method usually uses two metal electrodes placed on either sides of the barrier tissue and connected through an electrolyte.[7] A low voltage (kHz) is applied between these electrodes and the resulting current is measured. The design of an electrical equivalent circuit allows the extraction of the TER value. TER value increases with the ionic barrier tightness. The integration of metal electrodes with organ-on-a-chip device is challenging. Tiny wires have been introduced into the channel but they pose the risk to damage the cell layer or bring contamination into the device.[8,9] Electrodes have also been embedded into the poly-dimethylsiloxane (PDMS) structure.[10] In that case, artifactual differences in measured resistance values can come from electrode size and distance from the cell layer.

To solve these issues, the emerging field of organic bioelectronics proposes unique tools for barrier tissue resistance measurements.[11] They present millisecond temporal resolution to detect barrier tissue disruption.[12] These tools could also bridge the gap between rigid electrodes and soft tissues[13]. As an interesting tool, the organic electrochemical transistor (OECT) comprises a thin layer of conducting polymer that acts as the active material. The OECT is composed by three metal electrodes (source, drain and gate) in which the conducting polymer is deposited between the source and the drain to form the

channel of the transistor. The gate and the channel of the transistor are connected through an electrolyte. Poly(3,4-ethylenedioxythiophene) doped with poly(styrene sulfonate) anions (PEDOT/PSS) is commonly used as the active material due to its easy access, chemical tunability and biocompatibility. PEDOT:PSS solution is easy to process , which implies flexible OECT design for the integration into customized *in vitro* cell models such as organs-on-chips. The working principle of the OECT relies on the injection of ions coming from the electrolyte into the active area upon the application of a gate bias. The electrochemical doping/de-doping state of the channel serves as an efficient ion-to-electron transducer. OECTs have been used for a range of applications including bio-sensing, *in vivo* brain recording activity and *in vitro* measurement of barrier tissue integrity. Similar to commercially available cell-based impedance sensing (ECIS, xCelligence), OECTs provide information on cell layer resistance and capacitance operating in an AC regime. Notably, OECTs are compatible with bright field and fluorescence confocal microscopy. OECT technology has already been successfully integrated into an organ-on-a-chip device to provide multi-parametric *in vitro* cell monitoring[14].

Here we demonstrate for the first time the integration of OECTs with 3D *in vitro* microvessels to study blood brain barrier (BBB) formation. We demonstrate that human cerebellar microvascular endothelial cells (hCMEC/D3) are able to form an ionic barrier when cells are cultured in a tubular configuration. In addition to this, we show that the OECTs can monitor faster changes in the cell layer resistance when cells are cultured in the channels compared to a planar configuration. This technology offers great promise to investigate *in vitro* BBB formation under physiological conditions.

5.3 Results

5.3.1 Engineering 3D fluidic brain microvascular network

The design of a large majority of organ-on-a-chip devices published in the literature relies on soft lithography techniques using SU-8 resin to fabricate a silicon mold[15]. This mold shapes a PDMS layer that is permanently bonded to a stiff and flat substrate such as glass. This irreversible adhesion takes place following O_2 plasma activation of both the glass and the PDMS, which allows

fluidic device to support long-term operation. In these devices, cells are cultured in monolayer on top of the glass substrate following the shape of the channel that is delimited by the PMDS. Fluidic devices allow the application of a flow shear stress i.e. mechanical stimulation on the cell layer.

In the present work, we engineered the microvessel network via soft lithography technique in a type I collagen gel at 6 mg/mL^{-1}.[5,16] This collagen stiffness exhibits a modulus of about 200 Pa, which allows high reproducibility in the microvessel network structure. Contrary to previously described fluidic devices, we are using collagen to design the micron-size channels instead of PMDS. The native collagen presents the advantage to offer cell binding peptide domain such as GFOGER-domain and enables remodeling through degradation and deposition of extracellular matrix[17]. The design of the present organ-on-a-chip system proposes integration of deviations from the standard tubular-shape vessels (corners and bifurcations). Bifurcations have been shown as particularly fragile zones where local changes in shear stress could initiate changes in endothelial cells physiology and related impairments in barrier integrity[18]. Human brain microvascular endothelial cells (hCMEC/D3) were seeded into the fluidic structure to create an endothelialized lumen that is perfused by a gravity driven flow. The gravity driven flow is estimated to generate a low shear stress of about 0-10 $dyne.cm^{-2}$.[5]

5.3.2 OECTs integration with organ-on-a-chip device

In the present study, planar OECT are fabricated with both the transistor channel and the gate electrode patterned onto the same substrate through liftoff lithography. To insulate gold contacts and define active areas in the OECT, we use a thin parylene C (PaC) layer of ~2 μm, a derivative of poly(p-xylylene) presenting high mechanical and chemical stability and biocompatibility. In order to investigate the impact of cell seeding configuration on the BBB barrier formation, hCMEC/D3 cells were seeded on top of the microscope glass slide containing OECTs, with and without integration with the fluidic device. **Figure 5.1** shows an illustration of the fully assembled fluidic device with microvessel network design and integrated OECTs. hCMEC/D3 cells are seeded on the wall of the micron-size chambers. The proposed-platform is made of multiple

interconnected microchannels within which multiple OECT channels and gates are integrated on the bottom surface of the structure. Original fluidic channels defined lithographically should have a diameter of 100-150µm.

To evaluate the impact of micron-size tubular shape configuration on hCMEC/D3 cell layer tight-junction formation, we proceeded to a fluorescent immunostaining against the tight junction adaptor protein zona occludens-1 (ZO-1). **Figure 5.1b** shows a fluorescence image using ZO-1 antibody and fluorescent microscopy of hCMEC/D3 cells cultured in a 2D (left) and 3D (right) configuration. These images were obtained after maintaining the confluent monolayer during 5 days in EGM-2 media without vascular endothelial growth factor (VEGF). An increase in the fluorescent staining induced by the 3D cell culture configuration was observed compared to the 2D cell culture. The change in ZO-1 expression is more evident in the edge of cells, due to a protein relocalization from cell cytoplasm toward the tight-junction areas.

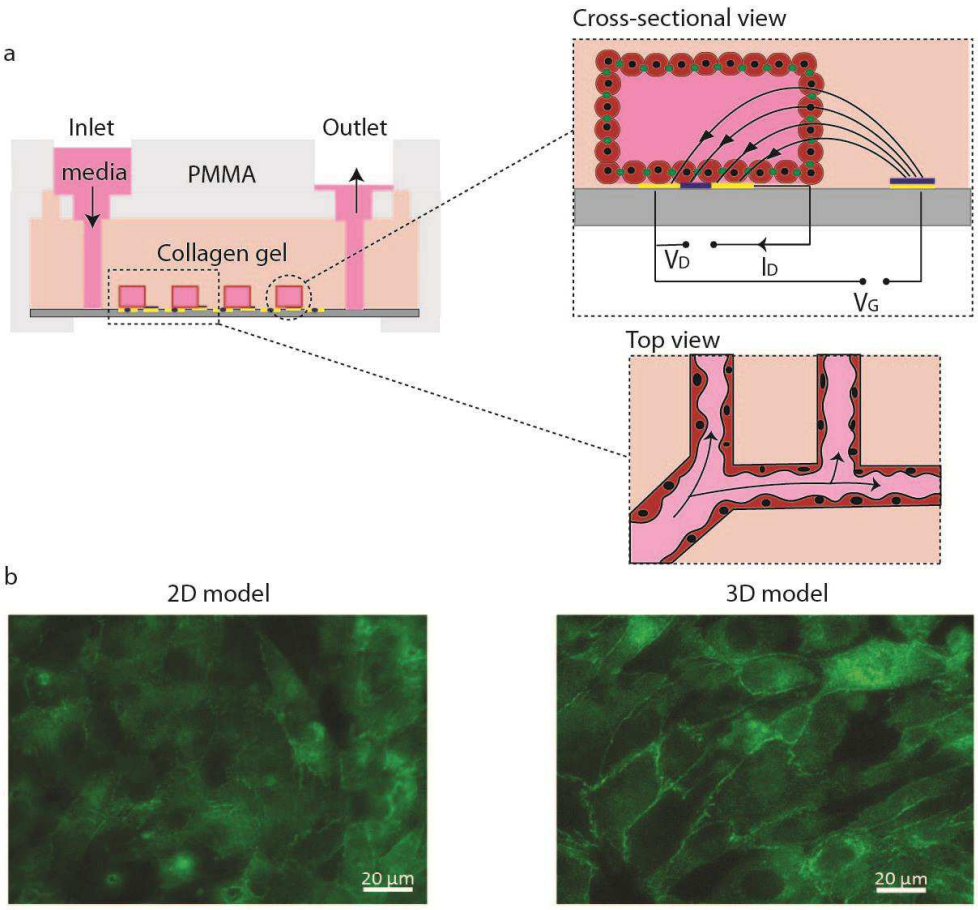

Figure 5.1: Integration of OECTs within microvessel-on-a-chip device. ***a) (left)*** *Graphical representation of the organ-on-a-chip platform cross-section*

*integrated with the OECT technology. **(right)** Top right, illustration of an OECT and the microvessel on top surrounded by collagen wall. Bottom right, top view of the microvessel networks and flow direction (black arrows). **b)** ZO-1 fluorescence image of a fully confluent layer of hCMEC/D3 after 7 days of culture in 2D model configuration **(left)** and 3D model configuration **(right)** (scale bar, µm).*

5.3.3 Blood brain barrier formation in 2D model vs 3D model

Subsequently we evaluated the ability of hCMEC/D3 cells to form a selective ionic barrier in both configurations. The first experiment was performed in the classic, static configuration using a glass well to contain cell culture media. **Figure 5.2a** shows plots of the OECT transconductance ($g_m = \Delta I_D/\Delta V_G$) over the five days of cell barrier culture when applying a gate voltage of 50 mV over a range of frequency from 1Hz to 10 kHz. The electronic monitoring of the barrier formation was performed measuring the OECT as a 3-terminal device every 24 hours after removing vascular endothelial growth factor (VEGF) from the media. Before addition of the cells, the cutoff-frequency of the OECT is ~900 Hz (black curve). Following hCMEC/D3 confluency, the cut-off frequency decreases gradually. This decrease is corresponding to the seal of the barrier by tight junctions and reaches a value of ~50Hz after 5 days. **Figure 5.2b** shows the time evolution of the frequency-dependent response of the OECT after culture of hCMEC/D3 cells in the fluidic device. After 3 days of cell barrier culture within the micron-size collagen structure, the cut-off frequency reaches ~40Hz, which is notably lower than the 2D configuration (~70 Hz).

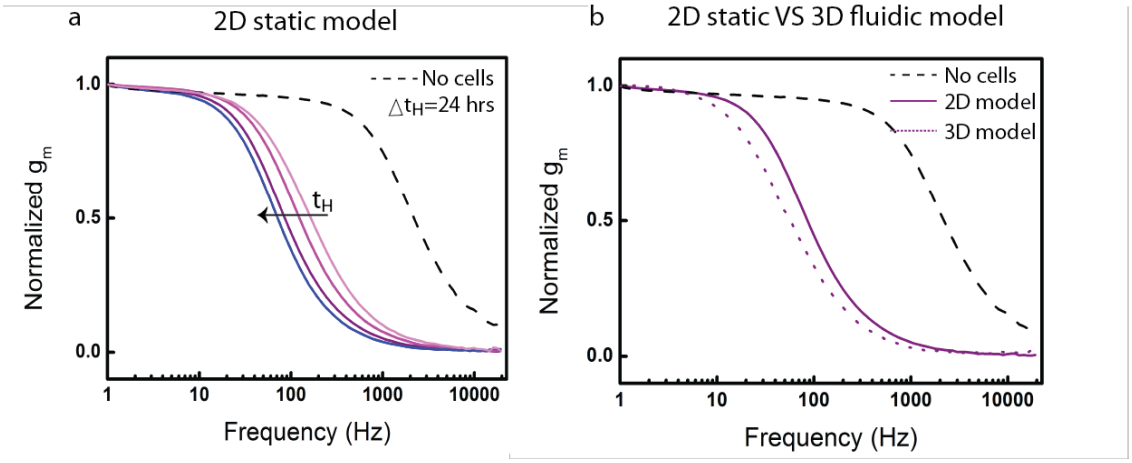

Figure 5.2: Electrical characterization of blood brain barrier ionic permeability. ***a)*** *Typical time evolution of the OECT frequency-dependent*

response during BBB cell barrier culture in 2D configuration. Confluent cell monolayer is maintained in culture for 5 days and OECT response is measured every 24 hours. Progressive sealing of the barrier by tight junctions induces a continuous shift in the OECT cutoff frequency from ~900Hz (dashed black line) to ~50Hz (solid blue line). ***b)*** *OECT frequency-dependent response after 3 days of cell barrier culture in planar static configuration (2D model) vs in microvascular network configuration (3D model).*

5.4 Discussion and Conclusion

One of the main advantages of using OECT technology as a sensor for cell barrier impedance sensing is the possibility to integrate micron-sized electrodes with an organ-on-a-chip structure in a compact manner without impairing cell visualization. With the rapid expansion of organ-on-a-chip field and the associated biological complexification, there is an urgent need for the coupling of these biological devices with sensing platforms able to provide real-time barrier tissue sensing.

Previously, the OECT technology has already been successfully integrated within a microfluidic platform. OECTs have been used as highly sensitive label-free sensor based on multi parametric *in vitro* cell monitoring. The diversity of OECT applications within biological environment allowed the monitoring of several parameters such as impedance monitoring, metabolite sensing and wound-healing assay. In the present study, we show that OECTs can be integrated into more complex fluidic systems where micron-size chambers are designed within a collagen gel. This device allowed the culture of brain microvascular endothelial cells in a 3D configuration while enabling substrate remodeling.

As preliminary results, we clearly demonstrate in this study the ability of planar OECTs to be integrated into organ-on-a-chip devices and used as in-line sensors for ionic cell-barrier quantification. The formation of the BBB has been shown to be faster and tighter when cells are cultured in the 3D fluidic model compared to the conventional 2D cell culture configuration.

Future projects will concentrate on culturing pericytes and astrocytes along the capillary wall or embedded into the collagen gel. This configuration will allow the reconstitution of neurovascular unit. This platform may be considered as a powerful tool for toxicological assays.

5.5 Material & Methods

OECT fabrication and operation

Thermally evaporated gold source, drain, and gate contacts of the OECT were defined on a microscope glass slide via liftoff lithography. Transistor channels of 50 × 50 μm, and gate electrodes (2 × 2 mm) were patterned using a parylene C (PaC) peel-off technique as described previously[19]. PEDOT:PSS (Heraeus, Clevios PH1000, Hanau, Germany) conducting polymer was used as the active layer for the OECT channel and gate electrode. The conducting polymer formulation consisted of PEDOT:PSS, ethylene glycol (Sigma-Aldrich, St. Louis, MO, USA, 0.25 mL for 1 mL PEDOT:PSS solution), 4-dodecylbenzenesulfonic acid (DBSA, 0.5 μL mL− 1) and 3-glycidoxypropyltrimethoxysilane (GOPS) (10 mg mL− 1). Before use of the OECTs, the microscope glass slides were soaked in de-ionised (DI) water overnight to wash away any unbound material from the OECT channel and gate. For the operation of the OECTs, a National Instruments PXIe-1062Q system was employed. A source-measurement unit NI PXIe-4145 was used to bias the channel of the OECT (VDS), while gate potential was applied and controlled using an NI PXI-6289, a multifunction data acquisition module. For frequency-dependent measurements, output currents of the drain (Id) and the gate

(Ig) were recorded using two NI-PXI-4071 digital multimeters. The bandwidth measurements were performed by applying a sinusoidal modulation at the gate electrode (ΔVgs = 50 mV peak-to- peak, 1 Hz to 10 kHz) while keeping a constant bias at the drain (VDS = − 0.4 V). Measurements parameters were controlled using a customized LabVIEW program. For fitting of the frequency dependent measurements, a MATLAB script was used to extract the cell layer resistance and capacitance as reported previously[20].

Microvessel network fabrication and operation

Our organ-on-a-chip device was fabricated by the assembly of a flat bottom piece and a top piece. Both pieces were assembled using housing device made with poly(methyl methacrylate) (PMMA). Microscope glass slide containing OECTs was coated with type I collagen 0.1 $mg.mL^{-1}$ during 1 hour at room temperature. It was forming the bottom piece of the device. The top part of the device showing microvessel networks were fabricated using native, type I collagen by molding

microstructures in collagen gels with injection molding techniques[16]. Briefly, PDMS stamps containing the network design were fabricated by standard soft lithography via SU-8 replica moulding. Type I collagen 6 $mg.mL^{-1}$ were injected in between the PDMS mold and the upper part of the housing device. After 20 minutes of incubation at 37°C, to allow collagen gelification, the PDMS stamp was removed. The bottom and the top part of the device where assembled using a housing device made with poly(methyl methacrylate) (PMMA). Prior the injection of collagen, the PMMA structure was coated with 1% Polyethyleneimine during 10 minutes and then 0.1% glutaraldehyde during 30 minutes to optimize collagen-PMMA attachment.

Collagen gel for microvessel formation was prepared by mixing collagen 10 $mg.mL^{-1}$ (Ibico) with MEM 10X (Sigma) and endothelial growth medium-2 (EGM-2) cell culture medium (Lonza). The pH of the collagen gel was neutralized using NaOH 1M solution.

The fluidic system is created by the sealing together of the microscope glass slide and the collagen layer to form enclosed fluidic structure by applying pressure within the housing device.

Cell culture

hCMEC/D3 cells (human cerebellar microvascular endothelial cells) were gently donated by Pr. Nacho (Open University, UK). Cells were grown at 80% confluency in a cell culture flask coated with 0.1 $mg.mL^{-1}$ and incubated with trypsin (0.25%) at 37°C for 1-2 min. The collected cells were resuspended in fresh EGM-2 media with 2.5% FBS to a final concentration of ~5 x 10^5 cells mL^{-1} and then seeded on top of the microscope glass slide (2D model configuration) or inside the fluidic channel (for 3D model configuration) and let adhere for ~30 minutes. After seeding cells were cultured under static condition (2D model) or under a gravity driven flow (3D model) for ~3 days in EGM-2 supplemented with 0.025% VEGF to reach 100% confluency. Cells were then cultured additional 5 days with media without VEGF to promote barrier maturation. Inlet reservoir was refilled every 12 hours while outlet reservoir was emptied in order to keep a gravity driven flow.

ZO-1 immunostaining

Cells were fixed with 4% paraformaldehyde during 10 minutes at room temperature. After cells were blocked with a solution of 1% bovine serum albumin (BSA) during 30 minutes, cell membranes were permeabilized by rinsing the cell layer with 0.025% tween-20 solution. Incubation with primary antibody against ZO-1 (Thermofisher) protein happened overnight at 4°C. The secondary antibody (IgG-488, Thermofisher) was incubated 2 hours at room temperature. Samples were imaged using fluorescent microscope (Axio Observer Z1 Carl Zeiss).

5.6 Acknowledgments

V.F.C. acknowledges support from a Marie Curie post-doctoral fellowship FP7-PEOPLE-2013-IEF, Project No. 624673. M.P.F acknowledges support from Agence Nationale de la Recherche 3Bs project and Ecole des Mines Saint-Etienne/Institut Mines Télécom for Bourse Ecole. V.F.C. acknowledges Dr Rayan Nagao and Dr Ying Zheng (University of Washington) for shearing technical expertise on microvessel network engineering.

5.7 References

1. Pampaloni, F., Reynaud, E. G. & Stelzer, E. H. The third dimension bridges the gap between cell culture and live tissue. *Nature reviews Molecular cell biology* **8,** 839–845 (2007).

2. Bhatia, S. N. & Ingber, D. E. Microfluidic organs-on-chips. *Nature Biotechnology* **32,** 760–772 (2014).

3. Arık, Y. B. *et al*. Barriers-on-chips: Measurement of barrier function of tissues in organs-on-chips. *Biomicrofluidics* **12,** 042218 (2018).

4. Benam, K. H. *et al*. Matched-Comparative Modeling of Normal and Diseased Human Airway Responses Using a Microengineered Breathing Lung Chip. *Cell Systems* **3,** 456-466.e4 (2016).

5. Zheng, Y. *et al*. In vitro microvessels for the study of angiogenesis and thrombosis. *Proceedings of the National Academy of Sciences* **109,** 9342–9347 (2012).

6. Guenat, O. T. & Berthiaume, F. Incorporating mechanical strain in organs-on-a-chip: Lung and skin. *Biomicrofluidics* **12,** 042207 (2018).

7. Srinivasan, B. *et al*. TEER measurement techniques for in vitro barrier model systems. *Journal of laboratory automation* **20,** 107–126 (2015).

8. Shah, P. *et al*. A microfluidics-based in vitro model of the gastrointestinal human–microbe interface. *Nature Communications* **7,** 11535 (2016).

9. van der Helm, M. W. *et al*. Direct quantification of transendothelial electrical resistance in organs-on-chips. *Biosensors and Bioelectronics* **85,** 924–929 (2016).

10. Henry, O. Y. F. *et al*. Organs-on-chips with integrated electrodes for trans-epithelial electrical resistance (TEER) measurements of human epithelial barrier function. *Lab Chip* **17,** 2264–2271 (2017).

11. Jimison, L. H. *et al*. Measurement of Barrier Tissue Integrity with an Organic Electrochemical Transistor. *Advanced Materials* **24,** 5919–5923 (2012).

12. Ramuz, M., Hama, A., Rivnay, J., Leleux, P. & Owens, R. M. Monitoring of cell layer coverage and differentiation with the organic electrochemical transistor. *J*. *Mater*. *Chem*. *B* **3,** 5971–5977 (2015).

13. Rivnay, J. *et al*. Organic electrochemical transistors. *Nature Reviews Materials* **3,** 17086 (2018).

14. Curto, V. F. *et al*. Organic transistor platform with integrated microfluidics for in-line multi-parametric in vitro cell monitoring. *Microsystems & Nanoengineering* **3,** 17028 (2017).

15. Roberts, M. A., Kotha, S. S., Phong, K. T. & Zheng, Y. Micropatterning and Assembly of 3D Microvessels. *Journal of Visualized Experiments* (2016). doi:10.3791/54457

16. Zheng, Y., Chen, J. & López, J. A. Microvascular platforms for the study of platelet-vessel wall interactions. *Thrombosis Research* **133,** 525–531 (2014).

17. Hinderer, S., Layland, S. L. & Schenke-Layland, K. ECM and ECM-like materials — Biomaterials for applications in regenerative medicine and cancer therapy. *Advanced Drug Delivery Reviews* **97,** 260–269 (2016).

18. Gray, K. M. & Stroka, K. M. Vascular endothelial cell mechanosensing: New insights gained from biomimetic microfluidic models. *Seminars in Cell & Developmental Biology* **71,** 106–117 (2017).

19. DeFranco, J. A., Schmidt, B. S., Lipson, M. & Malliaras, G. G. Photolithographic patterning of organic electronic materials. *Organic Electronics* **7,** 22–28 (2006).

20. Rivnay, J. *et al*. Organic electrochemical transistors for cell-based impedance sensing. *Applied Physics Letters* **106,** 043301 (2015).

Chapter 6: New materials for *in vitro* blood brain barrier models

Publication Status: *This chapter has not been published or submitted for publication at the time of submission of this thesis*. This chapter is a manuscript in preparation.

Collaborators: *Dr Sarah Heilshorn[1], Dr Roisin M. Owens[2]*

[1]Stanford University Department of Material Science & Engineering

[2]Cambridge University Department of Chemical Engineering and Biotechnology

6.1 Abstract

The **blood brain barrier (BBB)** is formed by endothelial cells that constitute brain microcapillaries. The BBB regulates exchanges between the blood stream and the brain tissue. It ensures brain tissue homeostasis by providing nutrition and protection to neural cells. However, the BBB rejects most of the drugs for the treatment of neurological diseases out of the brain. 2D *in vitro* models of the BBB have been developed for drug screening, yet they usually lack cell-matrix interactions. It leads to a mismatch between and *in vitro* models and *in vivo* situation and wrong predictions in terms of drug efficiency and toxicity. Biomaterials have been developed to mimic BBB **extracellular matrix (ECM)** physico-chemical properties *in vitro* and improve BBB endothelial cells with its surrounding environment. Here we review materials used over the past decade to mimic BBB microenvironment features. We highlight three main types of *in vitro* models based on substrate degradability and the related cell culture dimensionality it offers.

6.2 Introduction

The Blood Brain Barrier (BBB) is localized at the brain vascular ending. It is formed by endothelial cells that fold on themselves to create a 10 µm diameter lumen. The BBB is a highly selective barrier that regulates ionic and macromolecule exchanges between the blood stream and the brain tissue. Contrary to the peripheral vasculature, BBB endothelial cells are non-fenestrated and exhibit low pinocytic vesicle concentration. Specific transporters line cell membrane and allow the BBB to act as a *metabolic barrier*. As such, influx transporters provide

water-soluble molecules needed in abundance by the CNS 10-100 times faster than predicted from their physicochemical characteristics.[1] Efflux transporters both repel neurotoxic agents coming from the blood and clean the neural tissue by excluding waste molecules.[2] As such, P-Glycoprotein (P-Gp) is a drug-transporter predominantly localized on the apical side that reject out of hand most of the large drugs (>400 Da).

Apical junctional complexes bridge BBB cells to form a *physical barrier* the passive diffusion along the paracellular route. They are composed by tight-junctions (TJs) intermixed with adherens junctions. TJs, mainly Claudins and Occludins, close the gap between neighboring cells and regulate ionic and solute paracellular diffusion. They act as gated channels that select molecule diffusion based on their size and charge. TJ proteins are connected to the cell cytoskeleton through cytosolic plaques, which zona occludens (ZO) is a main component. Together with claudin proteins they are often used as BBB tightness markers. More details about the molecular composition and organization of BBB adherent junction complex may be found here.[3] The regulation of ion flow across barrier tissue is usually quantified by the trans-endothelial -epithelial electrical resistance (TEER) measurement. *In vivo* electrical impedance measurement was led for the first time in 1982 on a live frog. Two pairs of electrodes were introduced in an isolated brain capillary and the BBB TEER was estimated around 1900 Ωcm^2.(Crone, 1982). This value is a gold standard in the field of cerebral vascular biology and it is now well accepted that TEER value is a way to quantified *in vitro* barrier tissue integrity. Then *in vitro* BBB models using human cells exhibited TEER values until 5000 Ωcm^2.[4]

In the human brain, neural cells surround the BBB and provide structural support to the endothelial cells. Pericytes cover ~ 30% of the capillary wall and astrocytes end-feet enwrapped ~ 98% of the previous cell complex. Astrocytes and pericytes both strongly regulate BBB functions through the secretion of various mediators, which regulate transporters and TJ protein expression [5,6]. All together with neurons they form the neurovascular unit (NVU). [7–9]

6.3 The demand for *in vitro* models of the blood brain barrier

The presence of both transmembrane transporters and junctional complexes along the BBB endothelial cells makes difficult the delivery of active compounds within the brain tissue. In particular, the P-gp drug transporters reject most of the drugs out of BBB endothelial cells, which renders drug accumulation in a relevant therapeutic concentration challenging. For some neurological diseases such as epilepsy, a reinforcement of BBB metabolic barrier property through P-gp accumulation was even observed at the seizure area.[10]

A large number of central nervous system (CNS) diseases, including Alzheimer's and Parkinson's diseases, Amyotrophic lateral sclerosis and epilepsy, exhibit BBB dysfunctions, although the causal relationship is usually unclear. [11,12] On one hand, agents secreted by neural cells in pathological condition may impaired BBB functions. [13] As such, pro-inflammatory mediators secreted by astrocytes during inflammation increased BBB permeability and support leukocyte infiltration.[14] Matrix MetalloProteinases (MMPs) activated by pericytes during cerebral ischemia contributed to rapid and localized proteolytic degradation of the BBB TJs.[15] BBB disruption was induced by neural cells during neurodegenerative disease progression.[16] On the other hand, pathogenic agents circulating into the blood stream may induce BBB breakdown and the entrance of harmful components within brain tissue. As a result, a causal and temporal understanding of BBB impairment linked to neurological diseases may give rise to new therapeutic targets.

Nowadays, the two main models used to study the BBB are animal models and *in vitro* cell models. Animal models, mainly rodents, are still widely used in the field of drug testing. They offer to preserve native mammalian matrix complexity as well as brain tissue structure. However, both cellular and matrix composition differ across organisms which ends up in a mismatch between human and animal models. [17] As a result, animal models are poorly predictive of drug efficiency and toxicity for humans. Almost 80% of animal drugs candidates fail in clinical trial due to toxicity high level and/or low therapeutic efficiency.[17] *In vitro* cell models offer the possibility to culture cells from a human origin and mimic the human BBB in a controlled environment and performed drug screening and toxicology testing. However, both BBB cellular organization and matrix physico-chemical properties are challenging to reproduce on the bench. Progress made in microfabrication techniques and tissue engineering led to the development of

relevant platforms able to respect cell-cell and cell-matrix interactions. The design of an 'Ideal' biomimetic substrate for *in vitro* BBB cell culture requires a deep understanding of matrix structure and molecular composition.

6.4 Structure and molecular composition of the blood brain barrier matrix

Brain extracellular matrix (ECM) is composed of the brain parenchyma (17-20% of the brain tissue), the perineuronal network, which surrounds neurons, and the vascular basement membrane (BM). The latter separates microvascular endothelial cells from the underlying tissue. Four glycoprotein families compose the brain microvascular BM: collagen IV, laminins, nidogens and heparan sulfate proteoglycans (including perlecan and agrin). BM formation depends on the initial laminin network self-assembly. Then, nidogen and heparan form a bridge between laminin and collagen IV fibers to form a secondary network in which laminin is cross-shaped. [18] Brain microvascular BM consists of two entities that mainly differ by their laminin isoform biocomposition: laminin-111 and -211 mainly compose the *endothelial BM*, which separate endothelial cells and pericytes. Astrocytes secrete laminin-411 and -511 that compose the *parenchymal BM*, which surround brain vascular system (**Figure 6.1**).[2] Structure and composition of the BM is necessary for maintenance of BBB functions *in vivo*. [19–21]

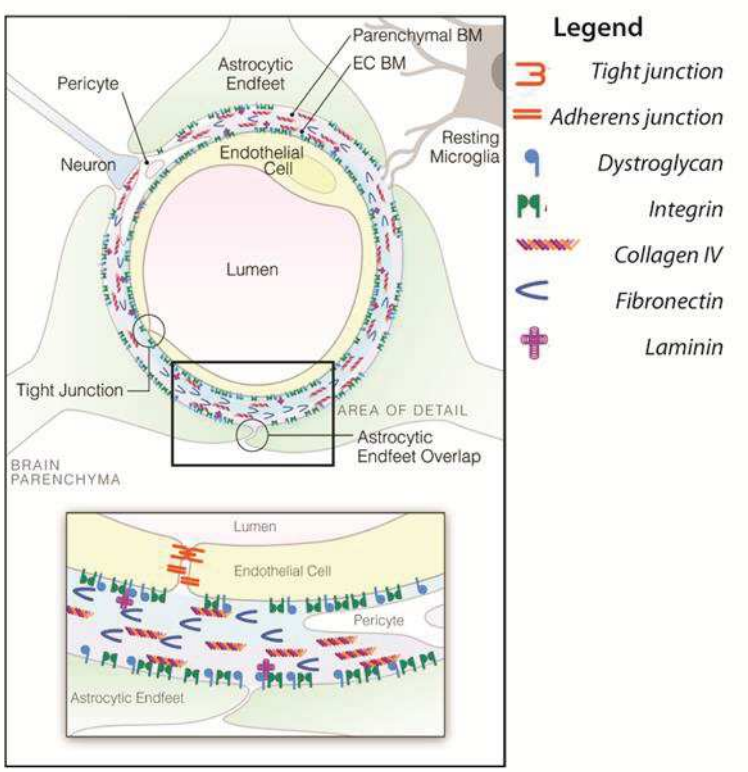

Figure 6.1: Schematic representation of the neurovascular unit. *Endothelial cells (ECs) form the blood brain barrier, in close contact with pericytes and astrocytic end-feet. The endothelial basal membrane (BM) separates ECs from pericytes and the parenchymal BM separate astrocytic end-feet from ECs and pericytes. ECs are bounded to the BMs through integrin-ECM interaction. Adapted from* [22]*.*

The critical aspect of BM components for *in vitro* BBB development has been shown using synthetic cell culture substrates modified by absorptive protein surface coating. As such, perlecan strongly improved hCMEC/D3 cell adhesion and TJ protein expression [22]. Agrin modulated TEER value in a cell origin-dependent way: it increased hCMEC/D3 TEER ~1.5 times compared to controls [22] while prevented iPSC-derived human brain microvascular endothelial cells (BMECs) barrier formation.[23] BMECs express all major basement membrane proteins when cultured on a porous membrane. It suggests the ability of these cells to recreate *in vitro*, part of their native microenvironment. Protein secretion was enhanced by co-culturing murine BMECs with pericytes.[24] The structural and biochemical critical aspects of BBB BMs components are summarized in **Table 6.1**.

Table 6.1: Overview of the blood brain barrier basal membrane composition: structural organization and interaction with microvascular endothelial cells [22]**.** *Endothelial cells (ECs), Pericytes (Ps) and Astrocytes (As)*

BM component	Matrix structural role	Impact on *in vitro* BBB functions	Cellular origin
Collagen IV	BM assembly and stabilization	Increases claudin-5 expression	ECs, Ps, As
Fibronectin (transient expression)	BM assembly	Affect barrier properties and integrity	ECs, Ps, As
Laminin 411, 511, 111, 211	BM assembly and stabilization	Cellular polarization Claudin-5 localization	ECs, Ps, As
Nidogen	BM structure		ECs
Agrin	Anchors ECs and As to BM	Increases Occludin expression and stabilize VE-cadherin, b-catenin and ZO-1	ECs, As
Perlecan	Cell-cell interaction	Increases occludin expression	ECs

Brain parenchyma is an ultra-soft and elastic tissue with an elastic modulus between 0.1-1 kPa.[28] However, there is little information about brain BM mechanical features, probably due to the difficulty in obtaining BM preparations free of adjacent interstitial connective tissue. BM from other tissue in the body revealed an elastic modulus in the range of MPa.[29] Vascular endothelial cells and in particular BBB endothelial cells pursue mechanical stimulation from their

surrounding microenvironment. As such, both shear stress, coming from the blood flow, and matrix elasticity generate mechanical cues and BBB endothelial cells respond to it through a mechanotransduction process. Then, BBB endothelial cells exposed *in vitro* to a physiologically relevant shear stress of 10 to 20 dyne.cm-2 were forming a tighter barrier by upregulation of TJ expression compare to the control.[30,31] Shear stress impact on *in vitro* BBB functions has been widely reviewed by [32]. However, matrix biomechanical impact on the BBB functions has been poorly investigated (**Figure 6.2**).

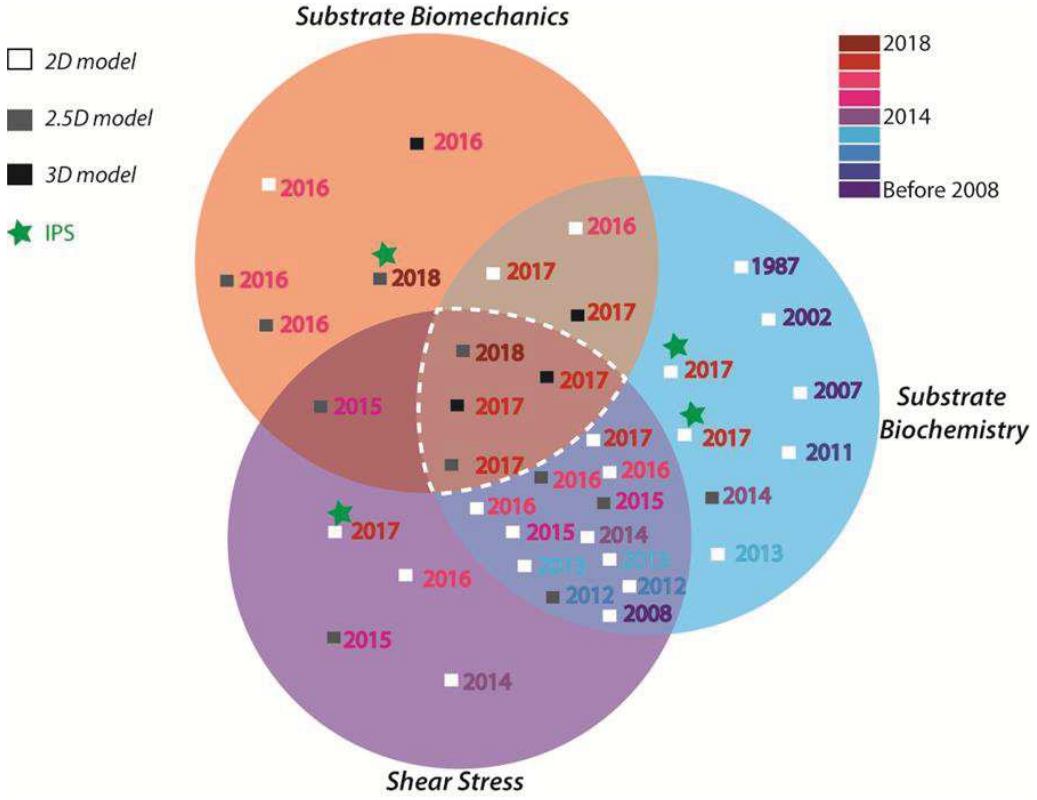

Figure 6.2: Selected History of *in vitro* BBB Models; *References:* [23–25,32–34,36,58–65,65–87].

6.5 2D blood brain barrier models

6.5.1 Porous, non-degradable material for 2D blood brain barrier models

2D models rely on the culture of cells on top of synthetic non-degradable substrates. Among them, PolyCarbonate (PC) or PolyEsther Terephthalate (PET) semi-permeable membrane are widely used to model the BBB *in vitro* for drug

screening. Transwell® systems offer the possibility to culture cells on each side of 10 μm thick porous membranes and establish multi-cell type culture configurations. As such, co- and tri- culture configurations were established to investigate cross-communication between endothelial and neural cells in healthy and disease models.[35] 5-days co-culture of human cerebellar microvascular endothelial cells (hCMEC/D3) with astrocytes or pericytes increased BBB TEER value by about 1.5 fold compare to the monoculture model.[36] The tri-culture of primary rodent brain microvessel endothelial cells (BMECs) with astrocytes and neurons significantly increased expression of BMECs P-gp and ZO-1 proteins compare to mono- or co-culture models.[37] Transporters secretion by human iPS-ECs increased by co-culturing all-human primary astrocytes, pericytes and iPS-derived neural stem cells (NSC) at the bottom of the well.[38]

The 'direct contact' co-culture configuration where endothelial cells are cultured on top of astrocytes monolayer has shown to BBB permeability compared to the conventional configuration. [39,40]

Pore diameter of Transwell® usually varies from 0.4 μm to 8 μm, which is adapted for the diffusion of proximal soluble growth factors between cells cultured on either side of the filter.[41] Astrocytes cultured on the basal side of the membrane were able to partly migrate across the pores when diameter exceeds 3 μm. They established cell-cell contact with the apical EC monolayer.[42] However large pores also promote the risk of endothelial cell migration across the membrane leading to a non-physiological double cell layer formation. This issue was overcome by adopting a 'dry-bottom' cell seeding configuration.[42]

Semi-permeable membranes have also been integrated into microfluidic platforms to evaluate shear stress impact on BBB functions. The membrane makes the physical separation between two channels in which culture media and the flow rate are controlled independently.[43]. The use of traditional semi-permeable membrane allows comparison with conventional transwell models.[44] Then, by applying a shear stress of 0.15 dyne.cm^{-2} on hCMEC/D3 monolayer, the TEER of *in vitro* BBB increased by ~1.5 folds compared to the static device.[45] Collagen gel with astrocytes embedded can be used to fill the lower channel of the device [46]. In some models, ECs line all or part of the vascular microchannel instead of covering only the filter, adding a 3D spatial configuration to the capillary-like structure.

PDMS-based devices, which integrate photolithography design of porous substrates for ECs culture are an alternative to the use of porous membranes and bring the possibility to include curvature to the capillary-like structure[47].

Substrate porosity is important to mimic the tortuous shape of the BM. Partial track etching technique is traditionally used to generate pores for semi-permeable membrane. However, this technique proposes random pore location with a low pore density (7% maximum). Microfabrication techniques were used to design pores with improved regularity and higher density into a range of materials, including silicon or resin-based membrane (**Figure 6.3, Table 6.2**). As such, 0.5 µm thick silicon substrates reached 20 % to 50 % porosity using electron beam photolithography.[48] SU-8 resin (elastic modulus GPa[49]) based ultra-porous microtubule has been designed using two-photon lithography.[50] Murine brain-derived EC.3 (bEnd.3) in co-culture with U87 glioblastoma cells on top of these 10 µm diameter microtubules decreased EC permeability to dextran.

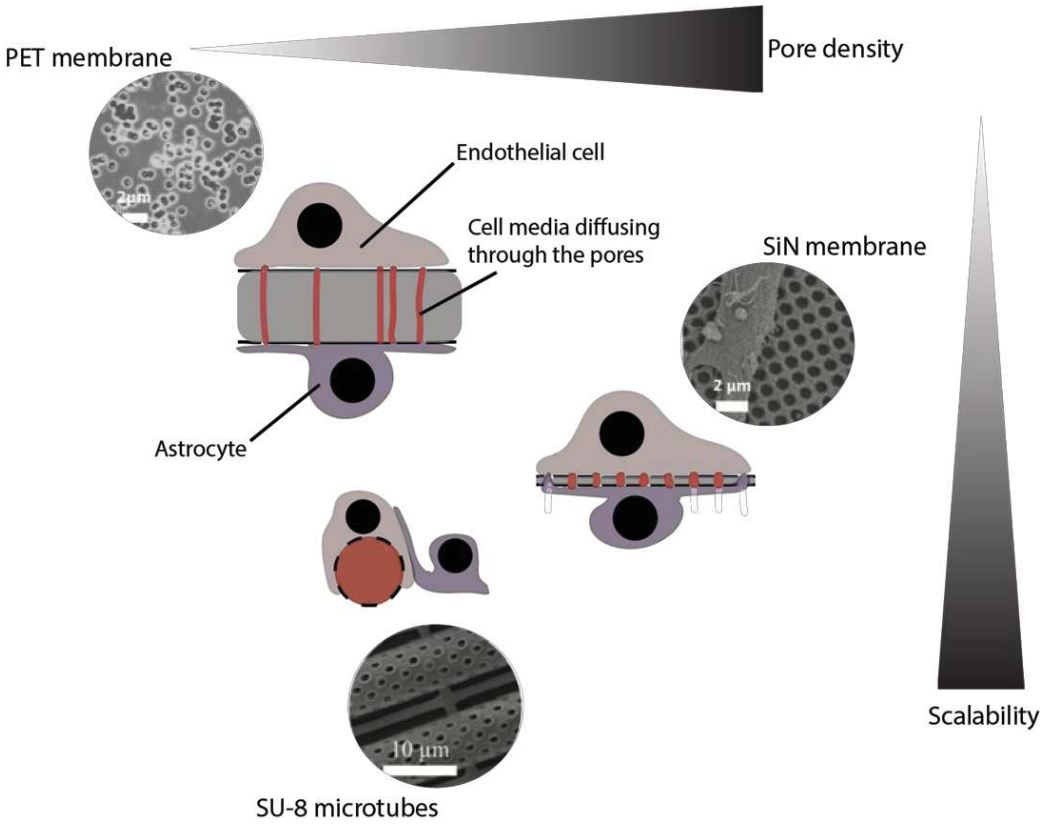

Figure 6.3: Porous non degradable substrate for 2D BBB models. ***a)*** *SEM images of a 0.4µm pore diameter PET semi-permeable membrane (left) and the associated cell scheme* ***b)*** *SEM image of bioinspired microcapillaries made of SU-8 using two-photon lithography technique to design 1µm pores.* ***c)*** *SEM image of*

an SiN porated membrane with a pore size of 0.6µm. The image illustrates astrocyte extensions projecting through the pores. Adapted from [44,46]*.*

Table 6.2: Porous non degradable substrates for 2D BBB cell culture. n.d means 'no data'.

Material	PET	SU-8	SiN
Thickness (µm)	10	n.d.	0.5
Curvature	No	Yes	No
Pore size (µm)	0.4 - 3.0	1	0.27 – 0.7
Pore density	15% - 7%	n.d	50% - 20%
Pore creation technique	Partial track etching	Two photon lithography	Electron beam photolithography

Most of these substrates exhibit a high elastic modulus including glass substrate (GPa) and (MPa), which is much higher than biological tissues (0.1-500 kPa). The Young's modulus of porous PET membranes is about 180 MPa [51], which is 3 orders of magnitude higher than brain tissue (kPa). However, a recent study revealed substrate pore density and diameter as key parameters to regulate mechanical sensing of the substrate by endothelial cells [52]. By decreasing the pore size and increasing pore density, ECs adopt a similar behavior to cells cultured on a soft substrate of kPa range in terms of number of focal adhesions (FAs) and TJ expression (**Figure 6.4**). The staining of cell FA over pores, lead to the hypothesis that ECs, when cultured on top of a disrupted surface, are able to generate ECM fibrils that span the pores and overcome contact area confinement. The close proximity of pores should result in many cell-matrix interactions occurring over open pore region leading to more physiological sensing of ECM stiffness. These observations are in accordance with previous papers, which noticed that murine

BMECs cultured on top of a 0.4 μm Transwell membrane exhibited the highest TEER value in comparison with 1, 3 and 8 μm membranes [53].

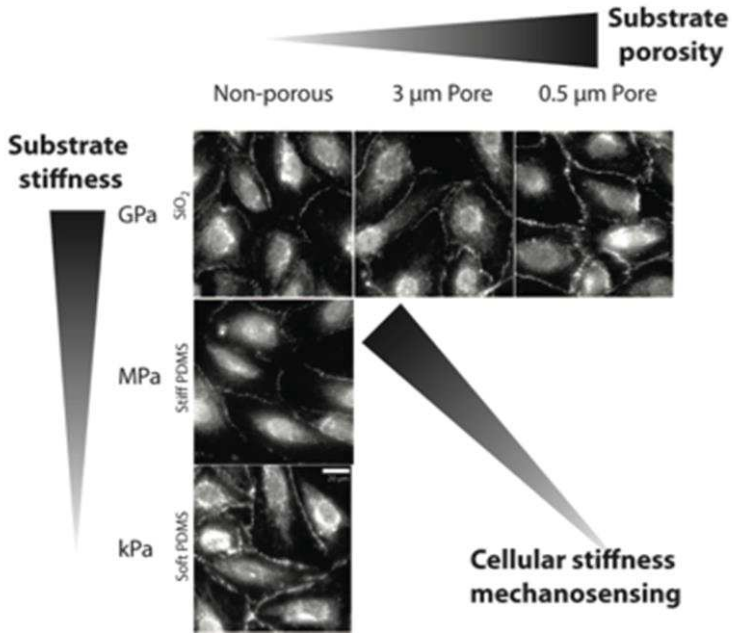

Figure 6.4: Representative image of ZO-1 tight junction proteins after 4 days of culture on nonporous, 3.0 and 0.5 μm pore diameter SiO_2 membranes, 2 MPa (stiff) and 5 kPa (soft) PDMS substrate. Adapted from [48].

These recent studies highlight the ability of matrix stiffness to modulate endothelial barrier permeability through mechanotransduction signaling, suggesting the importance in including this parameter in *in vitro* BBB tissue modeling. In the next sections, we will present new materials developed in the past 5 years with improved physical properties to approach cell-matrix interactions found *in vivo*.

6.5.2 Matrix modeling as an important feature for vascular function

As more generally for ECM, the brain BM corresponds to a fibrous network of entangled proteins that contains specific peptide sequences, which interact with cellular integrin's. It makes the matrix an adhesive substrate for cell attachment and migration while providing cells with topographic, elastic and structural cues. The brain BM exhibits a thickness that varies from 20 to 200 nm, which retains soluble factors secreted by surrounding astrocytes and pericytes, such as transforming growth factor-b (TGF-b) and Wnt, and generates diffusion gradients.[26,27] These

soluble factors are progressively delivered to vascular endothelial cells during matrix remodeling.

BBB dysfunctions were linked to changes in ECM mechanical properties that might be due to an extensive matrix remodeling.[10,33,34] It suggests the importance of cell-matrix remodeling and matrix physical properties to maintain BBB integrity. Following these observations we have chosen to classify BBB *in vitro* models based on matrix remodeling property and cell culture dimension. We will first present 2D cell model of BBB growing on flat stiff substrates. Brain endothelial cells individually embedded into a degradable biomaterial gave rise to 3D cell model where cells receive matrix cues in a 3D configuration. As an intermediate configuration, 2.5D cell model are made of degradable matrix are lined by a monolayer of brain ECs.

Brain microvascular endothelium receives information from the surrounding environment via bioactive soluble mediators and mechanical forces through cell–cell and cell-matrix interactions. Contrary to biochemical cues and shear stress, which have been extensively integrated as key parameters to regulate *in vitro* BBB integrity and functions, the participation of ECM biomechanical cues, including substrate stiffness, have been under-investigated in the field of BBB modelling (**Figure 6.2**). However, in cellular microenvironments that may be locally saturated by soluble factors, cells receive key information coming from the surrounding matrix through mechanical transmission from the matrix into the cells. Indeed, local ECM physical properties changes due to an extensive matrix remodeling have been suggested as one of the key parameters implied in BBB dysfunction [10,33,34].

The field of biological mechanosensing suggests that cells are able to sense and react to mechanical stimulation coming from their surrounding environment through actin stress fiber (SF) mechanotransduction. SFs are actin microfilaments bundles assembled through actin-myosin interactions to form an organized intracellular network. Some SF ends, mainly ventral SFs, are connected to focal adhesions (FAs) by proteins such as zyxin and vinculin. FA are protein complexes that form anchorage points between the cell and the surrounding matrix and hence enables mechanical forces to be transmitted into and out of the cytoskeleton of the cell. This force transmission has been shown to impact SF reinforcement, cell reorientation and to be critical for many cellular functions including

morphological stability, adhesion and motility [54,55]. Pulmonary ECs grown on three different grades of stiffness -very low (0.55 kPa), physiologically relevant (8.6 kPa), and very high (42 kPa) show an increase in stress fiber formation going hand in hand with increasing substrate stiffness [56,57]. The role of mechanical stimuli from the ECM to which cells attach, is gaining more interest with respect to the regulation of EC barrier properties. VE-cadherin seems to be part of an activated downstream mechanotransduction signals generated by substrate stiffness able to regulate FAs size, number and remodeling [58] directly implicated in cell contractility and gap formation in between adjacent cells. Increase in stress fiber density might produce a tensile force in the cell, able to pull proteins of the Adherens junction complex away from the cell surface inward toward the center of the cells. In contrast, soft substrates (kPa) were observed to be correlated to enhance in endothelial barrier properties. It may be due to a recruitment of VE-cadherins at junctional complexes and a shift from actin stress fibers to cortical actin that reduces tensile forces at VE-cadherin [59]. These observations are in accordance with a recent study suggesting a role of gap junction-mediated cell–cell interaction in the regulation of EC stiffness [60]**.** The molecular mechanism underlying barrier function modulation by substrate stiffness is excellently reviewed by [61]**.**

6.6 Degradable biomaterials as a matrix design element for 2.5D blood brain barrier models

6.6.1 Decellularized *in vitro*-secreted extracellular matrix

Given the complexity of ECM composition and structure combined with our incomplete understanding, designing a biomimetic material that fully mimics the architecture of the native tissue ECM are not currently possible. Decellularized ECM has already been shown to provide valuable insights for tissue engineering as it retains a native-like structure and composition. It is mainly obtained from an extracted tissue from which cellular components have been removed without impairing the microstructure of the matrix. Sliced brain sections can be decellularized, and this decellularized ECM can be used as the substrate for the three-dimensional (3D) culture of neural stem cells (NSCs) [91]. However, due to the very small diameter of the BBB structure and the complexity of cellular

organization, decellularization of the tissue by removing all cellular components is currently technically not possible. Thus, protocols to isolate decellularized ECM secreted by pericytes, astrocytes or endothelial cells *in vitro* have been developed [63]. The TEER of primary porcine brain endothelial cells was increased three-fold when the barrier was formed on pericyte-secreted ECM compared to endothelial-secreted ECM. A more complex model consisting of culturing each cell type a second time on a previously cell-secreted ECM for ECM remodeling and complexification enable them to reach more *in vivo* like ECM showing suprastucture organization (**Figure 6.5**). Pericytes cultured on astrocytes-secreted ECM remodel the substrate to produce honeycomb-like structures containing fibronectin and collagen IV, which improved Claudin-5 expression by endothelial cells of about two-fold compare to the endothelial ECM [63]. It should be noticed that this *in vitro* cell-secreted ECM employed in this study do not reflect the normal BM as they express high amounts of fibronectin, which is not an integral component of the normal endothelial basement membrane [92]. Therefore, improvements in BBB function do not necessarily correlate with the *in vivo* situation.

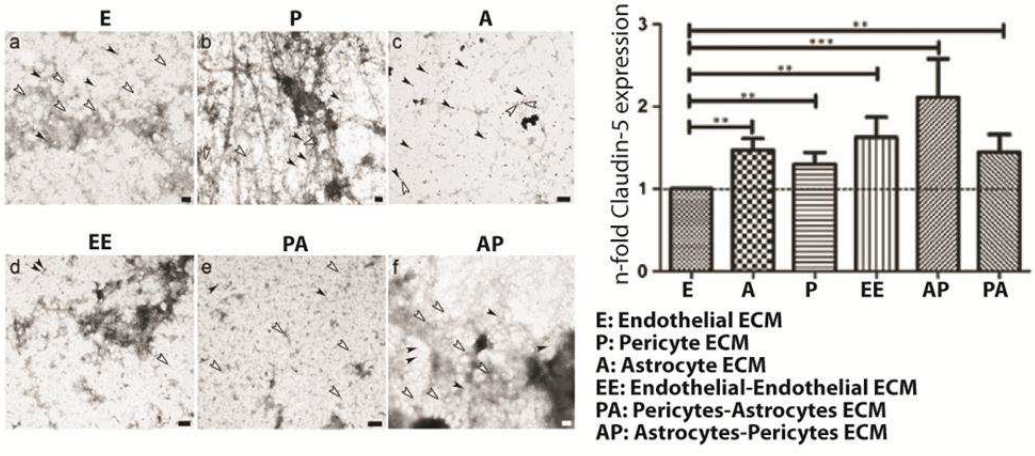

Figure 6.5: Decellularized cell secreted-ECM *in vitro*. *a)* *In vivo-like matrix produced by porcine astrocytes and pericytes on stiff (GPa) non-porous substrate* ***b)*** *and densitometrical expression of Claudin-5 TJ protein by porcine brain capillary endothelial cells. Black arrowheads show antibodies against Collagen IV and white arrowheads show antibodies against fibronectin.* [59]**.**

6.6.2 Electropsun membranes

Traditional semi-permeable membranes usually lack the ability to mimic fibrous architecture of BBB native matrices, which influence tissue structure and functions. Electrospinning enables nanofibers production of synthetic or natural biopolymers. The technique consists in forcing a polymeric solution to go through an electrostatic field to generate fibrous networks. Fiber diameter varies from few nanometers to more than a micrometer. Electrospinning is a versatile and relatively inexpensive approach to create scaffolds that approach native ECM architecture.

Human brain microvessel endothelial cells (HBMECs) cultured for 21 days on a Gelatin-based electrospun scaffold, so called 'biopaper', formed a less permeable barrier compare to the ones cultured on PET membrane (Figure 6.6a).[67] HBMECs have also been co-culture with primary human astrocytes during 28 days on this 4.5 μm thick 'biopaper' showing an upregulation of gene expression associated with extracellular matrix and TJs compare to PET membranes.[93] Fiber diameter and degradability is tuned by the amount of gelatin and the ratio gelatin/crosslinker agent. *Also gelatin fibers can be tuned by* [94]**.**

Synthetic polymer poly(lactic-co-glycolic) acid (PLGA) were electrospun to form cell-degradable nanofibrous meshes. Endothelial cells derived from human iPSC were co-cultured with astrocytes to form an *in vitro* BBB model (Figure 6.6c).[95]

Co-polymer electrospun scaffold for brain ECs in tri-culture with pericyte and astrocytes were fabricated using polycaprolactone (PCL) mix with polyethylene glycol (PEG) to increase cell-degradation profile (Figure 6.6b).[96] This 5.8 μm thick fibrous membrane proposes fiber architecture and pore structure tunability. PCL presents mechanical support to wound healing [97,98], however it shows a low cell-degradation profile[99], poor brain ECs growth and low coating molecule adhesion.[96]

These scaffolds replaced the traditional PET membrane in transwells to culture BBB endothelial cells (**Figure 6.6**) and provided superior porosity and cell remodeling. These new transwells are compatible with traditional barrier tissue characterization tools which makes easier the comparison with non-degradable semi-permeable membrane.

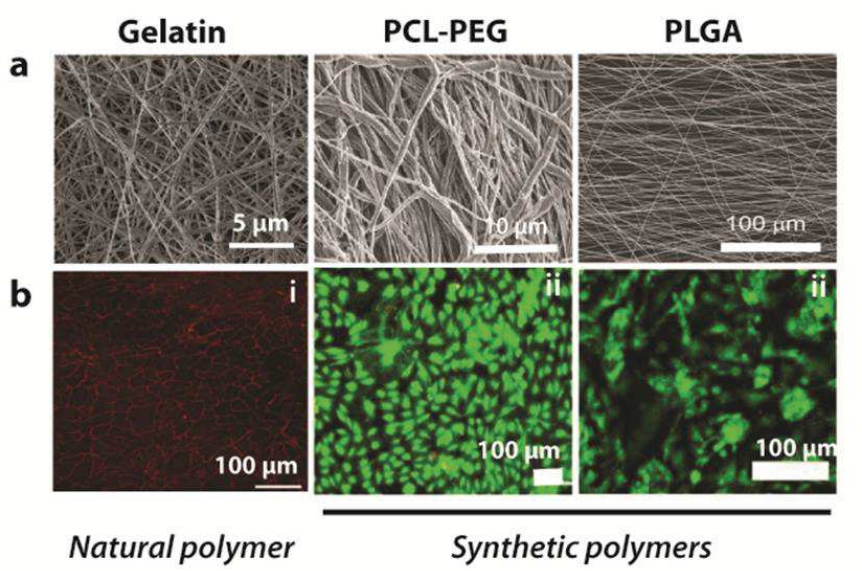

Figure 6.6: Electropsun membrane for BBB 2.5D model. ***a)*** *SEM images of electrospun membrane using natural or synthetic polymers as labelled and* ***b)*** *associated PECAM-1 (red staining) (i) or Live/Dead (green staining) (ii) images of human brain endothelial cells cultured on the respective substrates. Adapted from* [63,95,96].

6.6.3 Hydrogels

One of the major advancements in the engineering of ECM based biomaterials is the possibility to form ECM hydrogels. Hydrogels are composed by polymers hydrated with more than 30% (v/w) of water content. They are usually made of natural (alginate, collagen, elastin or HA) or synthetic (PEG) polymers, which maintain their structural integrity through crosslinking between the components. Hydrogels are compatible with a variety of new fabrication technologies including 3D printing, micropatterning and electrospinning.

Hydrogel membranes have been fabricated using using synthetic or natural polymers to replace the traditional semi-permeable membrane in a transwell model. As such, PEG solution was combined with a zinc oxide to form a porated hydrogels for BBB modeling.[100] Tri-peptide sequences Arg-Gly-Asp (RGD), from fibronectin, were integrated within PEG polymer to make it bioactive. Compared to PET membrane, this hydrogel membrane offers two-fold decreased pore diameter and one order of magnitude increased pore density. The Young's Modulus is ~100 kPa and can be tuned by changing PEG molecular weights without impacting either pore diameter or membrane thickness. Human umbilical vascular ECs (HUVECs)

cultured on the membrane exhibited less cell spread and increased VE-cadherin width. When co-cultured with pericytes, HUVECs allowed a functional vascular monolayer to be formed.[51,100]

Collagen gel vitrification technique was used to produce ~100 μm thin hydrogel membrane.[101] Polymerized collagen was combined with Matrigel using transglutaminase to modulate EC attachment and growth. Alginate was used as a porosity agent to tune pore diameter from 250nm to 700nm within the membrane. Membrane Young's Modulus was tuned by changing the ratio between collagen and Matrigel and allowed to vary from 429 kPa to 660 kPa. Considering the fact that Matrigel is mainly composed of globular proteins, the change in stiffness is likely due to the reduction in fibrous collagen, rendering the membrane more compliant [101].

Figure 6.7 and **Table 6.3** propose to recapitulate previously described new materials used to replace the traditional semi-permeable membrane in a Transwell configuration.

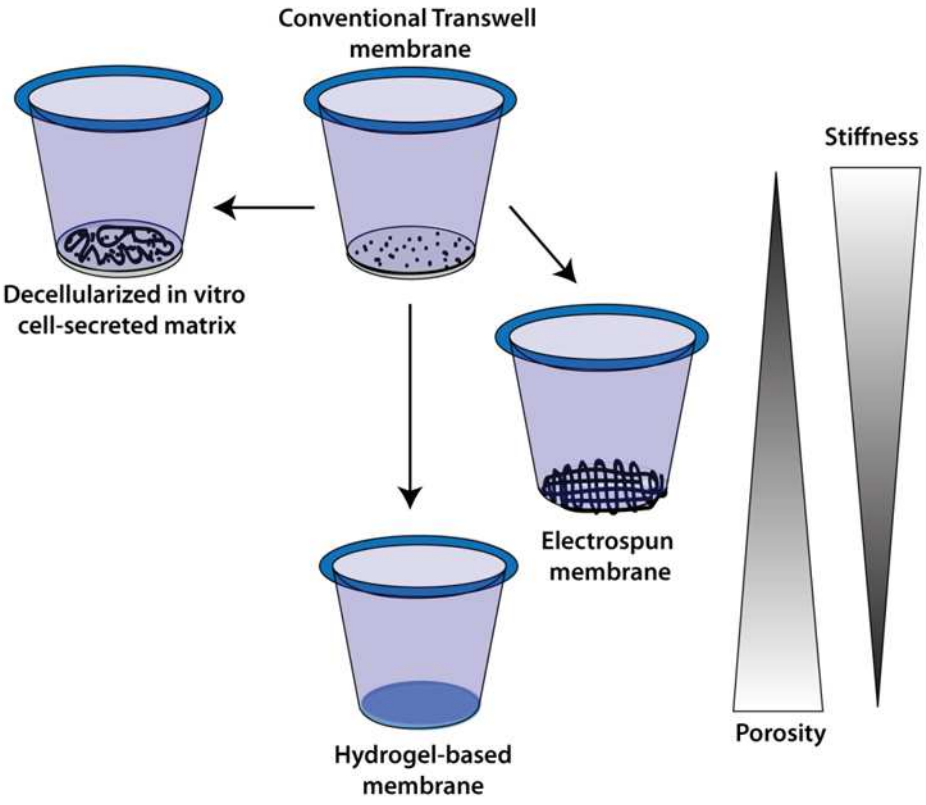

Figure 6.7: Strategies to move from 2D to 2.5D cell culture systems in a Transwell configuration.

Table 6.3: Biomaterials used to replace porous membrane for 2.5D model [63,95–97] n.d. means 'no data'.

	Conventional membrane	Electrospun membranes			Hydrogel membranes	
Biomaterial/ origin	PET/ synthetic	Gelatin 15%/ natural	96%PCL-4%PEG/ synthetic	PLGA 100%/ synthetic	Collagen-Matrigel/ natural	PEG-RGD/ synthetic
Thickness (µm)	10	4.5	5.8	30	20	9.5-18.8
Pore size (µm)	0.4	n.d.	0.6	n.d.	0.25-0.7	0.2
Fiber diameter (µm)	None	0.2	0.5	0.8	n.d.	n.d.
Stiffness	180 MPa	3.4 MPa	n.d.	53.8 MPa	660 kPa	54.7 kPa-96.8 kPa
Physical tunability	✖	✓	✓	✓	✓	✓

Organ-on-a-chip systems propose the culture of cell within micron-size chambers that are continuously perfused.[102] In some models of the blood brain barrier, brain ECs line the wall of the chamber that is made of collagen type I hydrogel. Collagen low Young's Modulus (kPa) and inherent GFOGER sequences make it one of the favorite biomaterials candidates to mimic ECM in BBB-on-a-chip systems.[103] hiPSC-derived brain microvascular ECs barrier was improved by adding Arg-Glu-Asp-Val (REDV) from fibronectin and Ile-Lys-Val-Ala-Val (IKVAV) from laminin.[104]

Lumen design for BBB-on-a-chip devices is made using both photolithography and phase guide technique to separate liquid from the hydrogel. Then, brain ECs are cultured on the wall of the chamber, which is composed by an assembly of several materials including collagen gel, PDMS and glass (**Figure 6.8a**). [76,105] As an alternative strategy, lumens were formed inside the hydrogel using viscous fingering technique or removing of needles. In that respect, cells seeded into the lumen sense the same surrounding material (**Figure 6.8b**) [74,75]. Channels have been designed within a collagen gel using gold nanorods and near-infrared laser beam to thermally denaturized the

protein. bEnd.3 cells were encapsulated into the collagen and allowed to migrate and elongate in tubular structure to form *in vitro* BBB vessels. Channel diameter was tuned from 9 to 180 μm by changing laser power and writing speed.[106]

Multicomponent hydrogels were fabricated to mimic physico-chemical properties of the native tissue. As such, HBMEC were cultured on top of a collagen gel mixed with hyaluronic acid and Matrigel. The latter was necessary to induce barrier formation. [107] Matrigel is a tumor-derived ECM cocktail composed by ~60% laminin, ~30% collagen IV, ~8% entactin and proteoglycans with additional GFs). It differs from the native basement membrane by the lack of matrix microstructure.

Brain parenchymal cells were embedded within organ-on-a-chip hydrogel to create a NVU-on-a-chip system. Astrocytes embedded into collagen hydrogel were allowed to 3D spread. Contrary to 2D configuration, astrocytes cultured in 3D models kept a quiescent phenotype closer to the *in vivo* situation.[107] It also enabled astrocytes and pericytes to remodel collagen and migrate close to the brain ECs to reform an NVU-like cellular organization. The presence of pericyte surrounding ECs vessel-like structure promoted ECs polarization through an increase number of ECs basal focal adhesions (FAs). [90] It also increased secretion of BM component such as collagen type IV in between ECs and both astrocytes and pericytes. [74,90]

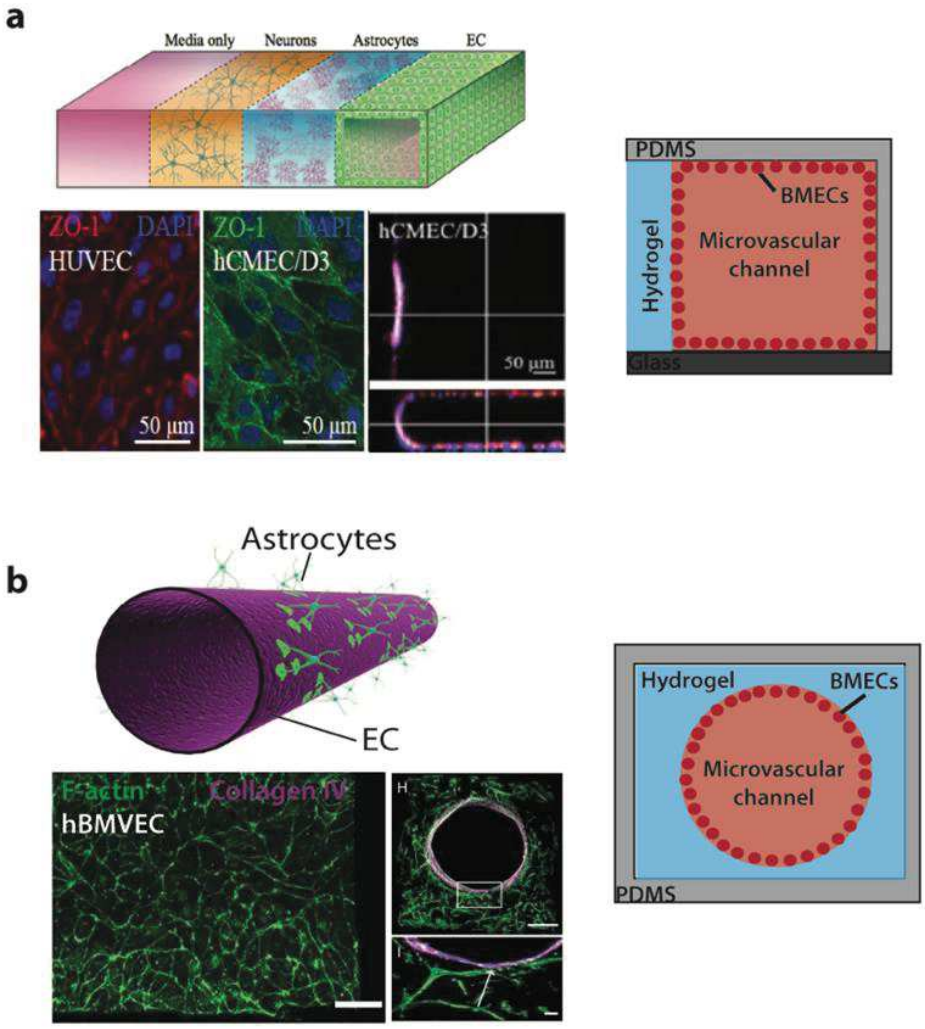

Figure 6.8: BBB-on-chips strategies. Adapted from [70,101]

Organ-on-a-chip systems are particularly adapted to mimic *in vivo*-like mechanical cues coming from the surrounding environment, including cell curvature and laminar flow. Then, vessel-like network containing bifurcations highlighted local changes in shear stress at the deviation point. ECs physiology was particularly fragile in this area, showing impairments in barrier integrity.[108] Tubular shape structure made into viscoelastic hydrogels allowed the introduction of a physiological cyclic stretch varying from 0% to 8% as a mechanical stress regulating hCMEC/D3 cell barrier functions [80]. Peripheral ECs stress fiber and FA rearrangements were associated to the mechanical strain of pulsatile flow. [109] This parameter was included into several vessel-on-a-chip systems [110].

6.7 3D microvascular blood brain barrier models

In the first stage of BBB development, endothelial progenitor cells invade the embryonic endothelium. This communication with neural cells triggers the BBB sprouting and barrier function development.[111] The study of EC behavior in constricted environments is particularly relevant to underline parameters linked to cell invasion mechanism and vascular network formation. In 2D and 2.5D configurations, the contact between cells and the matrix only happens at the basal side, which forces cells to polarize. 3D cell models offer the possibility to cultured brain ECs into the matrix, so cells spread and establish FAs in a 3D configuration.[112]

6.7.1 General information about endothelial cell sprouting

ECs embedded into a matrix-like hydrogel and activated by angiogenic growth factors such as Vascular Endothelial Growth Factor (VEGF), were allowed to migrate and sprout.[113] Sprout formation corresponds to branch expansion from the main vessel. They are composed by tip cells that lead the sprouting direction and stalk cells that follow tip cells and multiply to form the vessel. Tip cells define the path of neovascularization while the following stalk cells establish a nascent lumen by remodeling the matrix [114]. The issue of how stalk cells support sprout elongation is still unclear, however, a general assumption is that a sprout elongates as the stalk cells proliferate. The all structure is pulled by tip cells. Maturing sprouts fuse with neighboring sprouts to form capillary loops. During sprouting, ECs remodel considerably the BM through mechanical and chemical interactions.

Matrix metalloproteinase proteins (MMPs) expression co-localize with cell lamellapodia. They might participate to EC sprouting by cleaving collagen fibers. However, due to a lack of suitable reagents it is not possible to precisely localize most of the MMPs within the tissues. It makes thus difficult the understanding of their role in ECM remodeling. An exception to this is for gelatinases MMP-2 and MMP-9 for which activity is detected *in vivo* using gelatin zymography. During a stroke, MMP-9 may be secreted by ECs, neurons and astrocytes to remodel brain ECM and facilitate migration of neuronal precursor cells toward the damaged area. [115] MMP-2 and MMP-9 were also implicated in many diseases of the central nervous system (CNS) including neuro-inflammations and epilepsy. They degraded BBB tight junctions, inducing capillary leakage and immune cells extravasation

into the brain tissue.[10] A recent study also revealed the contribution of MMP-2 and MMP-9 secreted by pericytes during ischemia in the BBB proteolytic degradation.[15]

ECM stiffness may govern capillary morphogenesis by increasing mechanical tension on cell adhesion receptors. [116] Collagen matrix deformation during the early stage of *in vitro* HMVECs sprouting was tracked using particle image velocimetry techniques. The study revealed a strong cell-matrix mechanical interaction occurring by a "pull" and "released" tip cell behavior. The "pull" behavior leads to collagen fiber reorientation along lamellipodium long-axis and a decrease in collagen fiber density in the frontal region. The inherent changes in matrix stiffness might facilitate cell migration throughout the matrix, while serve as 'contact guidance' for cell-migration.[117] Thanks to their viscoelastic property collagen fibers return to their original positions when they are released. Dynamic changes in fibrin matrix stiffness during HUVEC sprouting have been shown using active micro-rheology technique. Bulk mechanical properties changes were mainly attributed to the presence of co-cultured fibroblasts. Yet, HUVECs were also progressively stiffening the surrounding ECM by both applying traction forces and depositing matrix components.[118]

6.7.2 Biomaterials for blood brain barrier vasculogenesis

It exists several ways to induce brain ECs sprouting *in vitro*. One of the techniques consists in seeding cells on the lateral side of a matrix, which is isolated between two microfluidic channels.[85] As another strategy, ECs that line tubular shape of vessel-on-a-chip devices may form lateral sprouting into the hydrogel.[90] Endothelial cells have been cultured in synthetic and natural polymers to form *in vitro* BBB, such as fibrin, collagen and polyethylene glycol (PEG).

Fibrin is the major component of the provisional matrix on a blood clot which justifies its suitability for investigating vasculogenesis [119]. HUVECs were cultured into fibrin hydrogel and vessel formation was correlated with matrix elasticity and fibrin fiber density.[120] The mechanical interactions that occur when pericytes wrap around ECs might stabilize HUVECs capillaries while promoting vascular junctions and branches [121]. HUVECs co-cultured with both astrocytes and neurons

formed vascular system with barrier properties. The vascular/astrocytic overlap was improved by the addition in the fibrin hydrogel of a VEGF-A gradient.[66] Matrigel mixed with fibrin hydrogel promoted hCMEC vasculogenesis as well as neurite extension from neural stem cells (NSCs).[85] In that study, the presence of neurons and pericytes were required to prevent gel shrinkage over vascular development.[85]

Collagen type I is one of the major component in most of the tissues. However, its concentration in brain parenchyma is very low. Collagen fibrils self-assemble and crosslink at neutral pH to form a matrix for cell culture. Many fabrication parameters have been reported to influence fiber structure and gel mechanical strength, including collagen source, solubilization, concentration, polymerization temperature, pH and ionic strength [122]. The change in collagen concentration required to form the hydrogel is associated with a change in fibril density. For low collagen concentration forming more compliant matrices, we observed a sparse distribution of collagen fibrils with a low degree of entanglement and large mesh size. Increasing the collagen density increases the entanglement of fibrils, resulting in smaller mesh sizes of the gel. The increase in matrix fibril density is associated with a change in the ratio of proliferating cells compared to migrating cells. By increasing collagen fibril density to a critical value (2.7 mg/ml), hMVECs are no longer able to elongate and penetrate into the ECM to sprout [123]. Collagen gel alone or in combination with other materials, such as fibrin gels or Matrigel, was successfully employed within microfluidic devices to study microvascularization process. Collagen I hydrogels can be fabricated reliably with controlled microstructure depending on the utilized isolation and gelation protocols. By decreasing the gelation temperature of collagen hydrogels from the usual 37°C to 4°C, collagen fibers are longer and thicker (150 nm), which can be explained by a limitation in nucleation of new fibers in case of lower temperature (**Figure 6.9**). The decreased entropy promotes thickening and elongation of already existing fibers. The inclusion of Matrigel into the collagen gel pronounced these differences by providing collagen nucleation sites. The presence of collagen type IV from Matrigel, combined with fibronectin, laminin and perlecan support the self-assembly of collagen IV in a mesh-like network. By lowering the casting temperature of collagen I and Matrigel, interactions between collagen fibrils and the linkers is prolonged, promoting the formation of thicker and longer collagen fibers.

If the biochemical factors coming from the addition of Matrigel were more impacting hCMECs growth than hydrogel microstructure itself, the increase in fiber length and thickness to the Matrigel-contained hydrogel, promote the development of thick, lumenized ECs branches. Differences in fibers size likely contribute to enhance EC contractility and the transmission of mechanical force along the fiber among neighboring cells might provide contact guidance for vascular network development. This microstructure also improves the deposition of Collagen IV by hCMECs. Similar results are observed with HUVECs cells [77].

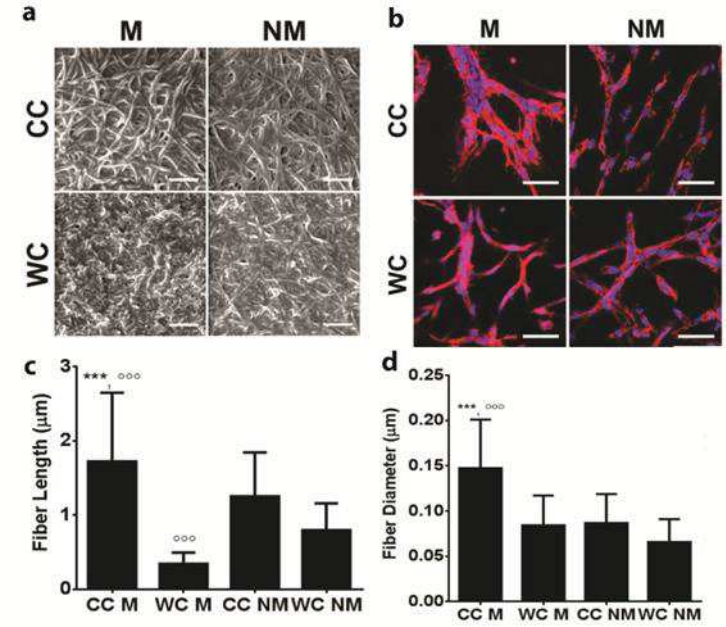

Figure 6.9: **Hydrogel composition and casting conditions impact collagen fibrillary structure**. ***a)*** *Scanning Electron Microscopy micrographs of cell-free hydrogels prepared by cold (CC) or warm (WC) casting in the presence (M) or absence (NM) of Matrigel. Scale bars are 50 µm and 1 µm, respectively. Image analysis of SEM micrographs indicated that collagen fiber.* ***b)*** *Confocal micrographs of hCMEC cultures suggest that hydrogel composition and casting conditions influence vasculogenic network assembly. Blue is DAPI and red is phalloidin. Scale bars are 50 µm.* ***c)*** *length and* ***d)*** *diameter increases with decreased casting temperature; effects were enhanced in Matrigel-containing hydrogels.* [74].

PEG: Synthetic PEG hydrogel containing MMP-degradable peptide and CRGDS peptide sequence for cell adhesion was used to seed human pluripotent stem cells-derived NPCs, ECs and MSCs for NVU tissue reconstitution [124].

6.7.3 3D pinting bioinks

A promising area for development of neurovascular unit model is their biofabrication through 3D printing, to produce a multicomponent scaffold combining different cell types. Bioprinting is defined as the process of patterning cell suspensions embedded within a biocompatible material with a hierarchically defined 3D spatial organization. Biofabrication of a tissue-engineered 3D NVU model utilizing hydrogel based bioinks with specific spatial distribution of the different cell types and combination of the normal and diseased NVU cellswill allow precise dissection of the contribution of each cell type to the disease-specific dysfunction. There are many different biopolymers that can be developed into bioink to form a hydrogel matrix for cells. These range from natural polysaccharides, which are either native constituents of the ECM or mimic the native ECM. Ideally the hydrogel will allow cells to secrete and deposit their own native ECM, thus potentially replicating the physiological role of the native tissue ECM. Soft bioinks, which reproduce mechanical properties of the brain ECM (around 1kPa) tend to print with lower resolution than those with higher yield stress and stiffness.

A common strategy to functionalize hydrogels for NVU-bioprinting purposes is to combine two biopolymers to produce a blended hydrogel-based bioink, with the advantageous properties of each polymer contributing to the favourable NVU properties required. Collagen-based hydrogels have been created: although collagen has an inherent GFOGER adhesion domain, collagen hydrogels typically lack the physical properties to be used as a bioink (slow gelation times). Collagen has been used to create mixed hydrogel-based bioinks with various other matrices such as agarose, gelatin, methacrylate, alginate and Matrigel, altering shear thinning properties to create an effective bioink for NVU cell culture. Detailed analyses of bioink composition and properties for NVU bioprinting are widely reviewed in [28].

6.8 Conclusion and future opportunities

Here, we reviewed physical properties of materials used to mimic BBB matrix *in vitro*. We took as a reference the widely used semi-permeable membrane, which offers a non- cell degradable stiff substrate (MPa) with limited pore diameter and density for 2D cell culture. As a consequence of the emergent field of

mechanotransduction, and subsequent consideration of substrate physical properties such as matrix stiffness, new materials have been developed with the aim to improve substrate physical property and to approach *in vivo* mechanical cues delivered from the matrix to the tissue. Hence, new materials exhibiting lower Young's Modulus, showing increases in pore density and with the possibility to be remodeled by surrounding cells, are required. The development of natural or synthetic hydrogels with tunable elasticity and cell-degradation rate has been suggested as the most promising biomaterials for soft tissue engineering. Hydrogels mechanical properties have been largely explored through organ-on-chip systems where endothelial cells are cultivated in monolayer lining a predesigned vascular channel. We have defined the culture on monolayer of endothelial cells on degradable substrate as a 2.5D cell culture configuration. A different approach consists of orienting endothelial cells growth into a 3D matrix where cells receive homogenous mechanical cues from the surrounding environment. These 3D models allow the study of BBB development from an angiogenesis perspective.

Brain tissue elasticity has been estimated to be around 0.1-1kPa, however it remains almost impossible to determine with precision the physical property of the BBB BM due to the lack of available protocols to isolate this nanometer scale ECM. Previous studies have suggested that cells were able to sense stiffness of the underlying substrate up to 20 microns deep thanks to a force propagation along ECM fibers. Considering the difference in protein composition between brain parenchyma and BM, the thickness of the BM (20-200 nm) and the close proximity of mural cells and astrocytic end-feet, which exhibit an elastic modulus around 20 kPa (Okamoto et al. 2017) to the vascular endothelial cells, we can't confirm that BBB ECs sense the stiffness of brain parenchyma. Using soft biomaterials allowing a close contact between astrocytes, pericytes and endothelial cells is likely the best way to reproduce the *in vivo* mechanical properties of the basement membrane.

Table 6.4 gives an overview of materials that have been used to model the BBB depending on the dimensionality of the model.

Table 6.4: Summary of new materials for BBB modeling and mechanical stimuli associated with investigate/improve cell-matrix interactions.

Cell model	Mechanical stimuli	Biomaterial	Stiffness range	Endotelial cell type	Reference
2D	Curvature	SU-8 resin	GPa	bEnd.3	[46]
2D	Porosity	SiN	GPa	bBMVEC	[45]
2D	Pulsatility Shear stress	Silicon	GPa	HBMECs	[122]
2.5D	Topography	Gelatin nanofibers	MPa	HBMECs	[64]
2.5D	Topography	PCL-PEG nanofibers	n.d.	TIME cells	[97]
2.5D	Topography	PLGA nanofibers	MPa	hiPSC-derived EC	[96]
2.5D	Topography	*In vitro* cell-secreted ECM	n.d.	Porcine brain ECs	[60]
2.5D	Topography Stiffness	PEG-RGD hydrogel	kPa	HUVECs	[97]
2.5D	Topography Stiffness	Collagen-Matrigel hydrogel	kPa	HUVECs	[48]
2.5D	Geometry Shear stress	Collagen	kPa	hBMVECs/hCMEC/D3/ bEnd.3	[70,72,76,101]
2.5D	Shear stress Cyclic strain	Collagen-Matrigel-HA hydrogel	kPa	hCMEC/D3	[77]
3D	Shear stress	Fibrin	kPa	HUVECs/ hBMECs	[62,81,117]
3D	Topography	Collagen	kPa	hCMECs	[74]
3D	Matrix degradability	PEG hydrogel	kPa	hPSC-derived ECs	[120]

Future perspectives: the use of conducting polymers for electrically active NVU tissue: *In vivo* and ex vivo analysis of status epilepticus (SE) impact on the NVU in a rat pilocarpine model revealed an induced spatiotemporal course in BBB leakage happening within hours following electrical seizures. Resulting BBB damage appears to be an important factor in triggering epileptogenesis–associated changes including degeneration of NVU cells [126]. Thus, there is an interest in understanding how brain endothelial cells react after current stimulation in particular concerning the transport function across the BBB. Recent interesting models relying on the 2D culture of b.End3 cells on a Transwell filter and spatially uniform direct current stimulation (DCS) adapted system revealed an oriented fluid and solute movement across the BBB associated with DCS [127]. As illustrated in that

review, biochemical and mechanical parameters are impacting BBB integrity and the development of new models supports this idea. Biocompatible conducting polymers for scaffolds preparation represent a new class of advanced materials combining ECM physical properties with electrical conductivity in the emerging field of bioelectronics. Among conductive polymers (CPs), poly(3,4-ethylenedioxythiophene) doped with poly(4-styrenesulfonate) (PEDOT:PSS) is one of the most promising for bioscaffold construction because of its dispersibility in polar solvents and high conductivity. Then, by combining PEDOT:PSS with PCL polymer we can design organic electronic porous scaffolds for stimulation of electro-responsive cells showing great potential for bone reconstruction [128]. Hydrogels made of PEDOT:PSS combined with polyurethane composites have been shown to support human NSC grow and enhance neurogenesis by electrical stimulations of the cells [129]. Enhanced biocompatibility of CPs by using biomolecules as dopants has leaded to the development of PEDOT:GAGs (glycosaminoglycans) films increasing the proliferation of neural cells compared to the conventional PEDOT:PSS-based substrate [130].

The use of PEDOT:PSS-based transistors, so called OECTs, allows the measurement of barrier tissue integrity over time with a great temporal resolution. Thanks to their ability to act as a convertor of ionic signals into electrical signaling, OECTs are shown as promising devices to interact with biological environment [131]. Integrated as porous 3D scaffolds or in planar configuration integrated into a microfluidic device, OECTs show a promising way to integrate micrometer transepithelial resistance measurement platforms into *in vitro* models [132–134].

6.9 References

1. Oldendorf, W. Brain uptake of radiolabeled amino acids, amines, and hexoses after arterial injection. *American Journal of Physiology-Legacy Content* **221,** 1629–1639 (1971).

2. Abbott, N. J., Patabendige, A. A. K., Dolman, D. E. M., Yusof, S. R. & Begley, D. J. Structure and function of the blood–brain barrier. *Neurobiology of Disease* **37,** 13–25 (2010).

3. Bauer, H.-C., Krizbai, I. A., Bauer, H. & Traweger, A. “You Shall Not Pass”—tight junctions of the blood brain barrier. *Frontiers in neuroscience* **8,** (2014).

4. Lauschke, K., Frederiksen, L. & Hall, V. J. Paving the Way Toward Complex Blood-Brain Barrier Models Using Pluripotent Stem Cells. *Stem Cells and Development* **26,** 857–874 (2017).

5. Armulik, A. *et al*. Pericytes regulate the blood–brain barrier. *Nature* **468,** 557–561 (2010).

6. Sweeney, M. D., Ayyadurai, S. & Zlokovic, B. V. Pericytes of the neurovascular unit: key functions and signaling pathways. *Nature Neuroscience* **19,** 771–783 (2016).

7. McConnell, H. L., Kersch, C. N., Woltjer, R. L. & Neuwelt, E. A. The Translational Significance of the Neurovascular Unit. *Journal of Biological Chemistry* **292,** 762–770 (2017).

8. Gastfriend, B. D., Palecek, S. P. & Shusta, E. V. Modeling the blood–brain barrier: Beyond the endothelial cells. *Current Opinion in Biomedical Engineering* **5,** 6–12 (2018).

9. Iadecola, C. The Neurovascular Unit Coming of Age: A Journey through Neurovascular Coupling in Health and Disease. *Neuron* **96,** 17–42 (2017).

10. Rempe, R. G. *et al*. Matrix Metalloproteinase-Mediated Blood-Brain Barrier Dysfunction in Epilepsy. *The Journal of Neuroscience* **38,** 4301–4315 (2018).

11. Modarres, H. P. *et al*. In vitro models and systems for evaluating the dynamics of drug delivery to the healthy and diseased brain. *Journal of Controlled Release* **273,** 108–130 (2018).

12. Cai, Z. *et al*. Role of Blood-Brain Barrier in Alzheimer’s Disease. *Journal of Alzheimer’s Disease* **63,** 1223–1234 (2018).

13. Kealy, J., Greene, C. & Campbell, M. Blood-brain barrier regulation in psychiatric disorders. *Neuroscience Letters* (2018). doi:10.1016/j.neulet.2018.06.033

14. Argaw, A. T. *et al*. Astrocyte-derived VEGF-A drives blood-brain barrier disruption in CNS inflammatory disease. *Journal of Clinical Investigation* **122,** 2454–2468 (2012).

15. Underly, R. G. *et al*. Pericytes as Inducers of Rapid, Matrix Metalloproteinase-9-Dependent Capillary Damage during Ischemia. *The Journal of Neuroscience* **37,** 129–140 (2017).

16. Giannoni, P. *et al*. The pericyte–glia interface at the blood–brain barrier. *Clinical Science* **132,** 361–374 (2018).

17. Bridging barriers: a comparative look at the blood–brain barrier across organisms. 14

18. Thomsen, M. S., Routhe, L. J. & Moos, T. The vascular basement membrane in the healthy and pathological brain. *Journal of Cerebral Blood Flow & Metabolism* **37,** 3300–3317 (2017).

19. Schöller, K. *et al*. Characterization of microvascular basal lamina damage and blood–brain barrier dysfunction following subarachnoid hemorrhage in rats. *Brain Research* **1142,** 237–246 (2007).

20. Yao, Y., Chen, Z.-L., Norris, E. H. & Strickland, S. Astrocytic laminin regulates pericyte differentiation and maintains blood brain barrier integrity. *Nature Communications* **5,** (2014).

21. Gautam, J., Zhang, X. & Yao, Y. The role of pericytic laminin in blood brain barrier integrity maintenance. *Scientific Reports* **6,** (2016).

22. Baeten, K. M. & Akassoglou, K. Extracellular matrix and matrix receptors in blood-brain barrier formation and stroke. *Developmental Neurobiology* **71,** 1018–1039 (2011).

23. Maherally, Z. *et al*. Real-time acquisition of transendothelial electrical resistance in an all-human, *in vitro* , 3-dimensional, blood–brain barrier model exemplifies tight-junction integrity. *The FASEB Journal* fj.201700162R (2017). doi:10.1096/fj.201700162R

24. Katt, M. E., Linville, R. M., Mayo, L. N., Xu, Z. S. & Searson, P. C. Functional brain-specific microvessels from iPSC-derived human brain microvascular endothelial cells: the role of matrix composition on monolayer formation. *Fluids and Barriers of the CNS* **15,** 7 (2018).

25. Thomsen, M. S., Birkelund, S., Burkhart, A., Stensballe, A. & Moos, T. Synthesis and deposition of basement membrane proteins by primary brain capillary endothelial cells in a murine model of the blood-brain barrier. *Journal of Neurochemistry* (2016). doi:10.1111/jnc.13747

26. Potjewyd, G., Moxon, S., Wang, T., Domingos, M. & Hooper, N. M. Tissue Engineering 3D Neurovascular Units: A Biomaterials and Bioprinting Perspective. *Trends in Biotechnology* (2018). doi:10.1016/j.tibtech.2018.01.003

27. Candiello, J. *et al*. Biomechanical properties of native basement membranes: Biomechanical properties of basement membranes. *FEBS Journal* **274,** 2897–2908 (2007).

28. Cucullo, L., Hossain, M., Puvenna, V., Marchi, N. & Janigro, D. The role of shear stress in Blood-Brain Barrier endothelial physiology. *BMC neuroscience* **12,** 1 (2011).

29. DeStefano, J. G., Xu, Z. S., Williams, A. J., Yimam, N. & Searson, P. C. Effect of shear stress on iPSC-derived human brain microvascular endothelial cells (dhBMECs). *Fluids and Barriers of the CNS* **14,** (2017).

30. Gray, K. M. & Stroka, K. M. Vascular endothelial cell mechanosensing: New insights gained from biomimetic microfluidic models. *Seminars in Cell & Developmental Biology* **71,** 106–117 (2017).

31. Takeshita, Y. *et al*. An in vitro blood–brain barrier model combining shear stress and endothelial cell/astrocyte co-culture. *Journal of Neuroscience Methods* **232,** 165–172 (2014).

32. Hatherell, K., Couraud, P.-O., Romero, I. A., Weksler, B. & Pilkington, G. J. Development of a three-dimensional, all-human in vitro model of the blood–brain barrier using mono-, co-, and tri-cultivation Transwell models. *Journal of Neuroscience Methods* **199,** 223–229 (2011).

33. Zobel, K., Hansen, U. & Galla, H.-J. Blood-brain barrier properties in vitro depend on composition and assembly of endogenous extracellular matrices. *Cell and Tissue Research* **365,** 233–245 (2016).

34. Adriani, G., Ma, D., Pavesi, A., Goh, E. L. K. & Kamm, R. D. Modeling the Blood-Brain Barrier in a 3D triple co-culture microfluidic system. in *2015 37th Annual International Conference of the IEEE Engineering in Medicine and Biology Society (EMBC)* 338–341 (IEEE, 2015).

35. Appelt-Menzel, A. *et al*. Establishment of a Human Blood-Brain Barrier Co-culture Model Mimicking the Neurovascular Unit Using Induced Pluri- and Multipotent Stem Cells. *Stem Cell Reports* **8,** 894–906 (2017).

36. Arthur, F. E., Shivers, R. R. & Bowman, P. D. Astrocyte-mediated induction of tight junctions in brain capillary endothelium: an efficient in vitro model. *Developmental Brain Research* **36,** 155–159 (1987).

37. Bang, S. *et al*. A Low Permeability Microfluidic Blood-Brain Barrier Platform with Direct Contact between Perfusable Vascular Network and Astrocytes. *Scientific Reports* **7,** (2017).

38. Bischel, L. L. *et al*. Electrospun gelatin biopapers as substrate for in vitro bilayer models of blood- brain barrier tissue. *Journal of Biomedical Materials Research Part A* **104,** 901–909 (2016).

39. Booth, R. & Kim, H. Characterization of a microfluidic in vitro model of the blood-brain barrier (μBBB). *Lab on a Chip* **12,** 1784 (2012).

40. Brown, J. A. *et al*. Recreating blood-brain barrier physiology and structure on chip: A novel neurovascular microfluidic bioreactor. *Biomicrofluidics* **9,** 054124 (2015).

41. Cho, H. *et al*. Three-Dimensional Blood-Brain Barrier Model for in vitro Studies of Neurovascular Pathology. *Scientific Reports* **5,** 15222 (2015).

42. Chou, C.-H., Sinden, J. D., Couraud, P.-O. & Modo, M. In Vitro Modeling of the Neurovascular Environment by Coculturing Adult Human Brain Endothelial Cells with Human Neural Stem Cells. *PLoS ONE* **9,** e106346 (2014).

43. Cucullo, L. *et al*. Immortalized human brain endothelial cells and flow-based vascular modeling: a marriage of convenience for rational neurovascular studies. *Journal of Cerebral Blood Flow & Metabolism* **28,** 312–328 (2008).

44. Griep, L. M. *et al*. BBB ON CHIP: microfluidic platform to mechanically and biochemically modulate blood-brain barrier function. *Biomedical Microdevices* **15,** 145–150 (2013).

45. Herland, A. *et al*. Distinct Contributions of Astrocytes and Pericytes to Neuroinflammation Identified in a 3D Human Blood-Brain Barrier on a Chip. *PLOS ONE* **11,** e0150360 (2016).

46. Kim, J. A. *et al*. Collagen-based brain microvasculature model in vitro using three-dimensional printed template. *Biomicrofluidics* **9,** 024115 (2015).

47. Koo, Y., Hawkins, B. T. & Yun, Y. Three-dimensional (3D) tetra-culture brain on chip platform for organophosphate toxicity screening. *Scientific Reports* **8,** (2018).

48. McCoy, M. G., Seo, B. R., Choi, S. & Fischbach, C. Collagen I hydrogel microstructure and composition conjointly regulate vascular network formation. *Acta Biomater* **44,** 200–208 (2016).

49. Megard, I. *et al*. A co-culture-based model of human blood–brain barrier: application to active transport of indinavir and in vivo–in vitro correlation. *Brain research* **927,** 153–167 (2002).

50. Nakagawa, S. *et al*. Pericytes from Brain Microvessels Strengthen the Barrier Integrity in Primary Cultures of Rat Brain Endothelial Cells. *Cellular and Molecular Neurobiology* **27,** 687–694 (2007).

51. Partyka, P. P. *et al*. Mechanical stress regulates transport in a compliant 3D model of the blood-brain barrier. *Biomaterials* **115,** 30–39 (2017).

52. Phan, D. T. *et al*. Blood–brain barrier-on-a-chip: Microphysiological systems that capture the complexity of the blood–central nervous system interface. *Experimental Biology and Medicine* **242,** 1669–1678 (2017).

53. Prabhakarpandian, B. *et al*. SyM-BBB: a microfluidic blood brain barrier model. *Lab on a Chip* **13,** 1093 (2013).

54. Shao, X. *et al*. Development of a blood-brain barrier model in a membrane-based microchip for characterization of drug permeability and cytotoxicity for drug screening. *Analytica Chimica Acta* **934,** 186–193 (2016).

55. Tao-Cheng, J.-H., Nagy, Z. & Brightman, M. W. Tight Junctions of Brain Endothelium in vitro Are Enhanced by Astroglia. 7

56. Uwamori, H., Higuchi, T., Arai, K. & Sudo, R. Integration of neurogenesis and angiogenesis models for constructing a neurovascular tissue. *Sci Rep* **7,** (2017).

57. Wang, J. D., Khafagy, E.-S., Khanafer, K., Takayama, S. & ElSayed, M. E. H. Organization of Endothelial Cells, Pericytes, and Astrocytes into a 3D Microfluidic *in Vitro* Model of the Blood–Brain Barrier. *Molecular Pharmaceutics* **13,** 895–906 (2016).

58. Wang, Y. I., Abaci, H. E. & Shuler, M. L. Microfluidic blood-brain barrier model provides in vivo-like barrier properties for drug permeability screening: Microfluidic BBB Model Mimics In Vivo Properties. *Biotechnology and Bioengineering* **114,** 184–194 (2017).

59. Xue, Q. *et al*. A Novel Brain Neurovascular Unit Model with Neurons, Astrocytes and Microvascular Endothelial Cells of Rat. *Int J Biol Sci* **9,** 174–189 (2013).

60. Yamamizu, K. *et al*. In Vitro Modeling of Blood-Brain Barrier with Human iPSC-Derived Endothelial Cells, Pericytes, Neurons, and Astrocytes via Notch Signaling. *Stem Cell Reports* **8,** 634–647 (2017).

61. Ye, M. *et al*. Brain microvascular endothelial cells resist elongation due to curvature and shear stress. *Scientific Reports* **4,** (2014).

62. Zheng, Y. *et al*. In vitro microvessels for the study of angiogenesis and thrombosis. *Proceedings of the National Academy of Sciences* **109,** 9342–9347 (2012).

63. Xu, H. *et al*. A dynamic in vivo-like organotypic blood-brain barrier model to probe metastatic brain tumors. *Scientific Reports* **6,** 36670 (2016).

64. Helms, H. C. *et al*. In vitro models of the blood-brain barrier: An overview of commonly used brain endothelial cell culture models and guidelines for their use. *Journal of Cerebral Blood Flow & Metabolism* **36,** 862–890 (2016).

65. Kulczar, C., Lubin, K. E., Lefebvre, S., Miller, D. W. & Knipp, G. T. Development of a direct contact astrocyte-human cerebral microvessel endothelial cells blood-brain barrier coculture model. *Journal of Pharmacy and Pharmacology* **69,** 1684–1696 (2017).

66. Eugenin, E. A., Clements, J. E., Zink, M. C. & Berman, J. W. Human Immunodeficiency Virus Infection of Human Astrocytes Disrupts Blood-Brain Barrier Integrity by a Gap Junction-Dependent Mechanism. *Journal of Neuroscience* **31,** 9456–9465 (2011).

67. Vandenhaute, E. *et al*. Adapting coculture in vitro models of the blood–brain barrier for use in cancer research: maintaining an appropriate endothelial monolayer for the assessment of transendothelial migration. *Laboratory Investigation* **96,** 588–598 (2016).

68. Achyuta, A. K. H. *et al*. A modular approach to create a neurovascular unit-on-a-chip. *Lab Chip* **13,** 542–553 (2013).

69. Kaisar, M. A. *et al*. New experimental models of the blood-brain barrier for CNS drug discovery. *Expert Opinion on Drug Discovery* **12,** 89–103 (2017).

70. Walter, F. R. *et al*. A versatile lab-on-a-chip tool for modeling biological barriers. *Sensors and Actuators B: Chemical* **222,** 1209–1219 (2016).

71. Sellgren, K. L., Hawkins, B. T. & Grego, S. An optically transparent membrane supports shear stress studies in a three-dimensional microfluidic neurovascular unit model. *Biomicrofluidics* **9,** 061102 (2015).

72. Deosarkar, S. P. *et al*. A Novel Dynamic Neonatal Blood-Brain Barrier on a Chip. *PLOS ONE* **10,** e0142725 (2015).

73. Ma, S. H., Lepak, L. A., Hussain, R. J., Shain, W. & Shuler, M. L. An endothelial and astrocyte co-culture model of the blood–brain barrier utilizing an ultra-thin, nanofabricated silicon nitride membrane. *Lab Chip* **5,** 74–85 (2005).

74. Lemma, E. D. *et al*. Mechanical Properties Tunability of Three-Dimensional Polymeric Structures in Two-Photon Lithography. *IEEE Transactions on Nanotechnology* **16,** 23–31 (2017).

75. Marino, A. *et al*. A 3D Real-Scale, Biomimetic, and Biohybrid Model of the Blood-Brain Barrier Fabricated through Two-Photon Lithography. *Small* 1702959 (2017). doi:10.1002/smll.201702959

76. Mondrinos, M. J., Yi, Y.-S., Wu, N.-K., Ding, X. & Huh, D. Native extracellular matrix-derived semipermeable, optically transparent, and inexpensive membrane inserts for microfluidic cell culture. *Lab on a Chip* **17,** 3146–3158 (2017).

77. Casillo, S. M., Peredo, A. P., Perry, S. J., Chung, H. H. & Gaborski, T. R. Membrane Pore Spacing Can Modulate Endothelial Cell–Substrate and Cell–Cell Interactions. *ACS Biomaterials Science & Engineering* **3,** 243–248 (2017).

78. Wuest, D. M., Wing, A. M. & Lee, K. H. Membrane configuration optimization for a murine in vitro blood–brain barrier model. *Journal of Neuroscience Methods* **212,** 211–221 (2013).

79. Buxboim, A., Rajagopal, K., Brown, A. E. X. & Discher, D. E. How deeply cells feel: methods for thin gels. *Journal of Physics: Condensed Matter* **22,** 194116 (2010).

80. Sen, S., Engler, A. J. & Discher, D. E. Matrix Strains Induced by Cells: Computing How Far Cells Can Feel. *Cellular and Molecular Bioengineering* **2,** 39–48 (2009).

81. Lepelletier, F.-X., Mann, D. M. A., Robinson, A. C., Pinteaux, E. & Boutin, H. Early changes in extracellular matrix in Alzheimer's disease. *Neuropathology and Applied Neurobiology* **43,** 167–182 (2017).

82. Liu, X. *et al*. Role of matrix metalloproteinase-2/9 (MMP2/9) in lead-induced changes in an *in vitro* blood-brain barrier model. *International Journal of Biological Sciences* **13,** 1351–1360 (2017).

83. Burridge, K. & Guilluy, C. Focal adhesions, stress fibers and mechanical tension. *Experimental Cell Research* **343,** 14–20 (2016).

84. Tojkander, S., Gateva, G. & Lappalainen, P. Actin stress fibers - assembly, dynamics and biological roles. *Journal of Cell Science* **125,** 1855–1864 (2012).

85. Birukova, A. A., Shah, A. S., Tian, Y., Moldobaeva, N. & Birukov, K. G. Dual role of vinculin in barrier-disruptive and barrier-enhancing endothelial cell responses. *Cellular Signalling* **28,** 541–551 (2016).

86. Birukova, A. A. *et al*. Endothelial barrier disruption and recovery is controlled by substrate stiffness. *Microvasc Res* **87,** 50–57 (2013).

87. Andresen Eguiluz, R. C., Kaylan, K. B., Underhill, G. H. & Leckband, D. E. Substrate stiffness and VE-cadherin mechano-transduction coordinate to regulate endothelial monolayer integrity. *Biomaterials* **140,** 45–57 (2017).

88. McRae, M. *et al*. Characterization of cell-cell junction changes associated with the formation of a strong endothelial barrier. *Tissue Barriers* e1405774 (2018). doi:10.1080/21688370.2017.1405774

89. Okamoto, T. *et al*. Gap junction-mediated regulation of endothelial cellular stiffness. *Scientific Reports* **7,** (2017).

90. Karki, P. & Birukova, A. A. Substrate stiffness-dependent exacerbation of endothelial permeability and inflammation: mechanisms and potential implications in ALI and PH (2017 Grover Conference Series). *Pulmonary Circulation* **8,** 204589401877304 (2018).

91. Hoshiba, T. *et al*. Decellularized Extracellular Matrix as an In Vitro Model to Study the Comprehensive Roles of the ECM in Stem Cell Differentiation. *Stem Cells Int* **2016,** (2016).

92. KRUM, J. M., MORE, N. S. & ROSENSTEIN, J. M. Brain Angiogenesis: Variations in Vascular Basement Membrane Glycoprotein lmmunoreactivity. 14

93. Gaston, J. D. *et al*. Gene Expression Changes in Long-Term In Vitro Human Blood-Brain Barrier Models and Their Dependence on a Transwell Scaffold Material. *Journal of Healthcare Engineering* **2017,** 1–10 (2017).

94. Topuz, F. & Uyar, T. Electrospinning of gelatin with tunable fiber morphology from round to flat/ribbon. *Materials Science and Engineering: C* **80,** 371–378 (2017).

95. Qi, D. *et al*. Establishment of a Human iPSC- and Nanofiber-Based Microphysiological Blood–Brain Barrier System. *ACS Applied Materials & Interfaces* (2018). doi:10.1021/acsami.8b03962

96. Pensabene, V., Crowder, S. W., Balikov, D. A., Lee, J. B. & Sung, H. J. Optimization of electrospun fibrous membranes for in vitro modeling of blood-brain barrier. in 125–128 (IEEE, 2016). doi:10.1109/EMBC.2016.7590656

97. Anjum, F. *et al*. Biocomposite nanofiber matrices to support ECM remodeling by human dermal progenitors and enhanced wound closure. *Scientific Reports* **7,** (2017).

98. Miguel, S., Ribeiro, M., Coutinho, P. & Correia, I. Electrospun Polycaprolactone/Aloe Vera_Chitosan Nanofibrous Asymmetric Membranes Aimed for Wound Healing Applications. *Polymers* **9,** 183 (2017).

99. Zhang, Y., Ouyang, H., Lim, C. T., Ramakrishna, S. & Huang, Z.-M. Electrospinning of gelatin fibers and gelatin/PCL composite fibrous scaffolds. *Journal of Biomedical Materials Research* **72B,** 156–165 (2005).

100. Pellowe, A. S., Lauridsen, H. M., Matta, R. & Gonzalez, A. L. Ultrathin Porated Elastic Hydrogels As a Biomimetic Basement Membrane for Dual Cell Culture. *Journal of Visualized Experiments* (2017). doi:10.3791/56384

101. Lauridsen, H. M. & Gonzalez, A. L. Biomimetic, ultrathin and elastic hydrogels regulate human neutrophil extravasation across endothelial-pericyte bilayers. *PLOS ONE* **12,** e0171386 (2017).

102. Bhatia, S. N. & Ingber, D. E. Microfluidic organs-on-chips. *Nature Biotechnology* **32,** 760–772 (2014).

103. van der Helm, M. W., van der Meer, A. D., Eijkel, J. C. T., van den Berg, A. & Segerink, L. I. Microfluidic organ-on-chip technology for blood-brain barrier research. *Tissue Barriers* **4,** e1142493 (2016).

104. Katt, M. E., Linville, R. M., Mayo, L. N., Xu, Z. S. & Searson, P. C. Functional brain-specific microvessels from iPSC-derived human brain microvascular endothelial cells: the role of matrix composition on monolayer formation. *Fluids and Barriers of the CNS* **15,** 7 (2018).

105. Adriani, G., Ma, D., Pavesi, A., Kamm, R. D. & Goh, E. L. K. A 3D neurovascular microfluidic model consisting of neurons, astrocytes and cerebral endothelial cells as a blood–brain barrier. *Lab Chip* **17,** 448–459 (2017).

106. Hribar, K. C. *et al*. Three-dimensional direct cell patterning in collagen hydrogels with near-infrared femtosecond laser. *Scientific Reports* **5,** (2015).

107. Placone, A. L. *et al*. Human astrocytes develop physiological morphology and remain quiescent in a novel 3D matrix. *Biomaterials* **42,** 134–143 (2015).

108. Zheng, Y., Chen, J. & López, J. A. Microvascular platforms for the study of platelet-vessel wall interactions. *Thrombosis Research* **133,** 525–531 (2014).

109. De, R. A general model of focal adhesion orientation dynamics in response to static and cyclic stretch. *Communications Biology* **1,** (2018).

110. Guenat, O. T. & Berthiaume, F. Incorporating mechanical strain in organs-on-a-chip: Lung and skin. *Biomicrofluidics* **12,** 042207 (2018).

111. Malinovskaya, N. A. *et al*. Endothelial Progenitor Cells Physiology and Metabolic Plasticity in Brain Angiogenesis and Blood-Brain Barrier Modeling. *Frontiers in Physiology* **7,** (2016).

112. Cukierman, E. Taking Cell-Matrix Adhesions to the Third Dimension. *Science* **294,** 1708–1712 (2001).

113. Gerhardt, H. *et al*. VEGF guides angiogenic sprouting utilizing endothelial tip cell filopodia. *The Journal of Cell Biology* **161,** 1163–1177 (2003).

114. Ribatti, D. & Crivellato, E. “Sprouting angiogenesis”, a reappraisal. *Developmental Biology* **372,** 157–165 (2012).

115. Rempe, R. G., Hartz, A. M. & Bauer, B. Matrix metalloproteinases in the brain and blood–brain barrier: Versatile breakers and makers. *Journal of Cerebral Blood Flow & Metabolism* **36,** 1481–1507 (2016).

116. Ingber, D. E. Mechanical Signaling and the Cellular Response to Extracellular Matrix in Angiogenesis and Cardiovascular Physiology. *Circulation Research* **91,** 877–887 (2002).

117. Du, Y. *et al*. Three-Dimensional Characterization of Mechanical Interactions between Endothelial Cells and Extracellular Matrix during Angiogenic Sprouting. *Scientific Reports* **6,** (2016).

118. Juliar, B. A., Keating, M. T., Kong, Y. P., Botvinick, E. L. & Putnam, A. J. Sprouting angiogenesis induces significant mechanical heterogeneities and ECM stiffening across length scales in fibrin hydrogels. *Biomaterials* (2018). doi:10.1016/j.biomaterials.2018.02.012

119. Ceccarelli, J. & Putnam, A. J. Sculpting the blank slate: How fibrin’s support of vascularization can inspire biomaterial design. *Acta Biomaterialia* **10,** 1515–1523 (2014).

120. Kniazeva, E. *et al*. Quantification of local matrix deformations and mechanical properties during capillary morphogenesis in 3D. *Integrative Biology* **4,** 431 (2012).

121. Kim, J. *et al*. Engineering of a biomimetic pericyte-covered 3D microvascular network. *PloS one* **10,** e0133880 (2015).

122. Antoine, E. E., Vlachos, P. P. & Rylander, M. N. Review of Collagen I Hydrogels for Bioengineered Tissue Microenvironments: Characterization of Mechanics, Structure, and Transport. *Tissue Engineering Part B: Reviews* **20,** 683–696 (2014).

123. Shamloo, A., Mohammadaliha, N., Heilshorn, S. C. & Bauer, A. L. A Comparative Study of Collagen Matrix Density Effect on Endothelial Sprout

Formation Using Experimental and Computational Approaches. *Annals of Biomedical Engineering* **44,** 929–941 (2016).

124. Barry, C. *et al*. Uniform neural tissue models produced on synthetic hydrogels using standard culture techniques. *Experimental Biology and Medicine* **242,** 1679–1689 (2017).

125. Garcia-Polite, F. *et al*. Pulsatility and high shear stress deteriorate barrier phenotype in brain microvascular endothelium. *Journal of Cerebral Blood Flow & Metabolism* **37,** 2614–2625 (2017).

126. Bankstahl, M. *et al*. Blood–Brain Barrier Leakage during Early Epileptogenesis Is Associated with Rapid Remodeling of the Neurovascular Unit. *eneuro* **5,** ENEURO.0123-18.2018 (2018).

127. Cancel, L. M., Arias, K., Bikson, M. & Tarbell, J. M. Direct current stimulation of endothelial monolayers induces a transient and reversible increase in transport due to the electroosmotic effect. *Scientific Reports* **8,** (2018).

128. Iandolo, D. *et al*. Development and Characterization of Organic Electronic Scaffolds for Bone Tissue Engineering. *Advanced Healthcare Materials* **5,** 1505–1512 (2016).

129. Javadi, M. *et al*. Conductive Tough Hydrogel for Bioapplications. *Macromolecular Bioscience* **18,** 1700270 (2018).

130. Mantione, D. *et al*. Poly(3,4-ethylenedioxythiophene):GlycosAminoGlycan Aqueous Dispersions: Toward Electrically Conductive Bioactive Materials for Neural Interfaces. *Macromolecular Bioscience* **16,** 1227–1238 (2016).

131. Rivnay, J. *et al*. Organic electrochemical transistors. *Nature Reviews Materials* **3,** 17086 (2018).

132. Curto, V. F. *et al*. Organic transistor platform with integrated microfluidics for in-line multi-parametric in vitro cell monitoring. *Microsystems & Nanoengineering* **3,** 17028 (2017).

133. Inal, S. *et al*. Conducting Polymer Scaffolds for Hosting and Monitoring 3D Cell Culture. *Advanced Biosystems* **1,** 1700052 (2017).

134. Curto, V. F., Ferro, M. P., Mariani, F., Scavetta, E. & Owens, R. M. A planar impedance sensor for 3D spheroids. *Lab on a Chip* **18,** 933–943 (2018).

Chapter 7: Conclusions

This thesis reports the development of electrical platforms with improved coupling between electronics and biology and their compliant integration within 3D barrier tissue models.

After a short introduction, chapter 2 discusses the evolution of *in vitro* barrier tissue models toward 3D configurations, which offer better cell-cell and cell-matrix interactions within a controlled microenvironment. I present the limits of conventional electrical platforms to be integrated in 3D cell culture systems to monitor barrier tissue ionic conductance. The high impedance and rigidity of metal electrodes both limit the interactions with biological tissues. I demonstrate that this challenge can be overcome using OECTs to provide in-line 3D cell impedance sensing.

In chapter 3, I quantified for the first time the ionic conductance of an airway epithelium using a flexible OECT-based platform. Traditionally electrical tools require barrier tissues to be fully immersed into the electrolyte, which is irrelevant for air-liquid interface tissue configuration. I designed an organic sensor that is flexible and mechanically compliant with biological tissues to monitor tracheal epithelium directly at the air-liquid interface. In this configuration, the electrolyte corresponds to the cell-secreted mucus. It allowed me to perform relevant vapor toxicity analysis under tissue physiological conditions. Thanks to this innovative platform, I demonstrated important breakthroughs in the field of e-cigarette toxicity.

In chapter 4, I monitored spheroid ionic resistance using an OECT-based impedance sensor. Spheroids are 3D structures of bulk of cells embedded into their own-secreted matrix. This free-floating configuration makes spheroids complicated model to characterize electrically. In this work, OECTs are integrated within PDMS microfluidic chambers to record spheroid impedance with high temporal-resolution. Thanks to PEDOT:PSS's low impedance, OECTs established a superior electrical coupling with tissue ionic conductance compare to traditional metal electrodes. I thus demonstrated the ability of this new platform to segregate spheroids according to their size and thickness.

In chapter 5, I present a new strategy to make organ-on-a-chip in-line sensors using OECTs blended with a collagen-based 3D microvessel network. Organ-on-a-chip systems are among the most complex *in vitro* cell culture platforms and their use for drug testing is on the rise. However, the integration of metal electrodes within micron-size chambers remains challenging. In our platform, 3D microvessels are placed on the OECTs for the continuous monitoring of blood brain barrier (BBB) formation.

The BBB regulates ion and solute diffusion within the brain tissue to help maintain its proper functions. However, the BBB prevents the majority of drugs from entering the brain and its disruption is linked to many neurological diseases. The complex cellular and molecular composition of the BBB makes it challenging to be reproduced *in vitro*. In chapter 6, I review materials that have been used over the past five years to mimic BBB microenvironment features. I highlight the importance of cell-matrix interactions to promote *in vitro* BBB integrity. I also suggest the potential of conducting organic material to monitor BBB properties while preserving integrity of both cell-cell and cell-matrix interactions.

As an interesting perspective, the design of OECTs using conducting hydrogels might be a promising way to interface with ultra-soft biological tissues such as the brain (0.5-1 kPa). This stretchable conducting material should maintain conformal contact with dynamic tissue surface. Soft OECTs might be envisioned providing both *in vitro* recording of BBB integrity and electrical stimulation of the surrounding neural tissue.